RF Feedforward Interference Cancellation For Wide-band Signals using Adjustable Band-stop Resonators

Sarah Adel Ibrahim

A thesis submitted in partial fulfillment of the requirements for

Doctor of Philosophy

Department of Electronic Engineering

National University of Ireland, Maynooth

Ireland

Head of the Department: Ronan Farrell

Supervisor of the Research: Ronan Farrell

Declaration

I hereby certify that this thesis, which I now submit for assessment on the program of study leading to the award of PhD has not been submitted, in whole or part, to this or any other University for any degree and is, except where otherwise stated the original work of the author.

Signature:

June 6, 2017

Abstract

This dissertation is focused on developing RF feedforward cancellation systems for wide-band interference signals appearing at close proximity from the receiver. The system is designed to target high interference risks in the Upper-700 MHz band (746-805 MHz) following the congestion in the spectrum between public safety land mobile radios, LTE broadband public safety and LTE commercial mobile. New low-profile planar band-stop resonators are designed to obtain a wide-band and a high roll-off rejection (> 1dB per MHz). Two new design methodologies of band-stop resonators are presented in this work. The first approach incorporates the use of power splitters and large delay transmission lines, and the second methodology uses finite cell artificial left-hand transmission lines. The two structures are used in separating the receiver wanted signal from the interferer, and this separation is required to generate a replica of the interferer, which later becomes an input to the cancellation phase of the system. The system is tested using two generated LTE modulated signals, modeling the interference and the wanted signals, which are 20, 15 and 10 MHz apart. The test results have shown successful cancellation for 9 MHz wide interference signals. The cancellation can be further improved over a wide band, by increasing the linearity of the phase shifters used in the feedforward system. Therefore, new RF MEMS switch based phase shifters are designed, implemented and measured. Measurements of the new phase shifters have successfully reduced the RMS amplitude deviation, which is calculated between all the phase states over a 100 MHz bandwidth, by 66% when compared to the phase shifter used in the above interference cancellation tests.

Acknowledgment

My deep gratitude goes first to Professor Ronan Farrell, who supported me in many ways during the entire journey. I would also like to thank Grzegorz Szczepkowski, John Dooley, James Kinsella, Han Su and all the department colleagues for their help and support. I am very much thankful to Ziming Wang who has always been very encouraging, inspiring as well as very entertaining. I am very grateful to Kieth Finnerty who has been very much helpful.

I thank the RF teams in Analog Devices Co. and Bell Labs (Nokia) in Ireland.

I thank Joanna, Lorna and Louise for offering help with the thesis writing.

I would also like to thank Lorraine, Angela, Sheree, Paola, Stephanie, Sara and Anna for all the wonderful times we had together in Maynooth.

Finally, I thank my family for their continuous support, understanding, and for all the beach summer vacations.

Contents

Chapter 1

Introduction

The advanced developments in telecommunication standards are now enabling high data rate communication employing larger bandwidths. These developments have become attractive to many businesses and services, which are not only involved at commercial mobile industry. With the increasing demand of high data rate communication, the frequency spectrum is getting congested more and more with multiples of different operators. To enable larger bandwidths for each of these operators, the guard bands which are used to separate their operating bandwidths, are getting smaller. Eventually, this results in multiples of interference scenarios, which are continuously getting worse and the quality of communication is highly degraded. A famous example of a frequency congested spectrum is the 700 MHz band (Upper-700 MHz band), which is now shared between three different operators: public safety land mobile radios; the new LTE broadband public safety devices; and the commercial mobile LTE operator [1]. This band has been selected as a use case in this thesis, however the review and the study performed in this work can be applied on other congested spectrums.

1.1 The Next Generation of Public Safety Networks

Public safety organizations have relied on Land Mobile Radios (LMR) for communication at emergency times. Land Mobile Radios use either Digital or Analog modulation schemes which support long range voice communications [1]. These radios operate over a very narrow bandwidth, typically less than 1 MHz, such as TETRA (Trans-European Trunked Radio) and Project 25 in North America. The next generation of public safety networks requires high speed data communications in order to support advanced multimedia applications for safety agencies. Despite the need of high rate data networks, broadband data networks are not going to replace the Land Mobile Radios. In fact, the aim is to have an interoperability between the narrowband radio network and the new broadband safety network, so that the benefits of the two networks are combined. This decision was taken after several incidents including the Hurricane Katrina when cell phone towers went down for several days leaving the digital LMR radios as the only means of communication [1].

In 2007, the Federal Communications Commission (FCC) authorized a new spectrum channelization plan for the Upper-700 MHz band [2]. It divided the frequencies from 698 MHz to 806 MHz into three sections: the new broadband network for only Public Safety data and no other purposes; the narrow band Land Mobile Radio narrow band channels; and the commercial LTE mobile network, as shown in Fig. 1.1. In 2012, the US government formed FirstNet and committed USD 7 billion to the development of the new Public Safety broadband network [3].

It is expected to have several potential interference issues between the different operators in such a highly congested spectrum where only a 1 MHz guard band is allocated as shown in Fig. 1.1. Interference can occur either between the narrow band and the broad band public safety networks, or between any of the two with the commercial LTE Mobile network. The narrow band public safety networks can cause the most critical interference scenarios, since they are transmitting and receiving simultaneously using 50 Watt

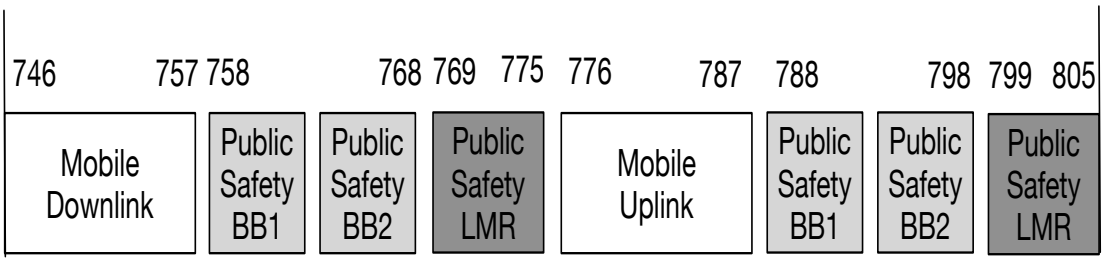

Figure 1.1: The spectrum allocation of the Broadband and the narrow band Public Safety with the commercial Mobile signals in the Upper-700 MHz band.

devices. This thesis is focused on finding solutions to manage the interference between the different public safety operators and the commercial mobile base station transceivers operating in the Upper-700 MHz band.

1.2 Motivation

The high risks of interference in congested frequency spectrums raise the potential of a serious threat to public safety and commercial mobile operators. The potential interference levels in these bands not only degrade the quality of communications, but also increase the chance of dropped calls for mobile users and emergency services. The LTE telecommunication standards impose strict performance requirements for interference limits to avoid degrading the throughput of the receiver by more than 5%. The throughput is defined as the number of payload bits successfully received per second for a reference measurement channel in a specified reference condition. Some handset manufacturers apply the maximum power reduction technique to mitigate interference levels, and achieve the necessary adjacent channel leakage ratio (ACLR) levels. However, reducing the transmitting power can severely worsen the network coverage, thus raising the need for extra nodes or base stations. Another way to meet the minimum ACLR requirements for LTE transceivers is to provide an additional stop band rejection of 23- 29 dB for their

front end duplexers, but this significantly raises the costs and complexity of the duplexer.

Small cell base station transceivers (e.g. metro-cell, picocell, ...etc) are more prone to interference risks, since their RF front end duplexers are constructed using ceramic based resonators. Ceramic duplexers provide less stop band rejection when compared to microwave air cavity duplexers which are used in large base stations. Air cavity duplexers offer much higher stop band rejection, however their structures are heavy, bulky in size, very expensive to fabricate and maintain, and very difficult to tune their frequency response. Knowing that the main interest for small cells is to mitigate the trade-off between cost, size and meeting the high performance requirements, the idea of replacing ceramic based filters with microwave air cavities is not acceptable, and finding an alternative approach that can assist ceramic duplexers in rejecting large interference signals becomes necessary.

1.3 Research Objectives

The objective of the research conducted in this thesis is to develop an RF interference cancellation system that can improve the stop band rejection characteristics of the front end duplexers in LTE base station transceivers, so that they can meet the minimum requirements for power levels defined in the 3GPP standards [4, 5]. This improvement involves increasing the attenuation of the receiver front end by 23-29 dB at the frequency locations of the interference signals. Since spectrum congestion encourages the appearance of interference signals at small frequency offsets, new sharp rejection filtering solutions are required with a narrow transition band between the pass and the stop band (a high roll-off rate).

Having the Upper-700 MHz band congestion selected as a use case for this thesis, the system should be designed to operate around 700 MHz, and should be tested using LTE modulated signals with a minimum bandwidth of 9-10 MHz, as defined in the

specified spectrum. The system should also keep minimum distortion levels in the band of the wanted receiver signal. At the end, this research should present a less complex solution using low profile RF components, that does not require large space nor high implementation costs.

1.4 The Structure of the Thesis

- Chapter II starts with a short description on the structure and performance of microwave cavity and ceramic based duplexers describing their limitations in handling high power interference in the 700 MHz band. Followed by a review on the existing solutions or approaches for managing interference signals generated from either unwanted emissions in the transmit chain, or a leakage from the transmit chain to the receiver, or neighboring channels operating at frequencies close to the receiver band. The chapter also includes a review on different microwave filter structures that can be used to separate close interference signals.

- Chapter III proposes a new RF feedforward interference cancellation system for assisting ceramic duplexers in rejecting high power interference signals. The chapter starts by explaining the system operation, and listing the performance criteria, design challenges on the RF hardware, and the additional requirements necessary to obtain some degree of reconfigurability in pursuance of handling the dynamic nature of interference signals. The chapter also discusses the practical implementation of the system by selecting some of the off-the-shelf RF components, and encouraging the development of new designs for handling very close interferers including bandstop resonators and controlled phase shifters .

- Chapter IV presents the development of a new structure of passive band-stop resonators named as “Multi-Tap Delay Resonator”. It offers very high selectivity with a

3 dB bandwidth of only 11 MHz, in addition to a sharp rejection roll-off rate of more than 1 dB per MHz. The new resonator is thus able to separate interference signals located at 20, 15 and 10 MHz frequency separation from the edge of the receiver signal. The chapter also demonstrates the RF feedforward interference cancellation system after placing the Multi-Tap Delay resonator in the auxiliary path of the feedforward loop, and successful cancellation of interferers is achieved.

- Chapter V studies the use of artificial left handed transmission lines in replacing the large delay transmission lines used in the design of the Multi-Tap Delay band-stop resonator. It presents the development of a new design named as composite right-left handed (CRLH) band stop resonators, which proved to keep the same cancellation performance while reducing the size of the circuit by more than 87 %. Furthermore, the in-band losses due to the cancellation system are reduced by more than 1.9 dB.

- Chapter VI presents the development of new RF MEMS switched phase shifter circuits, which are designed to obtain high phase linearity over a 100 MHz bandwidth, so that they can be used to improve the signal matching in the feedforward loop system, after replacing the off-the-shelf phase shifter used earlier in the system setup. The chapter includes a study of different microwave structures, and circuit topologies used to integrate the MEMS device and build the phase lines.

Chapter 2

Review of Existing Solutions for RF Interference in LTE BS Transceivers

2.1 Introduction

In general, this chapter provides a background on the existing solutions for interference management in RF transceivers. These solutions include front-end system architectures as well as microwave filtering structures. The solutions are judged based on their ability to handle high power interference signals appearing at small frequency offsets from the receiver, which describes some of the interference challenges in congested frequency spectrums. In addition, the complexity, size and cost of either the system architectures or filter structures are discussed.

At the beginning of this chapter, a general overview is presented discussing the evolution of LTE mobile communication standards. Section 2.3 presents the standards defined for LTE mobile transceivers as well as the new broadband public safety devices. This includes the power requirements for LTE base station transceivers; receiver sensitivity; receiver dynamic range; adjacent channel selectivity; and the receiver blocking requirements. All these requirements are then discussed to identify the levels of poten-

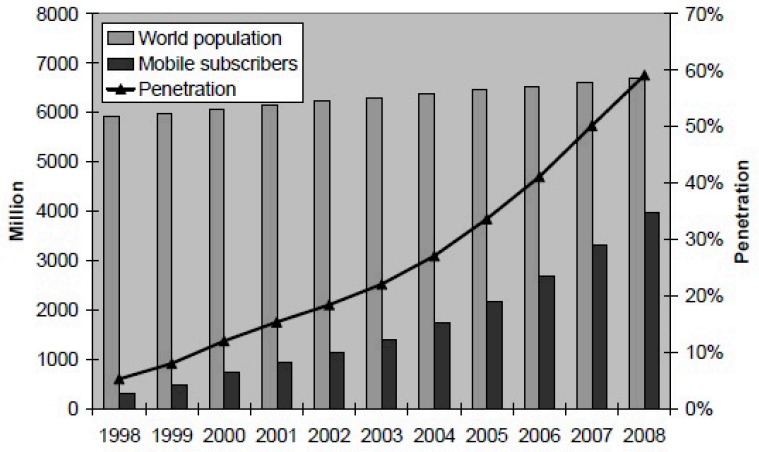

Figure 2.1: Growth of mobile subscribers over the past 10 years.

tial interference between LTE mobile and broadband public safety networks in the 700 MHz spectrum. Section 2.4 studies the performance of high Q duplexers employed in small and large base station transceivers, while listing their limitations in handling the public safety interference issues. Section 2.5 conducts a review on existing interference management solutions which are grouped into three according to the source of the interference signals: unwanted emission in the transmit chain; transmit power leakage into the receiver; and neighboring channels. At the end of this section, a discussion is performed on the limitations of the studied solutions. Section 2.6 conducts a review on high performance RF filters that can assist in separating close interference signals.

2.2 Evolution of LTE Standards

Analog telecommunications standards were first introduced in the 1980s, and the first generation (1G) mobile standard (e.g. advanced mobile phone systems (AMPS)) was later developed [6]. The 1G standard was defined for voice communication only and data service was still not available. Soon after, the second generation (2G) mobile phone systems emerged with two different standards; the European GSM and American CDMA. 2G

mobile networks were originally designed for carrying voice traffic only. However data capabilities were added at a later stage starting with the SMS service which was introduced to mobile users for the first time. However, the traffic volume was still dominated by voice only. Some 2G systems have implemented the packet-switched domain in addition to the circuit-switched domain, where a complete circuit is switched for a given user. The general packet radio services (GPRS) systems have evolved into the 2.5 G. At a later stage, the use of 2G phones became more widespread and people began to use mobile phones in their daily lives. Moreover, the demand for data such as internet access, streaming services and file sharing started growing which pushed industry to work on developing a more efficient mobile network.

In 2001, the third generation (3G) network was launched with higher data transfer speeds and capacity compared to 2G. Consequently, the better data transfer features in 3G had further expanded the number of mobile subscribers and the traffic volume became highly dominated by data transfer instead of only voice. The growth rate of data usage in 3G networks was fueled by the streaming media and mobile phone applications like video sharing, TV mobile and interactive gaming. A typical voice subscriber uses 300 minutes per month with a voice data rate of 12.2 kbps, which requires approximately 30 megabyte of data. A data user can easily consume more than 1 gigabyte of data during the same period. In general, mobile data usage requires 10 to 100 times more megabytes of data, when compared to voice usage [6]. Over the past 10 years, mobile subscribers have been rapidly increasing with a daily average growth rate of more than 1 million, as mobile phones have become the most preferred method in voice as well as data communication. The variation of mobile subscribers over the past 10 years can be seen in Fig. 2.1 together with the mobile network coverage compared to the world's population [6]. There is a continuous growing of the number of people connected to internet. Therefore, industry began looking for the 4th generation technologies with more data optimization techniques and speed improvements, since it became clear that 3G would be

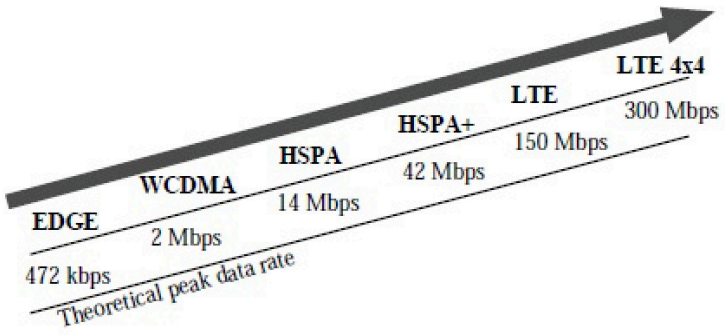

Figure 2.2: Evolution of peak data rate among different mobile networks.

overwhelmed by data transfer. The first two commercially available technologies, which were listed as 4G, were the WiMAX, and the LTE standard. WIMAX was offered in the U.S. by Sprint, while LTE was first offered in Scandinavia by Telia Sonera [8].

The first step in the process of developing mobile networks is system standardization, where the objectives and targets of the new network are defined. Usually, it takes more than 5 years for every new mobile generation to emerge, starting from setting the system standards, realization of these standards, and validation till commercial deployment becomes applicable. Data rates for GSM (EDGE) and WCDMA were defined in 1997 and 1999, respectively [7]. However, both systems had their first commercial deployments in 2002. The same for HSPA evolution, whose system standards were completed in 2007 and the deployments started only after 2009 [6]. The performance targets of LTE were defined relative to HSPA (High Speed Packet Access) in 3GPP standard release no. 6 [10], since HSPA is known for having the highest data transfer rates possible among all the current operating systems.

LTE standards are designed such that the peak data can be pushed further. Fig. 2.2 illustrates how data rates increased from one mobile network to another. The first target of LTE is to achieve a minimum peak user throughput of 100 Mbps in downlink and 50 Mbps in uplink, which is ten times more than HSPA. The second target is the

	Max rated output power	Min coupling loss	Max. received power
Wide Area BS	N/A	70 dB	-
Medium Range BS	< 38 dBm	53 dB	-15 dBm
Local Area BS	< 24 dBm	45 dB	-21 dBm
Home BS	< 20 dBm	N/A	-

Table 2.1: The minimum coupling losses from BSs to UE, and the maximum rated output power for BSs operating in single carrier or multi-carrier configurations.

power consumption, which needs to be minimized in order to enable more usage of the multimedia applications without the need of recharging the battery over short periods of time. LTE is characterized by the flexibility of spectrum as the transmission bandwidth can vary between 1.4, 3, 5, 10, 15 and 20 MHz.

2.3 LTE Standards for Mobile BSs

This section presents the power requirements for LTE mobile base station transmitters and receivers according to LTE standards for broadband public safety networks as well as the commercial mobile networks. The standards are defined in 3GPP Release 9 [4] and updated in Release 14 [5]. At the end of this section, all requirements are discussed to identify the levels of the potential interference between the two networks.

2.3.1 Power Requirements for LTE Mobile BS Transmitters

LTE Mobile base stations (BS) are classified according to their coverage area into a macro-cell (also named as “Wide Area BS”), a micro-cell (also named as “Medium Range BS”), a pico-cell (also named as “Local Area BS”), and a femto-cell (also named as “Home BS”).

For all mobile BSs, the transmitted output power affects the magnitude of unwanted emissions outside the transmission bandwidth. Unwanted emissions can directly influence the interference levels experienced by neighboring cells using the same channel.

	Receiver sensitivity
Wide Area BS	-121 dBm
Medium Range BS	-111 dBm
Local Area BS	-107 dBm
Home BS	-107 dBm

Table 2.2: The sensitivity level of LTE BS receivers [5].

This affects the ability of the LTE system to maximize spectral efficiency. Therefore, it is important that the transmitters can set their output power accurately. The maximum output power for all BSs must remain within ±2 dB of the rated output power assigned. The rated output power is defined as the mean power level per carrier for BS that a manufacturer has declared to be available at the antenna connector. There is no upper limit for the rated output power for "Wide Area BS". For other BSs, the output rated power is listed in Table. 2.1.

2.3.2 Power Requirements for LTE Mobile BS Receivers

2.3.2.1 Receiver Sensitivity and Dynamic Range

The upper limit for the average signal power that can be received by an LTE base station can be identified by referring to the minimum coupling losses, which are the losses encountered by the signal as it propagates between the user equipment and the base station tower. Table. 2.1 lists the minimum coupling losses for each BS type. The table also lists the upper limit for the average received power [5]. Coupling losses are not defined for Home BS.

On the other hand, the minimum power level requirements of LTE receivers are defined based on the receiver sensitivity level, which is the level of the minimum mean power received at which the bit error ratio shall not exceed the maximum specified levels defined in the 3GPP standards. The receiver sensitivity of LTE mobile BSs are listed in Table. 2.2. Another important parameter is the dynamic range of the receiver, which

	AWGN interferer	Wanted signal
Wide Area BS	-79.5 dBm	-70.2 dBm
Local Area BS	-71.5 dBm	-62.2 dBm
Home BS	-35 dBm	-25.7 dBm

Table 2.3: The minimum requirements for the receiver signal levels with 10 MHz channel bandwidth at the presence of AWGN interferers.

determines the ability of the receiver to handle a rise of interference in the receiver band. The dynamic range is used to define the minimum requirement for the wanted signal mean power. The receiver shall fulfill a specified bit error rate requirement for a specified sensitivity degradation in the presence of an interfering AWGN signal as listed in Table. 2.3.

2.3.2.2 Adjacent Channel Selectivity and Blocking Requirements

Adjacent channel selectivity (ACS) is a measure of the receiver ability to receive a wanted signal at its assigned channel frequency in the presence of an adjacent channel signal with a specified centre frequency offset of the interfering signal to the band edge of a victim system. In this condition a throughput requirement shall be met for a specified type of interference signal and frequency offset. The minimum requirements for ACS in all base station types are defined based on the adjacent channel leakage ratio (ACLR), which is defined as the ratio between the filtered mean power centered on the assigned channel frequency to the filtered mean power centered on an adjacent frequency channel. The ACLR is controlled by the maximum allowed level of unwanted power emissions from the transmit chain. The ACLR minimum requirement is 45 dB for all different BSs and at all the different LTE channel bandwidths (1.4, 3.0, 5, 10 and 20 MHz). Therefore, modulated interference signals appearing close to the base station receiver are going to introduce a maximum of in-band interference of 45 dB less than the interference mean power. Accordingly, the minimum requirement on interference mean power are defined in Table. 2.4 for 1.4 and 5 MHz interfering signals located at larger than 2.5 MHz frequency

	Wanted signal mean power	Interferer mean power	Interferer BW
Wide Area BS	Rx sens. + 11 dB	-52 dBm	1.4 MHz
	Rx sens. + 6 dB		5 MHz
Local Area BS	Rx sens. + 11 dB	-44 dBm	1.4 MHz
	Rx sens. + 6 dB		5 MHz
Home BS	Rx sens. + 27 dB	-28 dBm	1.4 MHz
	Rx sens. + 22 dB		5 MHz

Table 2.4: Minimum power requirement for adjacent channel selectivity in LTE mobile BS receivers at larger than 2.5 MHz frequency offset.

offset [9].

2.4 The New LTE Public Safety and Interference in the 700 MHz Spectrum

Public safety agencies are employing LTE broadband communication devices to enable the use of high data rate multi-media applications serving their missions. The new devices are not going to replace the conventional digital land mobile radios. Both services are allocated frequencies in the 700 MHz spectrum which is also occupied by the commercial mobile LTE band 13 (also referred to as Upper C band).

The “FCC Public Safety and Homeland Security Bureau” mandates LTE technology for the 700 MHz Public Safety band (Band 14) [2]. In 2014, there was only one power class defined for the public safety UE devices which is referred to as power class 3 in the 3GPP standards. The maximum transmit power for this class is set to be 23 dBm. This limitation on upper link power is a bottleneck to enable higher achievable data rate with broader coverage, which are essential for Public Safety broadband systems to provide the necessary population coverage. Public safety needs to provide better coverage and availability or throughput performance than provided by commercial mobile systems particularly in rural areas. This can be achieved by using higher power UE(s) for vehicular mobile applications. This can allow “first responders” to send and receive video and data,

thus providing the ability to co-ordinate response and protect lives in these scenarios. In 3GPP Release 14, the maximum transmit power level for Public Safety UE devices is increased to reach 33 dBm [5]. On the other hand, the narrow band public safety devices which operates using an average power of more than 47 dBm.

2.4.1 Interference levels in the 700 MHz Spectrum

Interference in the 700 MHz spectrum between public safety and commercial mobile networks can have many different forms. Public safety broadband devices transmit and receive in the 788-798 MHz band, in addition to the 758-768 MHz band. Public safety mobile radio are also operating between 769-775 MHz and 799-805 MHz. On the other hand, the uplink and downlink of mobile LTE operate in 776-787 MHz and 746-757 MHz, respectively. Such congestion has resulted in many interference scenarios between the different operators.

One scenario is where the base station receiver of a mobile LTE can become a victim of strong interference signals generated from either broadband public safety transmitters operating on its upper side band, or land mobile radios operating at its lower side band. Although, public safety land radios occupy very narrow bandwidths, they have to be considered since they can appear as close as 2 MHz only away from the edge of the uplink band. At the worst case, public safety interference can reach the uplink receiver with a power level ranging from -15 dBm to -21 dBm according to the minimum coupling losses discussed above for a local area base station. The adjacent channel selectivity requirements have mentioned that the power level of interference signals with less than 5 MHz bandwidth must not exceed -44 dBm. This means that a minimum of 23-29 dB suppression must be introduced to public safety interference signals reaching the mobile base station receiver to reach the minimum requirement defined in the 3GPP standards.

Similarly, the receiver of public safety land mobile radios can become a victim for the public safety broadband operating at its upper sideband, and in other scenarios, the

broadband public safety devices itself are affected by interference from the mobile downlink signals.

2.5 High Q Duplexers in LTE Base Stations

A duplexer is a three port passive device that allows transmitters and receivers to operate simultaneously via a single antenna. It combines the transmitter and the receiver front end filters, and isolates the two output of these two filters permitting them to share a common antenna.

2.5.1 Microwave Cavity Resonators

A microwave cavity or radio frequency (RF) cavity is a special type of resonator, consisting of a closed (or short-circuited) metal structure (or sections of waveguides), or high permittivity dielectric materials (e.g. Ceramic) that confines electromagnetic fields over a specific range of frequencies. The metal structure can be either hollow forming air cavity resonators, or partially filled with dielectric material. Microwave cavity are capable to handling high power levels, hence they are used in large BS systems.

In air cavity resonators, both the electric and magnetic fields are stored in a hollow metallic cavity. In this case, the only losses are due to finite conductivity of the cavity walls. The surface walls of cavity resonators are usually plated with either gold or silver to increase their conductivity, further reducing the conductor losses and preventing oxidation. Similar to waveguides, the losses of these resonators are extremely low leading to a very high Q factor when compared to lumped LC resonators. The Q factor is defined based on the cavity perturbation theory to be the ratio between the stored energy and the energy dissipated inside the resonant cavity [11].

There are three different techniques for EM excitation of cavity resonators, which are Loop excitation, Probe excitation and Aperture excitation [12]. In loop excitation, the RF

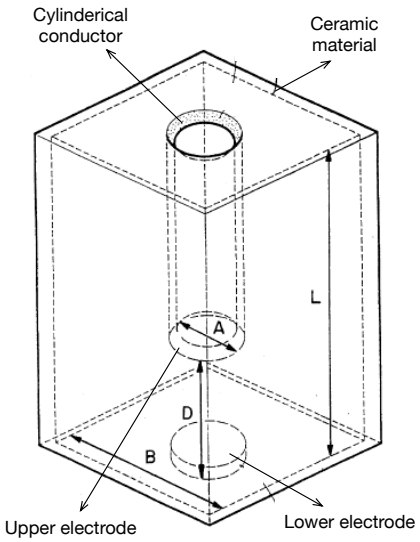

Figure 2.3: The structure of a ceramic resonator with cylindrical electrodes [15].

signal is applied on a loop, which is inserted inside the cavity. This causes the magnetic flux to expand and contract around the loop, which induces current on the surface walls of the cavity. In Probe excitation, a probe is inserted instead inducing magnetic field inside the cavity. Aperture excitation is carried out by making a slot in the cavity resonator where either electric or magnetic fields are coupled using either a circular or a rectangular waveguide [13].

2.5.2 Dielectric (Ceramic) Resonators

Di-electric resonators are formed using a rigid block of dielectric material (usually ceramic). The resonant response characteristics are mainly determined by the overall physical dimensions and properties of the dielectric material. An example of a ceramic resonator is shown in Fig. 2.3 [14].

EM excitation of ceramic resonators is usually performed by inserting two electrodes, one electrode at the bottom surface of the ceramic material and a second one at the

bottom of the cylindrical hole. This electrode can have different shapes (e.g. square, rectangle, circle, cross,...etc.) [15]. The shape and the physical dimensions of the electrodes are also used to control the resonance frequency.

Ceramic resonators are much smaller in size when compared to air cavities, as the guided wavelength is reduced by more than 70%. Ceramic resonators are also less expensive to fabricate. They are typically used in small-cell BSs (e.g. Picocell and Femtocell). Despite their low fabrication costs, ceramic filters can't totally replace cavity filters in large BSs due to their power handling limitations.

2.5.3 Rejection and Roll-off Rate of Cavity and Ceramic Duplexers

Cavity filters are characterized by a very high stop band rejection and a very sharp roll-off. For example, the rejection of a typical 6 order cavity duplexer from MCV Microwave Manufacturer operating in the 700 MHz LTE band is above 85 dB. In addition, the roll-off rate can exceed 4.6 dB per MHz. On the other hand, a 6th order Ceramic duplexer from the same manufacturer operating in the same LTE band can achieve a maximum rejection of 65 dB with a maximum roll-off rate of 3.3 dB per MHz.

2.5.4 Frequency Tuning of Cavity and Ceramic Duplexers

New LTE receivers require more tunable and adaptable filtering techniques to meet the flexibility requirements of the channel bandwidth. Microwave cavity resonators are tuned mechanically using tuning screws which is usually performed manually as shown in Fig. 2.4. In 2013, some research work has been conducted on electrically tuning cavity filter using MEMS switched capacitor banks and piezomotors [16]. Fig. 2.5 shows the new electrically tuned cavity filter from 2.56 to 2.63 GHz. Each cavity consists of tuning desks which are mechanically adjusted using piezomotors together with RF MEMS capacitor banks to introduce some variations in the resonance frequency. Unlike, the tuning screws,

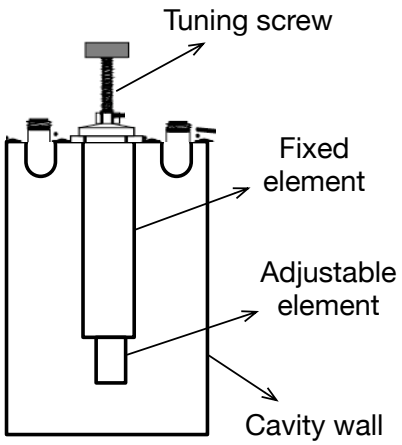

Figure 2.4: Mechanically tuning microwave air cavities using a tuning screw.

this technique introduces some degradation in the stop-band rejection performance and blocking characteristics (rejection roll-off rate).

Ceramic filter are still facing difficulties in tuning their frequency response, however few attempts has been made on tuning hybrid cavity dielectric filters using GaAs transistors and RF MEMS switched capacitors in 2011 [17]. In this paper, the MEMS circuit board were placed inside the Teflon dielectric in each resonator to introduce some parasitic magnetic field that can be adjusted to tune the resonance frequency. Similarly, the tuning elements have also degraded the rejection performance of the teflon based dielectric filter.

2.5.5 Limitations of Employing High Q filters in Interference Management

As mentioned earlier, interference management in the 700 MHz spectrum requires increasing the stop band attenuation of the receiver filter by more than 29 dB while keeping a roll-off rate of more than 4 dB per MHz. Therefore, high Q duplexers in wide and local area base stations must be capable of providing additional rejection by the same value in the presence of strong interference signals. Some researchers have managed to

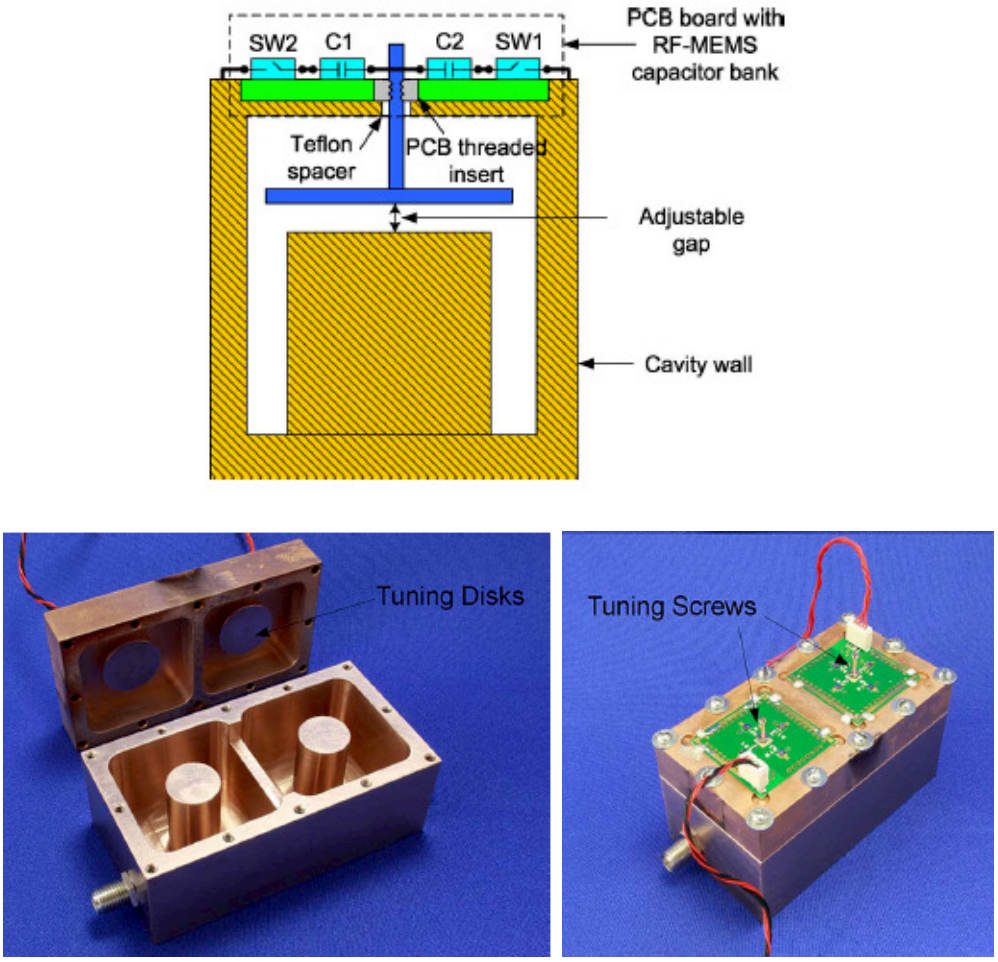

Figure 2.5: Cavity resonators tuned using RF MEMS capacitor bank and piezomotors [16].

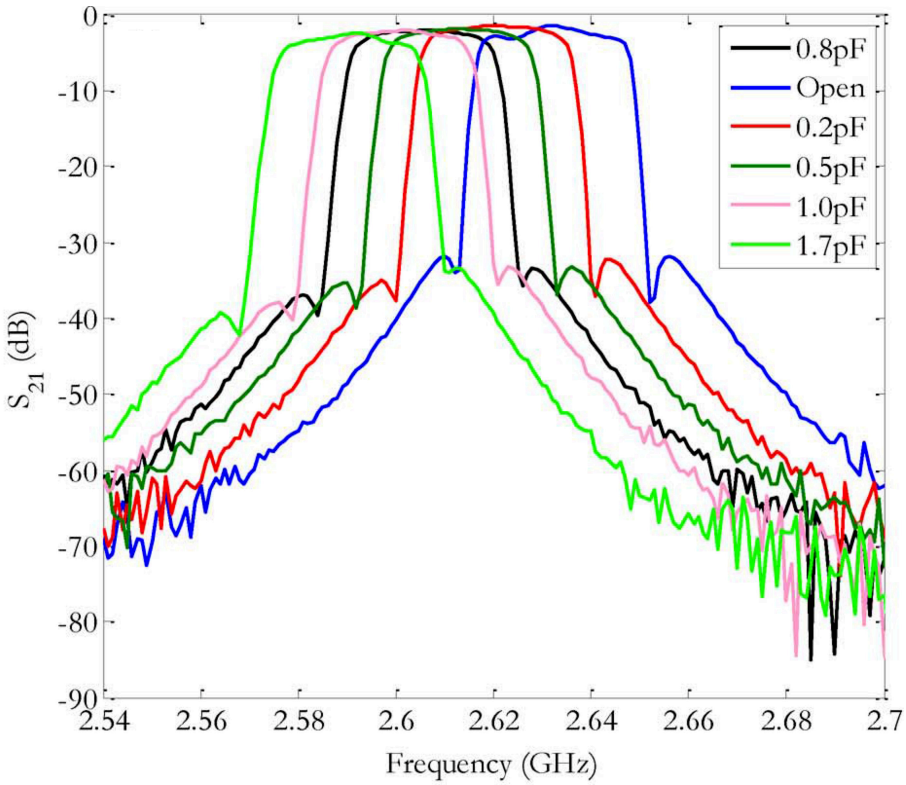

Figure 2.6: An example of tuning performance of cavity filter using MEMS switched capacitor banks and piezomotors [17].

improve the quality factor of air cavity resonators using corner rounding [18]. Hybrid configurations of cavity and dielectric resonators have also managed to improve the blocking performance of cavity to reach 100 dB. On the other hand, cavity resonators still suffer from their bulky size and weight which prevents them for being used in small cell base stations. Cavity resonators are only employed in wide area base stations, since their size and weight are not compatible with any of the smaller cells. Consequently, the robustness of wide area base stations to public safety interference signals are much higher.

In local area base stations, ceramic duplexers are still facing difficulties in improving their stop band rejection. Accordingly, a new solution is needed to relax the filtering requirements in order to assist ceramic duplexers in rejecting large interference signals, and also to reduce the order of cavity filters in large base stations, which can further reduce their size, fabrication and tuning costs.

2.6 Review of Interference Management Techniques

This section presents some of the existing approaches and techniques, which were developed for understanding, and preventing interference signals from degrading the performance of communication systems. The target of all the interference management techniques reviewed in this section is not to eliminate the need of RF filtering in transceiver systems, but relax the filtering requirements imposed on cavity and ceramic duplexers. Interference management techniques can be classified based on the source generating the interference signals. In general, there are three different sources of interference in RF transceivers.

1. Unwanted emissions in the transmit chain.

2. Power leakage of the transmitter signal onto the receiver (self-interference).

3. Interference generated from near by channels (inter-channel interference).

2.6.1 Existing Solutions for Unwanted Emissions in LTE Transceivers

As the level of the transmitted output power increases, the signal to noise ratio increases which improves the quality of intended transmission. However, increasing the transmitted power can also increase the level of unwanted emissions which adversely affect the interference levels. Therefore, requirements were set for LTE RF transmitters prescribing the maximum level of output power for the intended transmissions, as well as the level of unwanted emissions that can be tolerated while maintaining a high quality signal. Ideally, the transmitter should transmit power only in its assigned spectrum, but in practice this is never the case as unwanted emissions will always be introduced due to non linearities in the transmit chain.

There are two kinds of unwanted emissions; out of band (OOB) emissions and spurious emissions. OOB emissions are the emission that falls in a band close to the intended transmission bandwidth, while spurious emission are those which fall at any other frequency as seen in Fig. 2.7. Spurious emissions arise from a large variety of non-ideal effects including intermodulation products. Unlike OOB emissions, the magnitude of spurious emissions can be independent of the transmitted power level.

OOB emission mainly occurs due to non linear devices in the transmitter, e.g: power amplifiers and mixers. The magnitude of the OOB emission is dependent on the power level of the transmitted signal. The more power is transmitted, the higher the level of OOB emissions. Thus, reducing the transmitted power is usually an effective method for reducing the OOB emissions, however this impacts the signal to noise ratio levels at the receiver side which can degrade the recovering of the signal and overall data throughput. OOB emissions can be considered a major source of interference signals. Consequently, the level of OOB emissions is restricted with the adjacent channel leakage ratio (ACLR) constraint. This type of interference signals can be managed by suppressing the non-linearities in the transmit chain as discussed below.

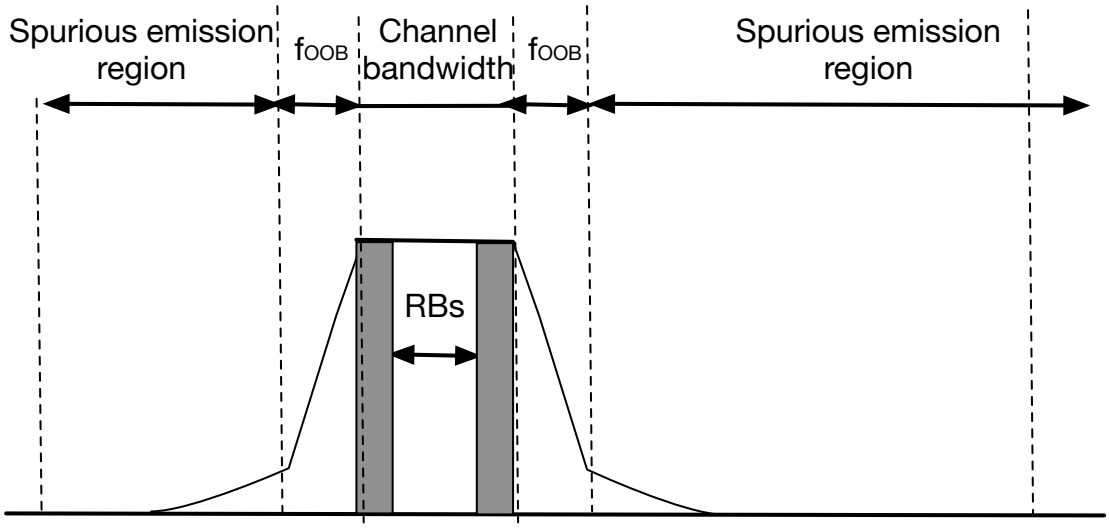

Figure 2.7: Unwanted emissions regions of the TX frequency spectrum.

2.6.1.1 Management of Non-linearities in RF transmitters

Non linearities in RF transmitters are not generated only by power amplifiers, however power amplifiers tend to have the major contribution to the transmitted signal distortion. At the highest power level, power amplifiers can be driven to operate in the non linear region, which results in adding more frequency components to the input signal at different amplitude levels. As a consequence, the level of out of band emissions increases. These undesired added frequency components are referred to as intermodulation distortion components. Their amplitude level depends on how far the power amplifier enters the non linear region. Several different techniques were developed to linearize power amplifiers including digital, IF and RF analog techniques. Some of these techniques are based on characterizing power amplifiers, hence they were called RF pre-distortion techniques [19]. Others use feedforward techniques, which are designed based on comparing the power amplifier input signal to a coupled replica of the output and subtracting the intermodulation components.

2.6.1.2 Power Amplifier Pre-distortion Techniques

Power amplifier pre-distortion is a technique that involves the use of some electronic circuit to implement an inverted behavior of the amplifier, so that it counteracts the non-linearities of the amplifier and minimize the distortion of the signal. Digital pre-distortion techniques usually show good linearization results compared to analog ones, however they suffer from a limited linearization bandwidth due to the memory effects of the system [9]. Another drawback of digital linearization techniques is the need for up conversion mixers. Mixers can adversely add more distortion to the signal which results in increasing the linearization requirements. On the other hand, analog pre-distortion solutions potentially offer broadband linearization. Nevertheless, in both cases the achieved linearity depends on a large number of different issues. A successful pre-distortion technique relies on the accuracy of the power amplifier characterization and the generation of an equivalent canceling characteristic. These techniques are very sensitive to changes in the device over time which can be due to a variation in the surrounding environment like a temperature drift or even a variation in the behavior of the signal to be processed. In non-adaptive digital pre-distortion techniques, the coefficients of the pre-distorter polynomial are usually allocated in a lock up table, while in adaptive ones, these coefficients will be continuously adjusted. In general, both digital and IF pre-distortion are preferred because the components required are usually less robust at high frequencies. Thus, many researchers are aiming at reducing the computational time, optimizing the required memory by the device.

2.6.1.3 Feedforward IMD Components Cancellation in Power Amplifiers

Feedforward linearization is the most cost effective technique that has been extensively employed in small base station amplifiers and handsets. It requires less mathematical computations compared to RF pre-distortion techniques, while providing a higher linearity

with a fast time response and broadband linearization bandwidth [20]. The feedforward linearizer consists of two fundamental loops, the signal cancellation loop and the IMD cancellation loop as shown in Fig. 2.8 [21]. IMD is the amplitude modulation of signals containing two or more different frequencies, caused by nonlinearities in a system. Non-linear systems generate harmonics in response to a given sinusoidal input, meaning that if the input of a non-linear system is a signal of a single frequency F1, then the output is a signal which includes a number of integer multiples of the input frequency signal. These multiples are referred to as high order IMD products. The third order IMD product is the most significant, since it is located at a near by frequency from F1. A power splitter is inserted at the input of the power amplifier to split the signal among two paths: the main path; and the auxiliary path. At the main path the signal is amplified then passed through a coupler that feeds the first cancelation loop, followed by a delay line and a second coupler feeding the second loop. In the auxiliary path, the signal passes through a phase shifter and a fixed delay line to compensate for the phase and delay encountered by the power amplifier in the main path. The two paths are subtracted and the intended signal to be transmitted is cancelled leaving a lower amplitude replica of the IMD components. This replica is amplified in the auxiliary path of the second loop using a small power amplifier. The phase shift and delay in the two paths are matched using a second phase shifter and fixed delay line. The output of the second auxiliary path is then coupled to the main signal path, while cancelling out the IMD components totally from the output signal.

The efficiency of feedforward techniques depends on three main factors: loop imbalances, device losses and the type of the auxiliary amplifier used. The distortion introduced by the auxiliary power amplifier is usually insignificant as it operates at very low power input levels, which make it sufficient to achieve good cancellation. An efficient feedforward requires having the exact same amplitude, group delay and opposite phase for all active paths. Furthermore, power amplifiers can be dynamic in various ways due to either thermal effects, aging and bias point. Hence, adaptive techniques are needed to maintain

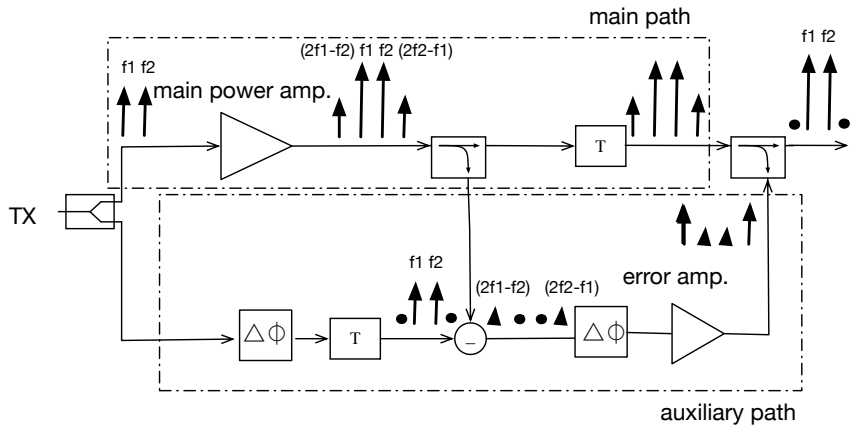

Figure 2.8: Feedforward IMD components cancellation in power amplifiers [21].

Tuning range (MHz)	Two-tone separation	IMD cancellation	Phase shifter method
2010- 2205	10 MHz	15 dB	varactors [24]
2140	15 MHz	15.2 dB	group delay [23, 20]
1700- 1900	20 MHz	25 dB	phase equalizer[25]
1500- 2400	2 MHz	17- 25 dB	LH T-lines (2015)[22]

Table 2.5: Performance comparison of four different IMD feedforward cancellation techniques.

the performance throughout the system life time. Feedforward can provide a broadband linearization when compared to other digital pre-distortion techniques. Phase shifters and amplitude modulators with broadband characteristics are the key components that facilitate tunable broadband characteristics in the feedforward approach. Table. 2.5 combines the performance results of feedforward techniques implemented using different types of phase shifters, which indicates that feedforward techniques can achieve more than 15 dB cancellation for the IMD components located at a frequency separation ranging between 20 down to 2 MHz. In addition, the same IMD cancellation performance can be tuned over a 900 MHz band when passive linear phase shifters are employed as presented in [22].

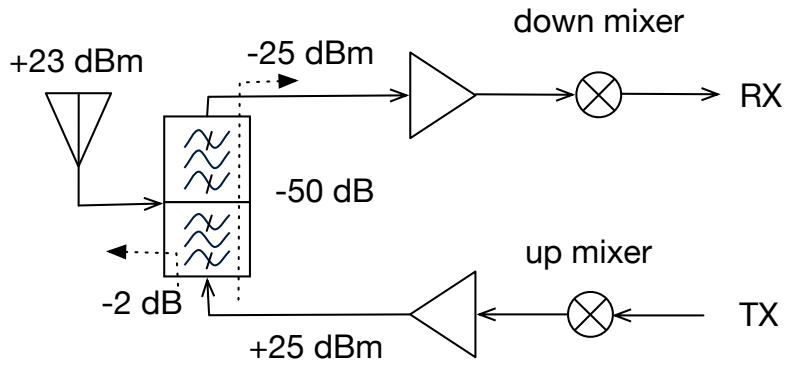

Figure 2.9: Interference due to transmit signal leakage in FDD LTE transceivers [26].

2.6.2 Existing Solutions for Transmitter Leakage

Some LTE transceivers operate in frequency division duplex (FDD) mode, which allows for simultaneous functioning of both the transmitter and receiver. Knowing that the level of the transmit power exceeds that of the receiver by more than 100 dB, insufficient isolation within the duplexer connecting the transmit and receive chain to the antenna will lead to a significant leakage of the transmitted signal into the receiver. Impedance mismatches at the antenna port can further increase the level of the leaked transmit signal. The level of the leakage power is not only a function of the transmit signal power, but also the duplex separation between the transmitter and receiver bands. The power leakage of the transmit signal into the receiver is generating the second type of interference signals known as self-interference. Self-interference presents a particularly challenging issue especially when dealing with RF bands with a small duplex separation, since not only the fundamental components of the transmit signal interfere with the receiver, but also the OOB emissions of the transmit signal fall directly into the receiver band. In this case, a cross-modulation becomes possible as the interference signals mix together to generate in-band intermodulation distortion products. Fig. 2.9 shows a simplified block diagram of the transceiver that illustrates the leakage mechanism or the self-interference between the transmitter and receiver [26].

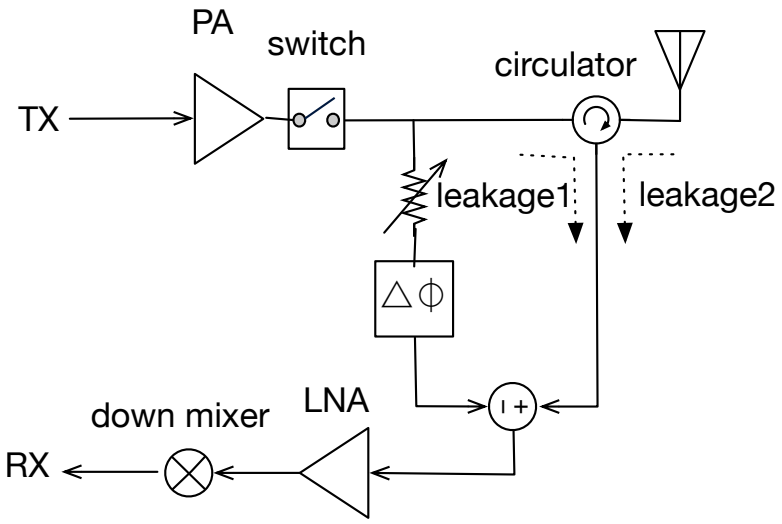

Figure 2.10: The block diagram of direct coupling compensation for leakage suppression in RFID [27].

2.6.2.1 Direct Coupling Compensation

Direct coupling compensation is the typical self-interference cancellation technique used in RFID readers. RF circulators are one example of the type of duplexers used in RFID readers. They are known to provide from 15 dB up to a maximum of 25 dB isolation in practice, which is not sufficient to avoid the self-interference issues. In these types of transceivers, there are usually two sources for the transmitter leaked signal which are referred to in Fig. 2.10 as 'Leakage 1' and 'Leakage 2'. 'Leakage 1' occurs due to the insufficient isolation of circulators, while 'Leakage 2' is due to the mismatches at the antenna port. Direct coupling compensation system for self-interference signal cancellation can be demonstrated using only passive RF components. Fig. 2.10 shows the block diagram of a self-interference cancellation system. It uses a three port ferrite circulator to route the TX and RX signals to and from the antenna, in addition to variable attenuators and phase shifters. The practical implementation of this technique faces the complexity of precisely controlling both the phase shifters and attenuator. In the work reported in [27], a micro-controller was used to tune both elements and more than 36 dB

cancellation for the leakage signal is achieved. This technique works well with narrow band receivers, but rejecting wideband self-interference signals in receivers becomes more challenging.

2.6.3 Existing Solutions for Inter-Channel Interference

Despite allocating RF band gaps between different neighboring channels, near by transmitters form a common source of interference to RF receivers, which is referred to as inter-channel interference. The severity of inter-channel interference effect on RF receivers increases at smaller frequency offsets between the victim receiver and the carrier frequency of the neighboring channel. The interference issue in the 700 MHz spectrum, which is the main topic in this thesis is an inter-channel interference type. Some research work has been done for managing inter-channel interference, which is sometimes referred to as out of band blockers. This subsection studies three different approaches which are active feedforward interference cancellation, active feedback cancellation and N-path blocker filtering.

2.6.3.1 Active Feedforward Interference Cancellation

The approach of implementing a feedforward cancellation loop for out of band blockers was adopted in 2006 by R. Gharpurey et. al. [28]. The loop is used to generate a replica of the interfering signal which is subtracted from the total received signal at the output of the LNA, in order to relax the linearity requirement of the down-conversion mixers. The system architecture of this cancellation loop is illustrated in the block diagram in Fig. 2.11. The main path is formed of the front-end differential LNA and down-conversion quadrature mixers. The auxiliary path is formed of down-conversion mixers connected to the input of the main path, high-pass filters (HPFs), baseband amplifiers, phase shifters and up-conversion mixers connected to the output of the LNA.

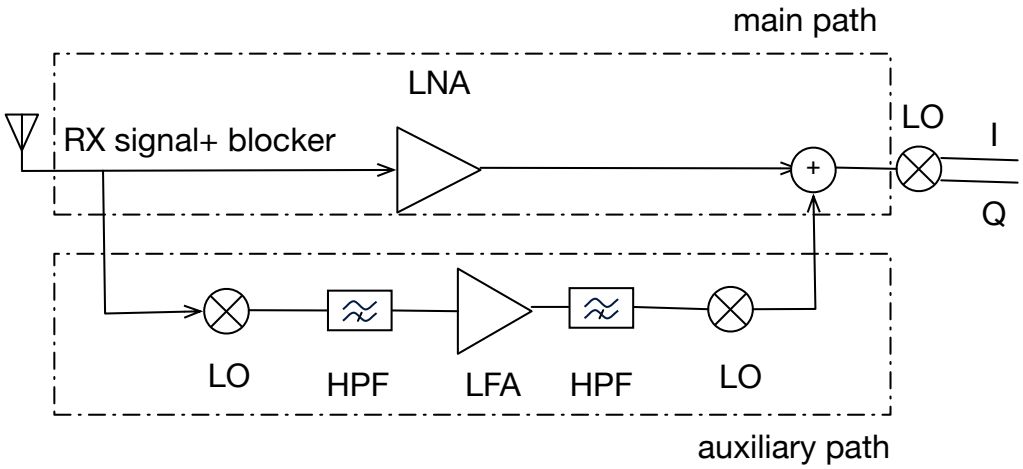

Figure 2.11: Active feedforward interference cancellation architecture for narrow band receivers.

The incoming signals are down-converted to baseband in the auxiliary path with a local oscillator (LO) frequency identical to that used in the main path of the receiver. The desired signal is attenuated using a high pass filter at baseband leaving the interferers at the input of the base band amplifier. The interferers are then amplified, applied to another passive high pass filter and up-converted to the original RF frequency. The second high pass filter is used to ensure attenuation of in-band non-linear products and noise generated by the baseband amplifiers and the down-converter mixer at the input of the up-converter. The output of the auxiliary path is then combined with the output of the LNA with a 180 degree phase shifter between the two paths. The attenuation for interfering signals again depends on the degree of phase and amplitude matching between the two paths.

Active feedforward cancellation has been tested using off-the-shelf components in [29], and the test results have shown 23.5 dB and 26.2 dB nulls at $\pm$23 MHz away from the carrier frequency of the receiver. The noise level increased dramatically above all the frequencies excluding a 4 MHz band centered at the carrier frequency of the receiver. The down conversion mixers present a large contribution to the increase of the noise level in

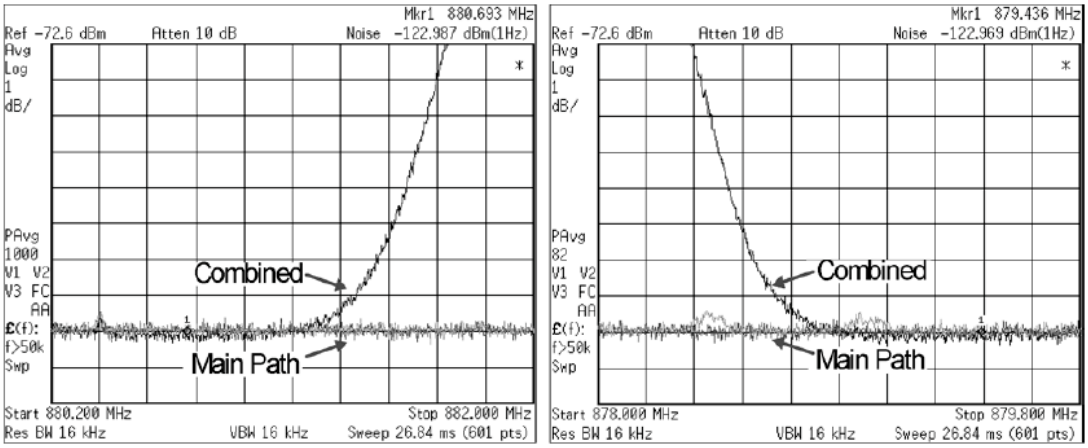

Figure 2.12: The measured output noise of the main path and combined paths in the upper (a) and lower (b) sidebands of the carrier frequency (880 MHz) [29].

the system. Fig. 2.12 shows the measured noise of the main path and the combined path, which is the main path together with the auxiliary path when the interference cancellation loop is active. A linearity test was also conducted resulting in a 1 dB compression point of -29 dBm, which indicates that this technique isn't valid for high power interference signals. Moreover, this technique can be used by RF receivers operating with bandwidths less than 5 MHz, and can handle only narrow band interferers. Although increasing the number of auxiliary loops has shown to form multiple nulls, it can only be used for multiple narrow interferers but not wideband modulated interference signals.

2.6.3.2 Active Feedback Interference Cancellation with No Amplitude Matching

In contrast to the feedforward cancellation system presented above, this active technique suggests the use of feedback loops for cancelling out of band blockers. Active feedback interference cancellation techniques are used to eliminate the amplitude matching condition between the main and the auxiliary paths, as reported in [30]. The system architecture of the feedback cancellation loop is shown in Fig. 2.13. Unlike feedforward loops, this technique doesn't depend on exact gain or phase matching of the LNA and filter core

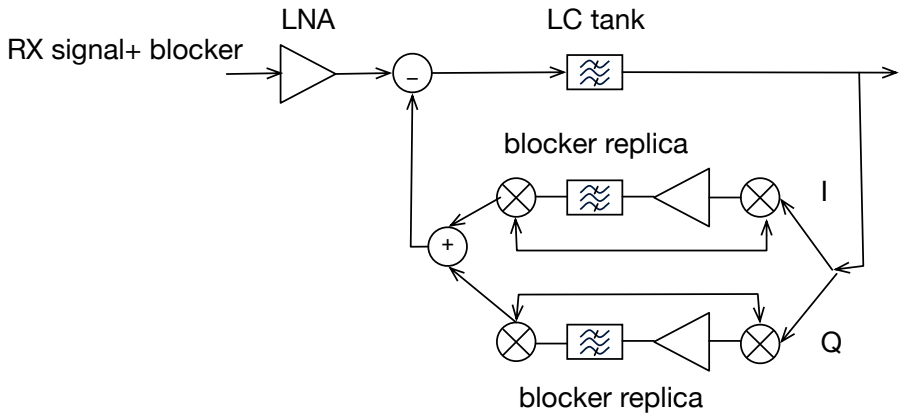

Figure 2.13: Receiver feedback loop for out of band blocker filtering with no amplitude matching [30].

paths. The selectivity of the feedback method only depends on the gain in the feedback path which is easier to adjust. First, the incoming signal together with the interference signal are amplified by an LNA with LC tank load. The output signal is fed into the active cancellation filter core, where it is down-converted into an intermediate frequency (IF) by the receiver local oscillator signal. The wanted received signal is filtered out using a high pass filter leaving a blocker replica, which is then up-converted to RF and subtracted from the total received signal at the output of the LNA. This technique can handle high power blocker as it was tested using a -15 dBm GSM modulated blocker located at 20 MHz away from the carrier frequency of the wanted signal (1.9 GHz) [30]. The test results achieved more than 16 dB attenuation for the blocker, but the noise level at the up conversion mixer has increased by more than 10 dB. The design of the IF filter bandwidth in the feedback chain proved to be critical since it controls the stability of the feedback loop. Similar to the past active feedforward interference cancellation, this system is valid for only narrow band signals.

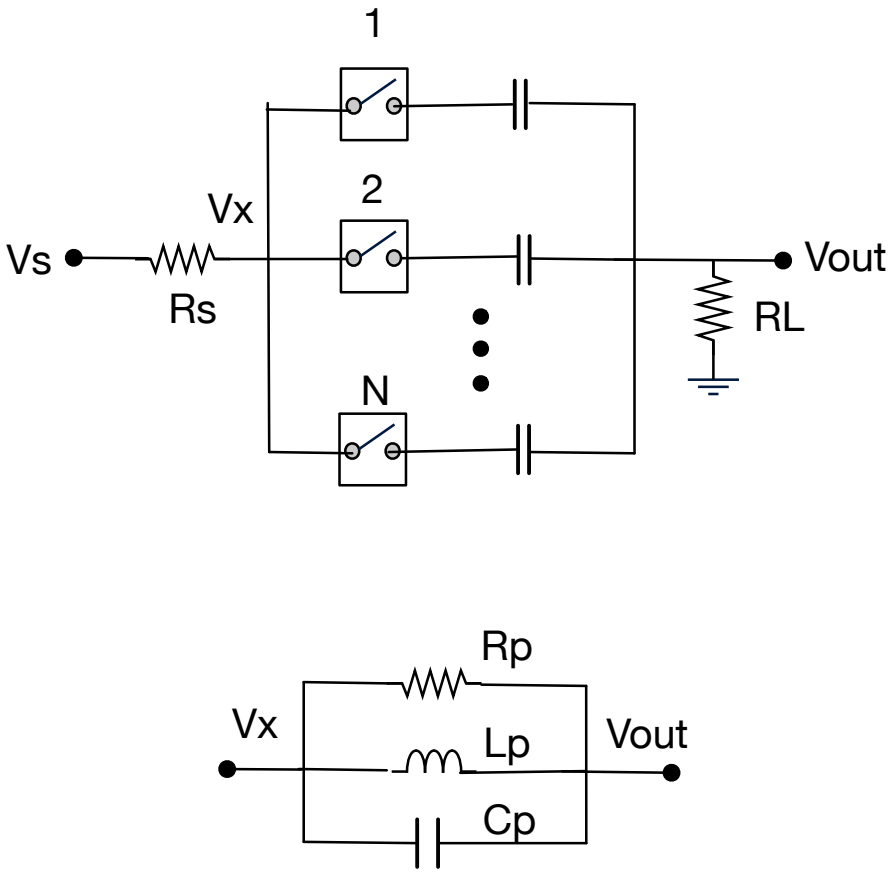

Figure 2.14: The RLC circuit model of N-path notch filters [31].

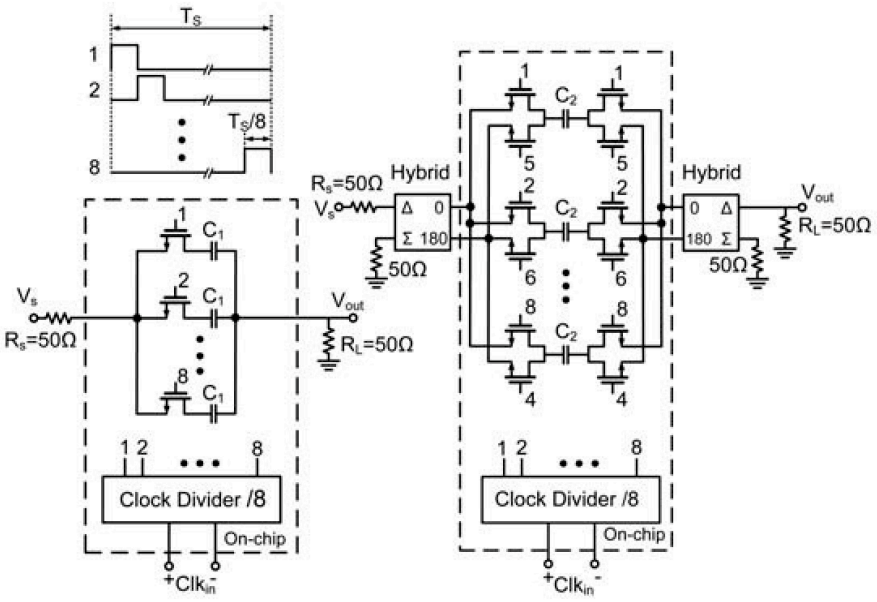

(a) (b)

Figure 2.15: Schematic of the implemented 8-path single ended and differential notch filters [32].

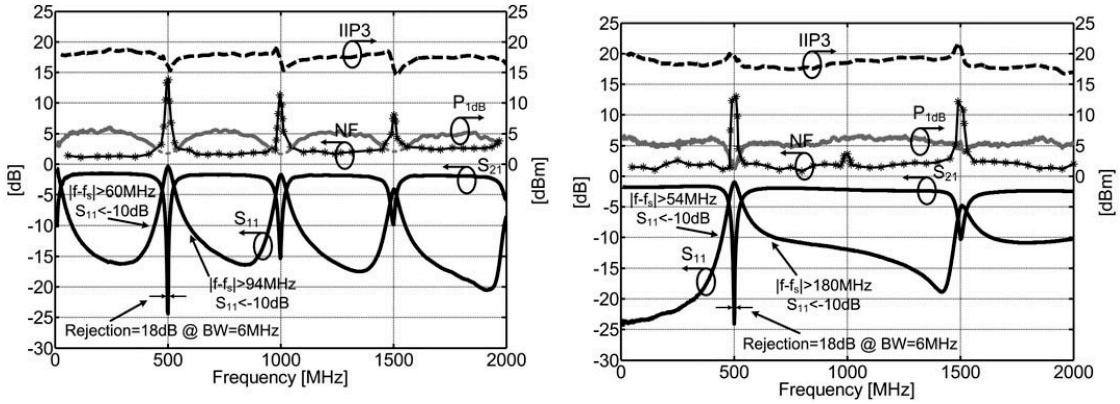

(a) (b)

Figure 2.16: Measurements of 8-path single ended (a) and differential (b) notch filters [32].

2.6.3.3 N-Path Blocker Filtering

N-path filtering is the most recent proposed technique for handling high-power interference in RF receivers. It uses the N-path concept, which was first introduced in [31], where filtering is performed in the baseband without the use of down or up conversion mixers. Unlike most baseband filters, they are characterized by a high 1 dB compression point and also low noise property.

A block diagram for the RLC circuit model of N-path filters is illustrated in Fig. 2.14. The input signal is down-converted, high-pass filtered and then up-converted to the same frequency band as the input experiencing a notch filter at multiple frequencies [32]. The down-converting mixers are realized by switches driven by N multiphase clocks with a duty cycle of 1/N. A simple RC network is used to construct the high pass filter, while the up converting mixers are implemented using a wired-OR connection at the output node. A typical transfer function of the notch filter is also plotted in Fig. 2.16 showing the rejection at the switching frequency (fs) and its harmonics. The multi-path switched capacitor in Fig. 2.14 can be modeled as a parallel RLC tank circuit with a resonance at fs. Rp, Cp and Lp are the parallel resistance, capacitance and inductance values of the RLC tank circuit. Rp and Cp are constant for a given number of paths but the inductor varies with fs. A fixed RC value imply a constant bandwidth for the notch formed. According to the equations in [32], increasing N will increase the parallel resistance which further increases the rejection of the notch filter. Similar to the N-path bandpass filter in [33] harmonic mixing might happen with (N-1)th and (N+1)th harmonics of fs. Therefore increasing the number of paths not only increases the amount of rejection at fs but also moves the folding-back components further away.

Fig. 2.15 shows a schematic for the implemented 8-path single-ended and differential notch filters, and Fig. 2.16 shows the measurements of the two filters. The two filters have obtained a notch with 18 dB rejection over a 6 MHz bandwidth, in addition to a 2

dB in-band insertion loss. Measurements have also proved that N-path filters are able to overcome the drawbacks of baseband filters for achieving a noise figure of less than 3 dB and an IIP3 of more than 17 dBm. On the other hand, these filters can't handle close interference signals, as the measured roll-off rate falls below 0.13 dB per MHz, which is only sufficient for blockers appearing at more than 60 MHz frequency offset.

2.6.4 Limitations of Existing Interference Management Techniques

All the techniques discussed have shown some attractive high performance results in rejecting interference signals, however they have resulted in some drawbacks that limits their use in managing interference in the 700 MHz spectrum, which is the main focus of this thesis.

Starting with the solutions proposed for inter-channel interference signals in subsection 2.6.3, since public safety interference is itself an inter-channel interference issue. The benefits and drawbacks of these solutions are summarized as follows:

- Active feedforward interference cancellation can handle interferers located at small frequency offsets. In this section, it has shown above 20 dB suppression for interferers appearing at 23 MHz offset. On the other hand, active feedforward cancellation has dramatically increased the level of noise introduced to the system. Active feedforward cancellation can be only applied on low power and narrow band interference signals, which is seen as a limitation for this technique.

- Active feedback interference cancellation have managed to handle large power interferers, but at the expense of a further increase in the level of noise and system instability.

- N-path filtering has succeeded in performing baseband filtering without the use of up/down conversion mixers. This makes it able to handle high power interference signals without degrading the noise level of the system. By applying baseband

filtering, this method has also allowed rejecting wideband modulated interference signals with 6 MHz bandwidth by 18 dB, as shown in the above example. The main drawback of this method is that it can't handle small frequency offsets, as the minimum frequency offset that can be obtained is 60 MHz [32].

Subsection 2.6.1 and 2.6.2 have discussed solutions for unwanted emissions and transmitter leakage, which are different sources of interference compared to what this thesis is looking at, however these solutions have proved how passive RF signal cancellation system can avoid all the drawbacks and limitations of baseband filtering and active cancellation techniques. RF solutions can avoid the added noise, system instability, and non-linearities which make the system able to handle large power interference signals. RF solutions also combine the benefits of active cancellation and baseband filtering, as it has shown to provide high rejection to interference signals located at small frequency offsets. In subsection 2.6.1, the IMD components, which were located at small frequency offset (20- 2 MHz) have been successfully cancelled. Furthermore, in subsection 2.6.2, more than 36 dB of signal cancellation for the leakage signals has been obtained by the direct coupling compensation RF system.

Passive RF cancellation system proved to provide a high performance in rejecting interference caused by unwanted emission or leakage signals. These performance results have encouraged investigating the feasibility of constructing a passive RF cancellation system for inter-channel interference in the 700 MHz spectrum, which is the research question of this review. There is one big challenge in applying these RF cancellation systems on inter-channel interference signals, which can be explained as follows:

The solutions in subsection 2.6.1 and 2.6.2 are all based on constructing a replica of the interference signals, which is later cancelled out from the main signal path. Constructing a replica can be more challenging if there is no supplied information on the interfering signal, which is likely the case in inter-channel interference. In other words, the leakage signals and the unwanted transmitter emission interferers are generated internally in the

same transceiver. This facilitates generating an interferer replica, which is a coupled version of the transmitter signal. On the other hand, inter-channel interference are generated from unknown transmitters, thus the only way to form a replica of the interferer is by filtering. RF filtering can be challenging when dealing with small frequency offsets which is the case with public safety interference signals. As a result, a review is conducted on RF filtering structures to assist their feasibility in separating close interference signals with large power and bandwidth (> 10 MHz).

2.7 Review of RF Filters for Inter-Channel Interference

According to the limitations discussed in subsection 2.5.5, existing high Q duplexers in small-cell base stations can't handle large power interference in the Upper-700 MHz band (LTE band 14). Furthermore, the reviewed solutions for inter-channel interference in section 2.6 have also shown limitations with the power levels of interference signals and the frequency separation between their location and the receiver band. As a result, a passive RF feedforward interference cancellation technique is adopted in this thesis. This technique requires the use of filtering structures for separating interference signals, which can assist in generating a replica for the interferer. Avoiding or reducing the dependency on replying solely on baseband or digital filtering of interference signals can eliminate the limitations of handling large power interference signals. Another advantage, it can also eliminate the noise introduced by mixers and improve the linearity of the receiver.

To implement this RF cancellation, the design of the filter is critical. The most essential characteristics for the RF filter used in separating close interference signals is the high roll-off rate, as it allows for fast switching between the pass and stop band. Knowing that interference signals can appear at frequency separation of less than 20 MHz away from the receiver, more than 1 dB per MHz roll-off rate is going to be set as a first requirement to successfully generate a replica for the interference signal. The rejection bandwidth of

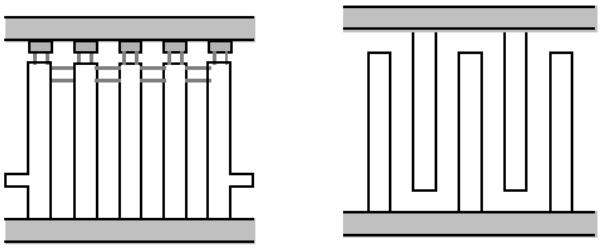

(a) (b)

Figure 2.17: The structure of combline (a) and inter-digital (b) filters.

the filter is another important parameter. For example, the 700 MHz spectrum involves LTE wideband modulated signals with 5-10 MHz bandwidth. The insertion losses of the RF filter needed can however be tolerated, since the separated interferer signal will have to undergo amplification whether the losses exist or not. However, low insertion losses are still seen as an advantage for the filter. The physical size of the filter is also a critical parameter, since the whole cancellation system must fit into the size of small base station transceivers.

2.7.1 Combline and Interdigital Filters

Combline filters, which were first introduced by Matthaei in 1963, are one of the most commonly used bandpass filters in many communication systems and other microwave applications. With modern filter synthesis theory, combline filters having elliptic function frequency responses can be realized by using the nonadjacent couplings. Unlike Chebyshev and Butterworth filters, the elliptic function frequency response is known to provide a sharper rejection using the same number of resonating elements (same filter order). Combline filters are constructed using capacitively coupled quarter wave resonators, often with additional lumped capacitive tuning screws for fine adjustment. The quarter wave resonators are implemented using strip transmission lines which are all grounded at the same end forming the shape of a comb, thus referred to as combline filters.

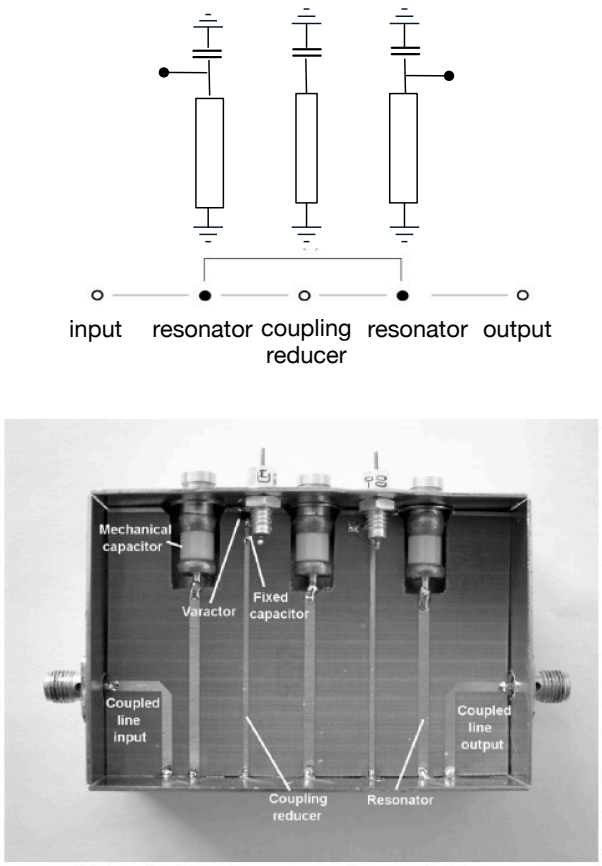

Figure 2.18: A 3rd order suspended combline bandpass filter tuned using a high Q mechanical variable capacitors and varactors [34].

Inter-digital filters can be seen as a miniaturized version of combline filters, since their structures are very similar. It is also composed of coupled transmission line resonators, but here the lines are shorted at opposite ends which makes the structure take the form of interlaced fingers. Inter-digital filters are more efficient in terms of size, when compared to combline filters, however combline filters can easily obtain better selectivity with smaller bandwidth and sharper rejection. The structure of the two filters can be seen in Fig. 2.17.

High performance combline filters are usually implemented using suspended strip line technology. Fig. 2.18 shows an example of a 3rd order suspended combline filter, which was designed for digital TV receivers operating in the UHF band [34]. The filter uses

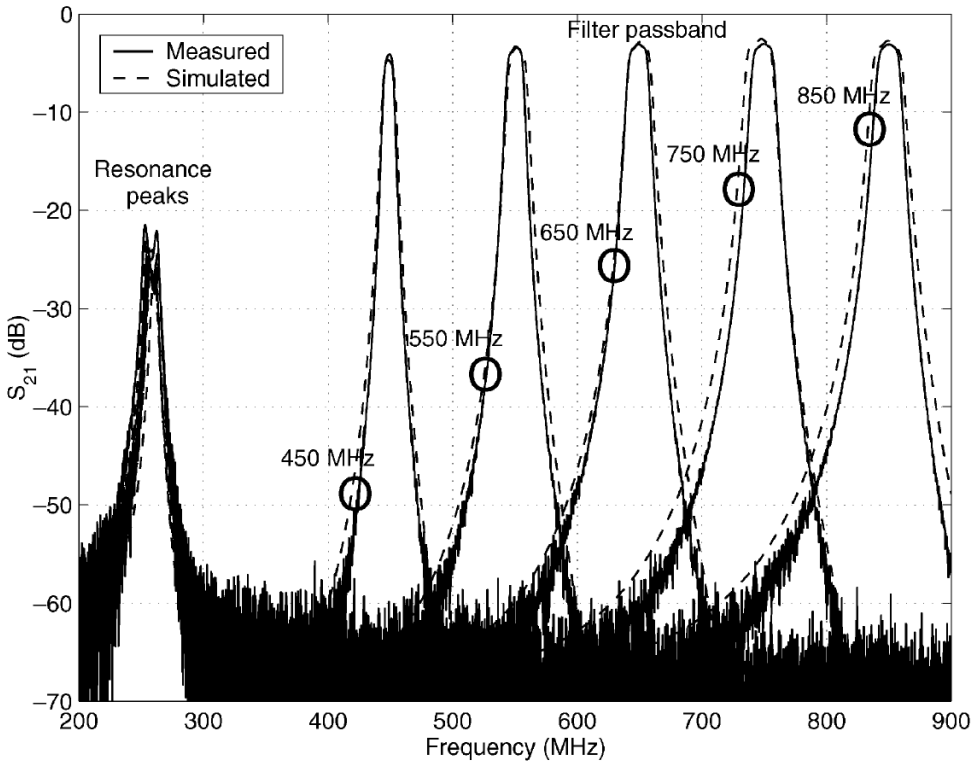

Figure 2.19: Measurements of a 3rd order suspended combline bandpass filter with varactor tuning.

high Q mechanical capacitors to tune the frequency response. Additional transmission lines (coupling reducers) are introduced between the quarter wave resonators to readjust the coupling at different resonance frequencies. The adjustment is made using different voltage biased varactors, as shown in Fig. 2.18. The dimensions of the aluminum box are 50 x 65 x 250 mm. Fig. 2.19 shows the measurements of the suspended combline filter tuned from 470 MHz up to 862 MHz. Measurements indicate more than 50 dB rejection with 1 dB per MHz roll-off rate. The results also show more than 5 dB insertion loss and a minimum 3 dB bandwidth of 10 MHz at 450 MHz. As the resonance frequency increases, the 3 dB bandwidth increases to values above 30 MHz and the roll-off rate degrades as shown in the figure.

Suspended strip combline filter proved to provide the rejection characteristics perfor-

mance requirements for separating interference signals in the 700 MHz spectrum. Yet, the bulky size of the suspended strip line box does not make it any better than microwave air cavity filters apart from featuring a more practical tuning capability.

2.7.2 Notch Filters

A notch filter can be defined as a band-stop filter with a narrow stop band. Notch filters have been extensively used in suppressing narrow band RF interference signals in base station transceivers. A microstrip notch filter is usually implemented via a resonating structure. The quality factor (Q) of the resonance determines the bandwidth of the notch in the frequency response. The higher the Q, the deeper the notch, and this can be useful when targeting large power interference signals, where high levels of attenuation are required. A simple form of a microstrip resonator is constructed using quarter wave transformer, which is not recommended for use at low frequencies as the length of the line becomes a direct function of the operating wavelength. Microstrip patches with different shapes have also been used in implementing notch filters or notch resonators. Examples include Ring resonators, T-shaped resonators, L-shaped resonators, ...etc [35, 36, 37]. Similar to quarter wave transformers, the dimensions of these patches remain a function of the operating wavelength, however the overall circuit size of notch filters constructed using these shapes is reduced.

Microstrip notch filters usually offer high tuning capabilities for their frequency response, unlike most of the band-stop filters, thus becoming an ideal candidate for matching the nature of some interference signals appearing at different frequency locations. In [38], a tunable notch filter is implemented using RF-MEMS capacitors (Micro-electro-mechanical switched) to suppress interference due to power leakage between the TX and RX in a WCDMA transceiver operating at 1.92-1.98 GHz. The high quality factor of the MEMS capacitors used enabled the notch filter to achieve more than 25 dB rejection over a 5 MHz bandwidth. On the other hand, the roll-off rate of the filter is very poor as shown

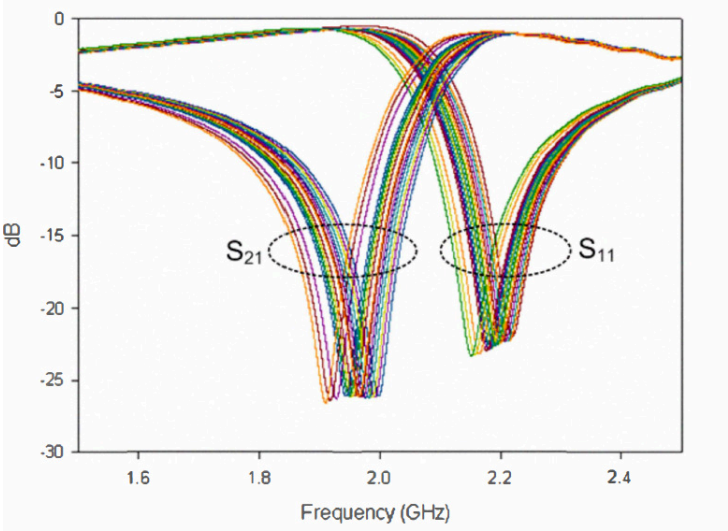

Figure 2.20: The measured frequency response of the MEMS capacitor tuned notch filter presented in [38].

in Fig. 2.20. In fact, a high roll-off notch filter can be obtained by employing high quality factor resonators, which are usually realized in non-planar bulky structures.

2.7.3 Lumped Distributed Capacitively Coupled (LDCC) Filters

Lumped distributed capacitively coupled (LDCC) filter is a new bandpass filter topology, which was first presented in [39]. This filter is constructed using coplanar waveguide short

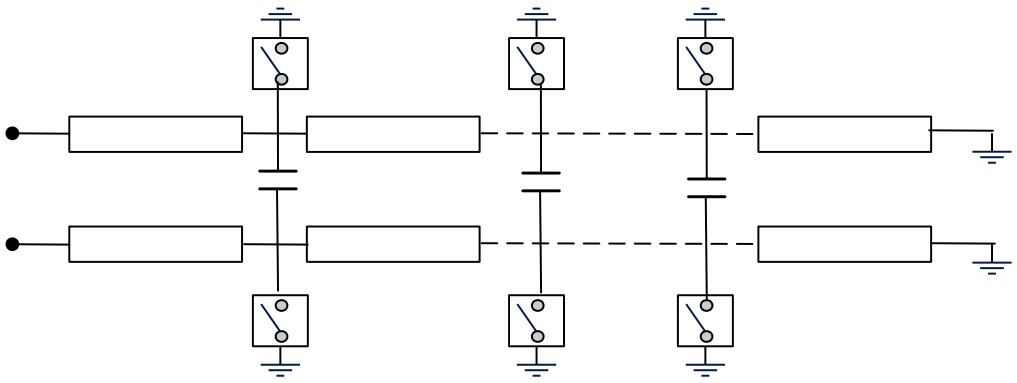

Figure 2.21: Schematic of one LDCC pair of segmented transmission line stub [39, 40].

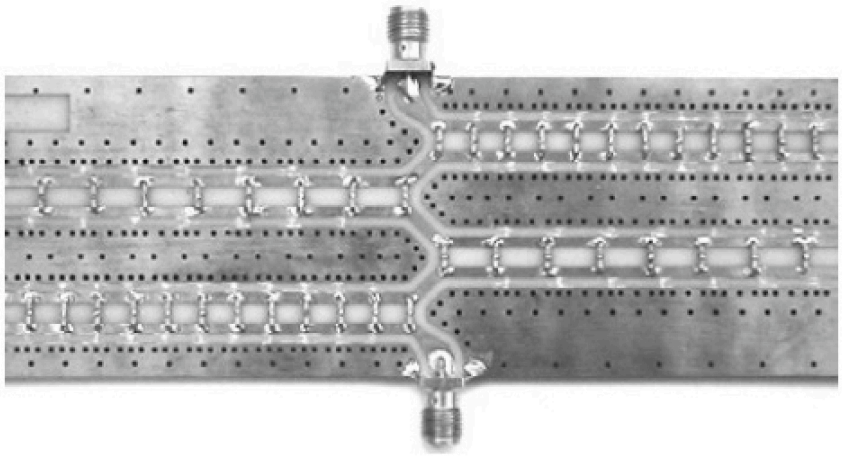

Figure 2.22: A fabricated 3rd order LDCC bandpass filter [39, 40].

ended stubs, as it allows for well-defined and easily adjustable ground connections for the resonators. Each stub is composed of 16 segments which are connected via MEMS switches. An example of a 3rd order LDCC, which is composed of four pairs of segmented stubs, is designed, fabricated and tested in [39, 40]. Fig. 2.21 shows a schematic for one LDCC pair. MEMS switches are used to tune the center frequency of the filter from 350 MHz (16 segments) up to 1.4 GHz (4 segments) while keeping a constant fractional bandwidth (17- 20%). Surface mount capacitors are also inserted along the two parallel stubs in each LDCC pair. The capacitors are used to slightly adjust the bandwidth of the filter. A diagram for the fabricated filter is shown in Fig. 2.22 whose dimensions are 44 x 240 mm. Unlike, suspended strip combline filters, LDCC is printed on a planar board with no metal box nor mechanical capacitors, which has largely reduced the weight of the board, however the physical dimensions of the filter are still similar [39, 40].

The measurements for the 3rd order LDCC bandpass filter example in [39, 40], showed more than 60 dB rejection at all switching states, and a 5 dB insertion for the smallest bandwidth in curve no. vi (5.7 %), as shown in Fig. 2.23. The measurements also indicate a roll-off rate ranging from 0.35 to 0.5 dB per MHz. This roll-off rate means that this

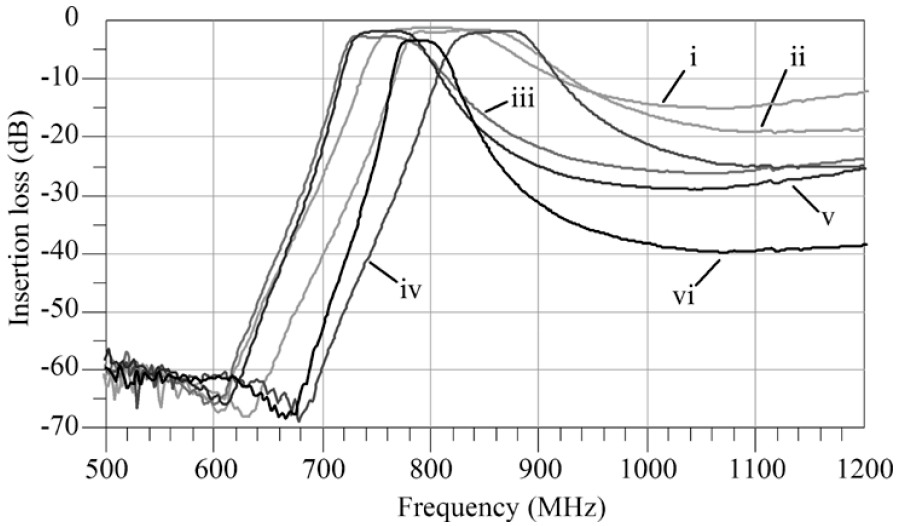

Figure 2.23: Measurements of a 3rd order LDCC bandpass filter at different switching states [39, 40].

filter can provide a maximum rejection of 10 dB only for an interferer located at 20 MHz away from the victim receiver, which is not sufficient to meet the rejection requirements discussed earlier.

2.7.4 Low Profile Microstrip Filters with High Roll-Off Rates

Both the LDCC and the suspended combline bandpass filter have shown very good rejection performance, but with bulky and large circuit sizes. These structures are composed of single dielectric substrate with two fine layers of metal on the top (signal line) and the bottom (ground) of the substrate material. In general, the rejection performance characteristics of RF filters can be judged by their corresponding low pass prototype. Therefore, low pass microstrip filters are reviewed in this section. The conventional method of constructing a low pass-low profile microstrip filter is the stepped impedance method, which provides only slow switching from passband to stop-band [41]. The roll-off rate can be improved by introducing more elements, however this increases the size of the filter and the insertion loss in the passband. Recently, different methods have been proposed and

	Cutoff freq. (GHz)	Roll-off rate (dB/ MHz)	Max. attenuation (dB)	size (mm)
[42]	3.3	0.084	20	10.0 × 10.9
[43]	1.57	0.03	15	17 × 15.6
[44]	2.00	0.031	10	5.4 x 13.49
[45]	0.8	0.095	20	34.6 x 70.95
[46, 47]	2.5, 2.3	0.1	16, 18	17.6 × 12.2
[48]	5.58	0.084	15	17.4 x 12.2
[49]	2.72	**0.125**	23	17.6 x 12.8

Table 2.6: A performance comparison between a number of low pass microstrip filters.

developed to implement low profile microstrip filters with better rejection performance by utilizing different approaches for constructing their resonating element. Some of these approaches are listed as follows:

1. Hex-angular shaped resonator [42].

2. Polygonal patch resonators with meander transmission line [43].

3. Modified stepped impedance hairpin resonators [44].

4. Stub loaded coupled-line hairpin unit [45].

More methods have been developed to improve the roll-off rate by cascading multiple patch resonators on high impedance microstrip transmission line [46, 48]. Hence, a performance comparison is conducted between all the above low pass microstrip filter designs in Table. 2.6. Each of the filter structures in the table are offering a compact size with reduced complexity and fabrication costs, when compared to LDCC and suspended stripline type of filters. The results in Table. 2.6 have shown high attenuation levels for small filter dimensions. However, all the filters have shown poor rejection roll-off rate, which is very important in selecting an RF filter for the feedforward interference cancellation system. Consequently, this thesis will be looking at how to design a compact low-profile passive filtering structure that can provide sharp rejection, in specific a high roll-off rate of more than 1 dB per MHz.

2.8 Conclusion

Interference management in the 700 MHz spectrum requires increasing the stop band attenuation of the receiver filter by more than 29 dB to meet the power requirements in the 3GPP defined standards for LTE systems. High Q duplexers in wide and local area base stations have shown some limitations in providing such additional rejection in the presence of strong interference signals. Although some researchers have managed to improve the quality factor of air cavity resonators using corner rounding and hybrid configurations with dielectric materials to reach 100 dB. Cavity filters can only assist in handling interference in large cells. Thus a review is made on existing interference management techniques which are grouped according to the source type of interference: neighboring channel interference; transmit power leakage; and unwanted emissions. All the techniques presented have shown some attractive high performance results in rejecting interference signals, and they have also shown some drawbacks that limits their use in managing interference in the 700 MHz spectrum. The review results can be summarized as follows:

1. Neighboring channel interference (inter-channel interference)

    - Active feedforward interference cancellation have shown above 20 dB suppression for interferers appearing at 23 MHz offset. It dramatically increases the level of noise introduced to the system. This cancellation system is only valid for low power and narrow band interference signals.
    - Active feedback interference cancellation have managed to handle large power interferers, but at the expense of a further increase in the level of noise and system instability.
    - N-path filtering has eliminated the added noise. It has the capability of handling large power interferers. It has rejected 6 MHz modulated signals by 18 dB. On

the other hand, it does not allow for small frequency offset as the practical minimum offset is 60 MHz.

2. Transmit power leakage interference (self-interference)

    - More than 36 dB of signal cancellation for the leakage signals has been obtained using a passive RF interference cancellation system. No significant noise is added to the system. No power limitations. Wide band interferers can be handled.

3. Unwanted emissions in the transmit chain

    - More than 17 dB attenuation for IMD components at small frequency offset (20 MHz and down to 2 MHz) can be obtained using RF feedforward cancellation systems. The cancellation system uses one active power amplifier, however the levels of distortion added are insignificant as it operates at very low power input levels.

The solutions for leakage signals and unwanted transmitter emissions have shown no drawbacks, however these solutions only address interference signals that are generated internally in the same system. In order to apply a similar RF feedforward cancellation method, a replica of the interfering signals must be provided. Inter-channel interference are generated from unknown transmitters, thus the only way to form a replica of the interferer is via an RF filtering process. RF filtering can be challenging when dealing with small frequency offsets which is the case with public safety interference signals in the 700 MHz spectrum. This chapter has therefore conducted a second review on RF filters with high rejection characteristics: combline and interdigital filters; LDCC filters; and low-profile-low pass filters. Combline filters implemented using suspended strip line technology have shown an excellent rejection performance, however their size is not compatible with small cell base stations. LDCC and microstrip filters have shown poor roll-off rate in

switching between the pass and the stop band.

The review conducted in this chapter suggests the use of an RF feedforward interference cancellation system for assisting small-cell base stations in rejecting high power interference signals appearing at small frequency separation from the receiver. The next chapter starts by introducing the block diagram of the proposed cancellation system, while listing the specifications and requirements on the RF hardware needed for handling some of the interference scenarios in the 700 MHz spectrum. This spectrum is selected as it presents an exemplar of high power interference with small frequency offsets. The following chapters present new methodologies for constructing low profile microstrip filtering structures with sharp rejection.

Chapter 3

RF Feedforward Signal Cancellation System for Public Safety Interference

3.1 Introduction

This chapter presents the system design for a new feedforward interference cancellation technique employing band-stop resonators. The structure allows the system to fully operate in the RF domain, where signal down conversion is no longer required. Eliminating the digital hardware has the advantage of overcoming distortion due to noise and non-linearities. Like all feedforward loop systems, it consists of two main stages: filtering; and signal matching. Knowing that interferers can appear at only few MHz away from the receiver edge (e.g. < 20 MHz) adds the first key challenge to the design of the RF components in the system. More challenges appear in the second stage where perfect signal matching is indispensable for interferers with dynamic bandwidths and power levels.

The chapter starts by introducing examples of different interference scenarios occurring in the Upper-700 MHz band between commercial LTE mobile base station receivers,

Public Safety Broadband and Land Mobile Radios (LMR). Section 3.3 starts with a basic introduction to the RF feedforward interference cancellation system and operation. Section 3.4 lists the design challenges and performance requirements on each of the RF components employed in the system including the band-stop resonator, phase shifter, amplifier, and couplers. Section 3.5 discusses additional requirements which are necessary to obtain some degree of reconfigurability in pursuance of handling the dynamic nature of interference signals. Section 3.6 discusses the practical implementation of the system by first selecting some of the off-the-shelf RF hardware components, then proposing new design solutions for handling very close interferers.

3.2 Public Safety Interference Scenarios in the 700 MHz Band

3.2.1 Interference Between Public Safety LTE and Public Safety Land Mobile Radio

As assigned by the FCC, the new broadband Public Safety (PS) LTE is going to use the frequency band starting from 758 MHz to 768 MHz for the down link (DL) transmission, and the band between 788 MHz and 798 MHz for the upper link (UL) transmission. On the other hand, the LMR band is assigned the frequencies between 769 MHz and 775 MHz. Several LMR channels can transmit/receive at any frequency within the 6 MHz, where each channel holds a very narrow band signal ($\approx$25 KHz). Thus, the LMR receiver operates at only 1 MHz frequency separation from the edge of the downlink LTE signal and at less than 20 MHz away from the upper link LTE. A case study was presented by the US Department of Homeland Security on the potential interference between the two Public Safety operators. The study showed that LMR receiver can exhibit some performance degradation in the presence of the two broadband LTE signals. This is due to the level of these two signals being roughly estimated to be 50 dB and 80 dB higher than the level of the wanted LMR signal for the down link and upper link, respectively. The

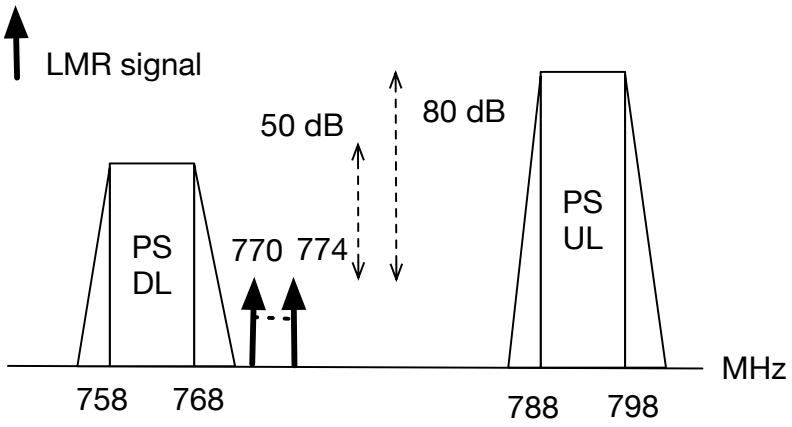

Figure 3.1: Interference between Public Safety LTE and Public Safety Land Mobile Radio signals.

upper link however showed less effect on the performance degradation, because it exists at larger frequency separation compared to the down link signal, as demonstrated in Fig. 3.1.

3.2.2 Interference Between Commercial LTE Mobile Base Station and Public Safety Land Mobile Radio

The commercial mobile base station transmits an LTE wide band signal in the frequency band between 746 MHz and 757 MHz (downlink), which is 12 MHz away from the LMR receiver and only 1 MHz away from the Public Safety broadband downlink. The two Public Safety signals can present some interference on the mobile phone receiver, however the differences between their power levels and that of the received LTE mobile signal are relatively lower when compared to the interference scenarios discussed above. Therefore, the effect of the LMR interference on the performance degradation of the mobile phone receiver is limited.

On the other hand, the uplink mobile signal received by the base station uses the band between 776 MHz and 787 MHz which is only 1 MHz away from the LMR signal.

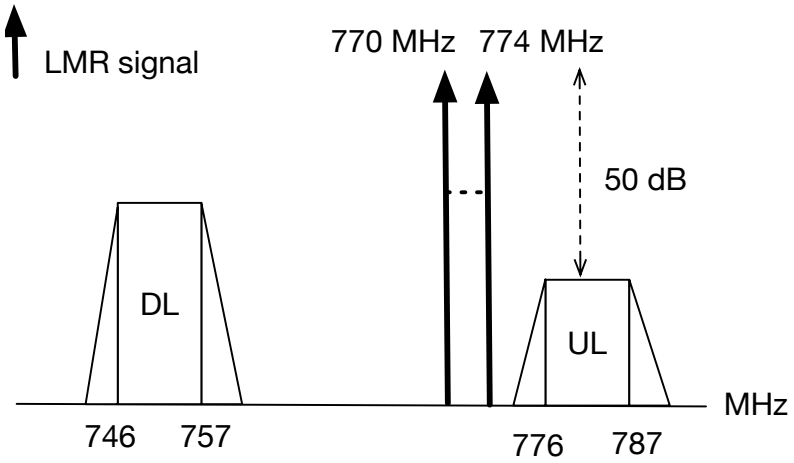

Figure 3.2: Interference between Public Safety LMR signal and the upper link of the commercial mobile band.

In addition, there is a huge differences in the power levels between the two signals, as the LMR can reach the LTE mobile base station receiver at more than 50 dB higher than the wanted signal. This can be considered as the worst case interference scenario in the 700 MHz band, because of the high difference in power levels as well as the very small frequency separation, as explained in Fig. 3.2.

3.3 System Overview

Fig. 3.3 shows the block diagram for the new feedforward interference canceller system consisting of a bi-directional RF coupler, band-stop resonator, phase shifter, fixed delay, fixed gain amplifier and signal subtractor. The system is located between the output of the receiver antenna and the low noise amplifier (LNA), in order to prevent high power interferers from desensitizing the LNA. The signal to interferer power ratio is visualized at different parts of the above diagram in the form of arrows labeled “i” and “d”, which refer to interferer and desired signals, respectively.

The operation of the system is explained in the following steps, given that the carrier

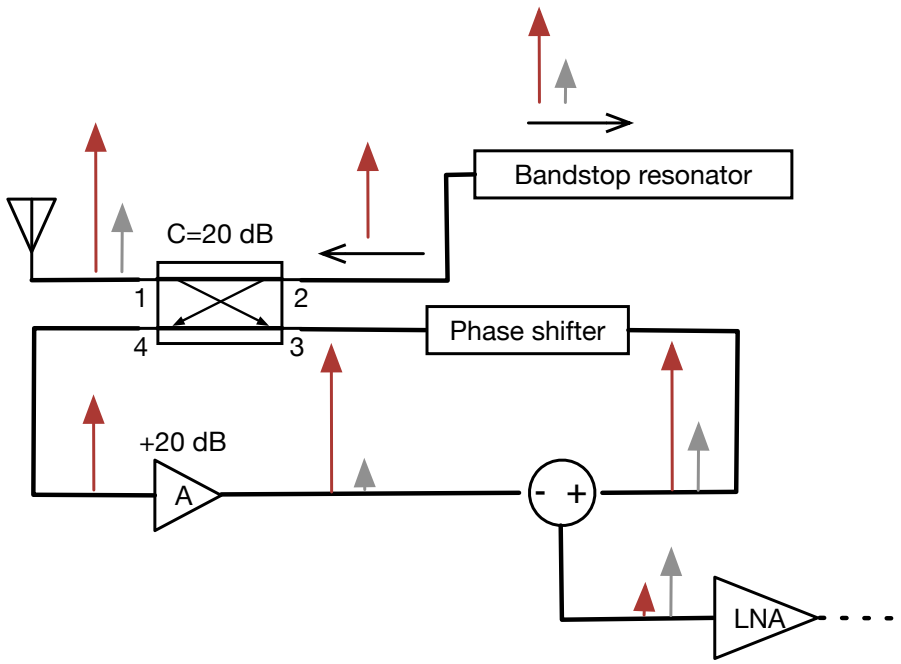

Figure 3.3: The block diagram for the setup proposed to suppress out of band RF interference signals using bandstop RF resonators.

frequency of the interferer is f1, while that of the desired signal is f2:

1. The total received signal first passes into the input port of the coupler named “Port 1”, whose coupling coefficient is set to 20 dB. The coupler is operating in the forward direction having “Port 2” as the coupling port, “Port 3” as the through port , and “Port 4” as the isolation port.

2. A fraction of the two signals now reaches the band-stop resonator, whose function is to separate the two. The separation is achieved by setting the stop-band at f1 and the pass-band at f2. Hence, the fraction of the interferer is reflected back to the coupler and the fraction of the desired received signal passes through the resonator, where it is absorbed by the ground terminal of the resonator.

3. Now, the coupler operates in the reverse direction as the fraction of the interferer forms a second input to the coupler at Port 2. In the reverse operation, Port 4

becomes the through port at which the fraction of the interferer signal reaches the amplifier.

4. The amplifier has a fixed gain of 20 dB, which is set to reconstruct the interferer signal forming the auxiliary path of the feedforward system. The gain of the amplifier is selected to compensate for the coupling coefficient of the coupler as well as any losses encountered in the band-stop resonator. In this case, a 20 dB gain amplifier is selected, because the resonator is considered to be an ideal component, whose losses are equals to zero.

5. The total received signal first passed into the coupler reaches Port 3 with zero attenuation assuming the coupler is lossless. The phase shifter and fixed delay forms the main path of the feedforward system. Their function is to compensate for both the phase and time delay encountered by the signals in the auxiliary path through each of the coupler, the band-stop resonator and the amplifier.

6. Subtracting the signals in the auxiliary path and the main path eliminates the interferer leaving the desired signal at the input of the LNA.

For this new feedforward cancellation system to work, stringent requirements on the design and performance of each of the system components need to be met.

3.4 System Performance Criteria and Requirements

3.4.1 Band-Stop Resonator

A band-stop resonator can be defined as a band-stop filter with one port terminated by either a short or an open circuit. The network representation of a band-stop resonator is illustrated in Fig. 3.4 together with the typical frequency response for the reflection coefficient from port1. The stop band represents the range of frequencies at which the signal is

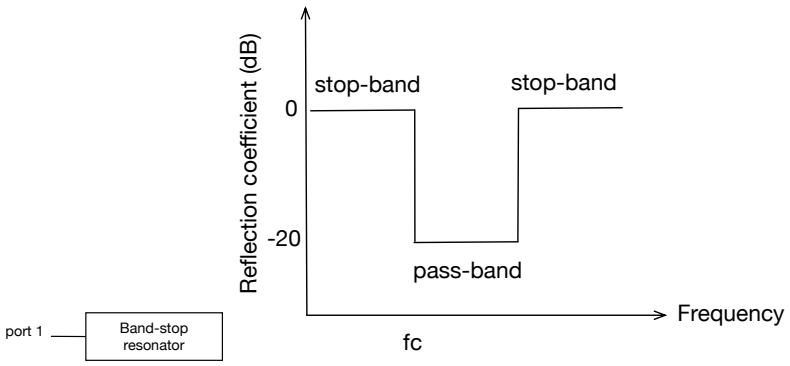

Figure 3.4: Network representation of band-stop resonators and the typical frequency response for the reflection coefficient from port1.

totally reflected at port1. On the other hand, the signals are absorbed in the frequencies above the cut off frequency forming the pass band of the resonator. The function of this component is to separate the interferer from the desired receiver signal. Seeing that the two signals are only a few MHz away, high selectivity becomes the most essential design requirement. The stop band is used to reflect fully the interference signal at the input, while the pass band absorbs the desired receiver signal to prevent it from being reflected back to the coupler. The more the receiver signal is absorbed, the less distortion introduced by the feedforwa §§rd system. Therefore, more than 15 dB attenuation is needed in the stop band of the resonator. In addition, the stop band must be wide enough to cover the total bandwidth of the receiver signal (e.g. > 10 MHz). Sharp rejection is an important criteria in the design of these resonator, where more than 1 dB per MHz roll-off rate is required to separate two signals that are less than 15 MHz away. Low insertion loss, small circuit size and low fabrication costs are also desirable to improve the system efficiency.

3.4.2 Phase Shifter and Fixed Gain Amplifier

The accuracy and precision of phase shifters and the fixed gain amplifier are critical design parameters, due to the fact that signal cancellation requires perfect signal amplitude

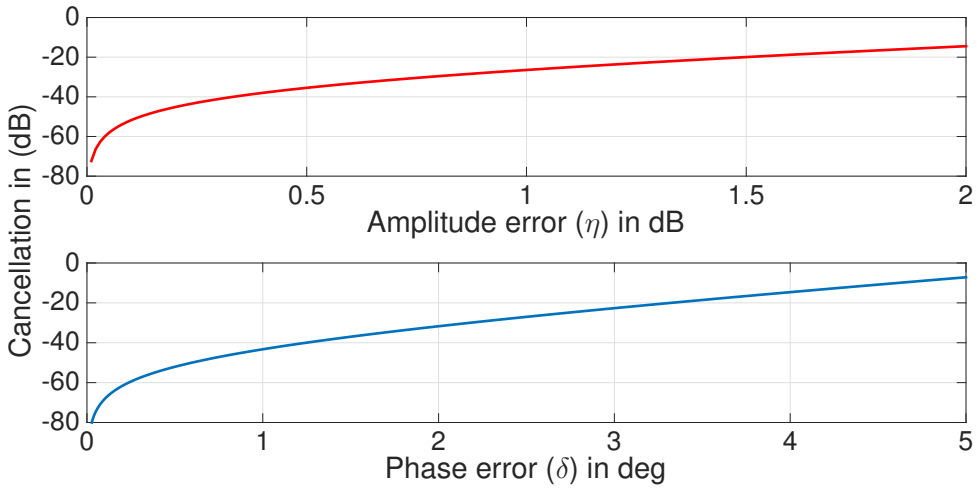

Figure 3.5: The effect of phase and amplitude errors on signal cancellation.

and phase matching.

For example, given two sinusoidal signals: S1= A$sin(\theta_1)$; and S2= B $sin(\theta_2)$, where the amplitude difference/error between A and B is η, and the phase difference/error between θ_1 and θ_2 is δ. The effect of these two errors in the cancellation performance can be seen in Fig. 3.5, which implies that the errors in the phase and amplitude must not exceed ± 3.5 degrees and ± 1.7 dB, respectively, for obtaining a 20 dB signal cancellation at minimum.

Furthermore, having a non zero bandwidth for the interferer signals identifies the need of highly linear phase characteristics over frequency, which can be considered as an additional requirement on the main path components. In fact, for many wide-band RF and microwave systems, linear phase response is equally desirable and a challenging design characteristic. Examples include, but are not limited to: adaptive antennas and radar systems (where phase characteristics are controlled for successful beam forming and target tracking [52]), wide-band multi-carrier power amplifiers (feed-forward amplifiers require precise delay to minimize distortion) and leakage cancellation systems to keep signals out of phase over a wide band of frequencies [53]. More parameters, such as as low insertion loss, small size, and low fabrication costs are also desirable in the design of

the phase shifters [54].

3.4.3 Bi-directional Coupler and RF Subtractor

Couplers are pure passive components with no active circuits included, and therefore the set of requirements are only targeting the amplitude losses and the isolation between the input ports. The coupler used is a bi-directional coupler whose scattering matrix must be symmetric. In the forward operation, the through port forms the main signal path of the feedforward loop. Thus, the maximum tolerable insertion loss must not exceed 1 dB. On the other hand, the auxiliary signal path is formed in the reverse operation of the coupler, after the coupled signal is reflected at the band-stop resonator. As a result, the coupler isolation becomes a very important parameter, as it determines the isolation between the main and the auxiliary signal paths, as well as the minimum cancellation that can be obtained for the interference signal. In this work, more than 25 dB isolation for the coupler is required to obtain a signal cancellation of higher than 20 dB. Furthermore, the couplers must operate over a sufficient bandwidth covering the frequencies of both the interferer, the desired received signal and the band separation between the two, which is typically less than 50 MHz. Either a Rat-Race-Ring coupler with a 3 dB coupling coefficient, or a 180 degree Wilkinson RF power combiner can be used to implement the RF subtractor.

3.5 System Tuning and Reconfigurability

As mentioned earlier, interference signals can appear with different power levels at several different frequency separations from the receiver band. The system requirements presented so far are able to handle different power levels for the interferer, because the signal to interference power ratio (SIR) is not a function of any of the system parameters. For example, the 20 dB coupling coefficient together with the 20 dB gain of the amplifier are not going to change, when handling interferers with SIR of 0 dB, 15 dB, or even higher

than 20 dB.

However, system tuning is still required to handle interference signals appearing at different frequency separations (2 MHz$\sim$ 20 MHz) from the receiver band, which itself can switch between different carrier frequencies (e.g. Public Safety LMR). Since the interferer and the wanted signal must always fall in the pass band and the stop band of the band stop resonator, respectively, therefore controlling the cutoff frequency of the resonator becomes essential, unless it is characterized by a wide pass/stop band. On the other hand, varying the cutoff frequency of the resonator changes the phase of the auxiliary signal path in the feedforward loop. Therefore, controlling the phase shifter in the main path is also needed to keep the phase matching between the two paths.

3.6 Practical Implementation of the Feedforward System

After reviewing commercial off-the-shelf modules available at “Mini-circuits” RF products, three modules are selected for matching some of the design requirements discussed above. These modules are the power amplifier (ZX60-3018G-S+), voltage controlled phase shifter (JSPHS-1000+), and bi-directional coupler (ZFBDC20-13HP-S+), as shown in Fig. 3.6.

3.6.1 ZX60-3018G-S+ Power Amplifier

According to the data sheet of the power amplifier module, it offers a very high performance perfectly matching the system design requirements. It operates over a very wideband starting at 20 MHz to 3 GHz, however, this work is considering the range between 500 MHz to 1000 MHz only. The power amplifier is characterized by low noise figure with a maximum level of 2.7 dB only. Fig. 3.7 shows the measured gain of the Mini-circuits amplifier varying from 22.42 dB at 500 MHz to 21.83 dB at 1000 MHz, which is only ± 0.59 dB. The maximum output power is 12.8 dBm with IP3 level of 25 dBm, which implies that

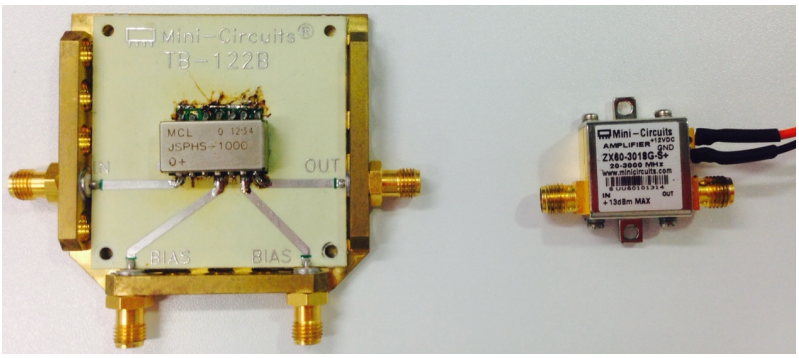

(a) (b)

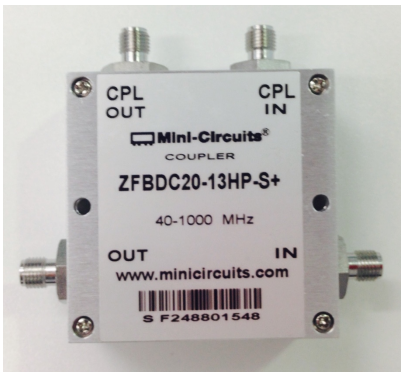

(c)

Figure 3.6: The three Mini-circuits RF components used in the system setup of the feed-forward interference cancellation. a- Voltage controlled phase shifter, b- Fixed gain power amplifier, c- Bi-directional coupler.

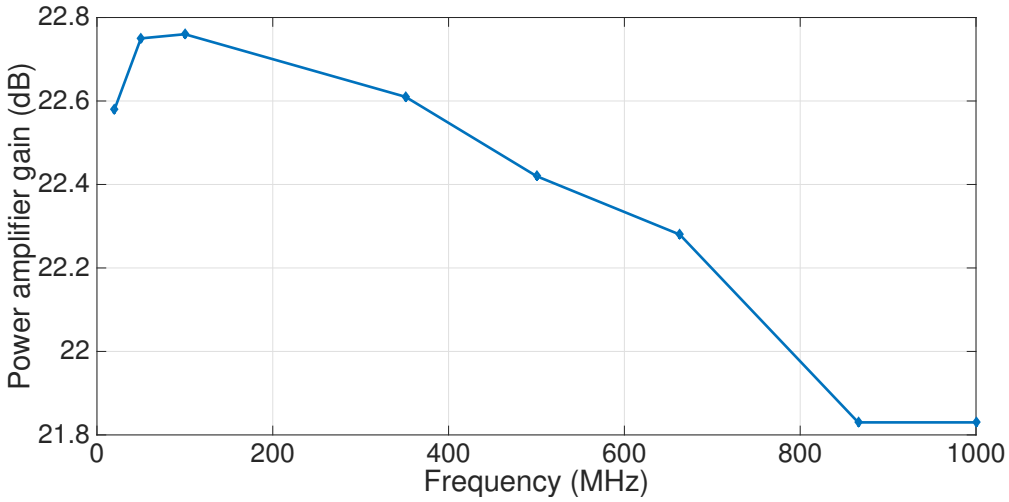

Figure 3.7: The measured gain of the Mini-circuits fixed gain power amplifier.

the third order intermodulation distortion products are non-significant.

3.6.2 JSPHS-1000+ Voltage Controlled Phase Shifter

The phase shifter operates over a wide-band starting at 700 MHz and up to 1GHz. It is characterized by low insertion loss of 1.5 dB and a voltage standing wave ratio (VSWR) of 1.3:1. Unlike the amplifier, the phase shifter shows a poor performance in terms of phase linearity, in addition to non-uniform phase steps with respect to the control voltages varying from 0 V to 15 V, as seen in Fig. 3.8.

3.6.3 ZFBDC20-13HP-S+ Bi-directional Coupler and Micro-strip Rat-Race-Ring

The Mini-circuits bi-directional coupler is selected for offering less than 0.4 dB insertion loss, as well as more than 26 dB isolation at 800 MHz over a wide frequency band reaching up to 1 GHz. Fig. 3.9 shows the measured S-parameters for the Mini-circuits coupler.

The Rat-Race-Ring coupler is designed and fabricated using Microstrip PCB technol-

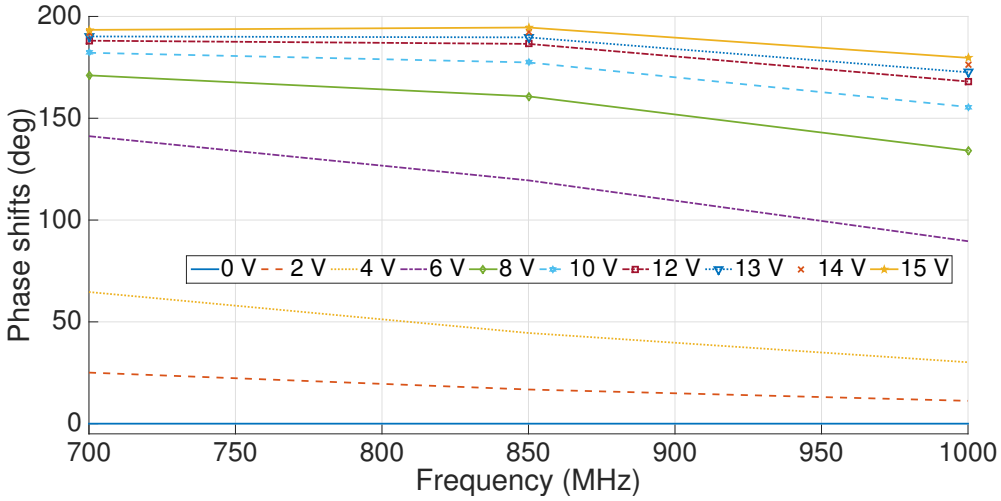

Figure 3.8: The measured phase shifts of the Mini-circuits voltage controlled phase shifter at different control voltages.

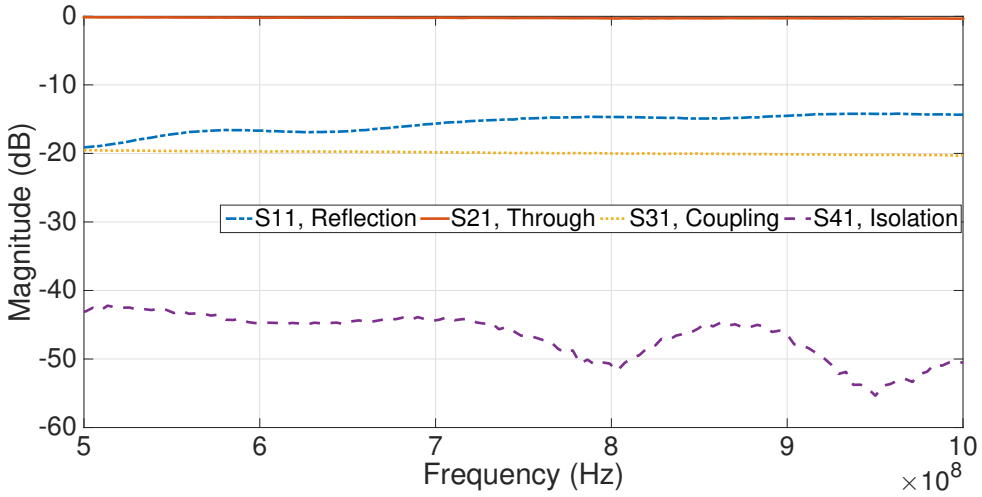

Figure 3.9: The 20 dB Mini-circuits bi-directional coupler used in the feedforward loop system setup.

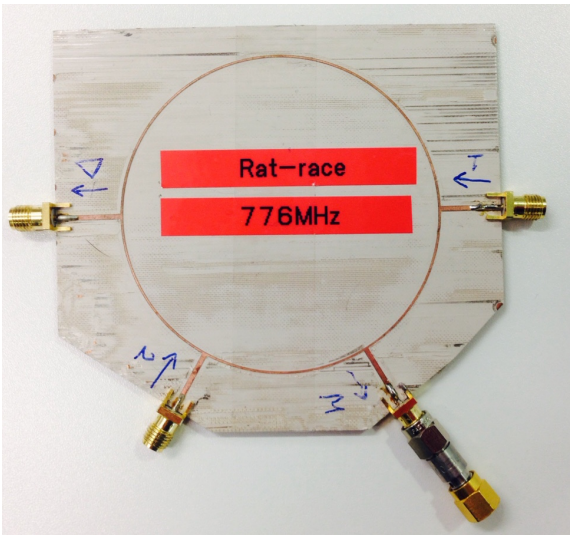

Figure 3.10: The Microstrip Rat-Race-Ring coupler used for subtracting the auxiliary path signal from the main path signal in the feedforward loop system setup.

ogy as shown in Fig. 3.10. It uses a high permittivity ceramic material with a dielectric constant of 10, so that it can confine the electromagnetic fields reducing the radiation losses at high power levels.

Mini-circuits off-the-shelf modules have a two-way power combiner with 180 degree phase shift between the two input ports, which functions similarly to the Rat-Race-Ring coupler. However, the isolation of the Rat-Race-Ring coupler is higher and the losses are much lower when compared to the power combiner. Fig. 3.11 shows the measured s-parameters for the coupler, which operates from 700 MHz up to 950 MHz with less than 0.6 dB insertion loss and more than 20 dB isolation.

3.6.4 Band-stop Resonator

As discussed before, there are several different interference cases in the 700 MHz band occurring between narrow band radios and broad band LTE signals, which are either generated from the public safety devices or the commercial mobile devices. In some cases, a high power narrow band interference signal is hitting a low power broadband LTE receiver.

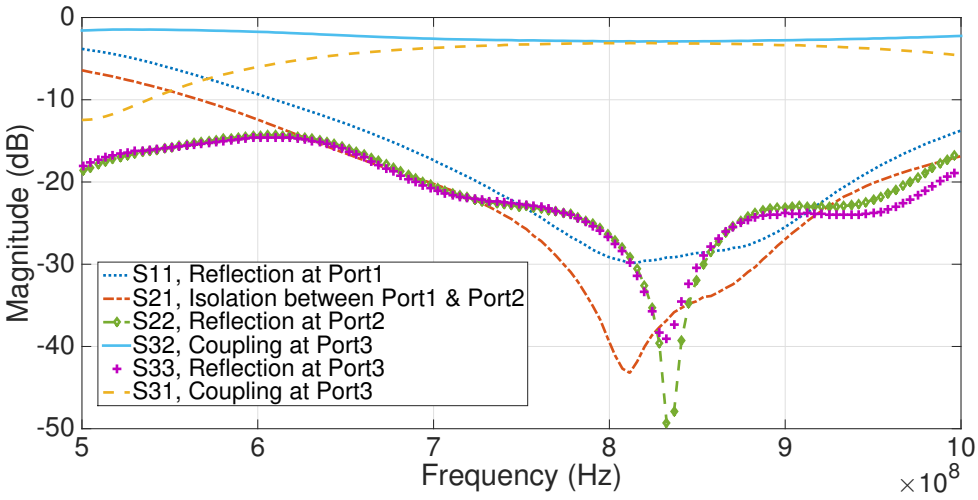

Figure 3.11: The measured S-parameters for the Rat-Race-Ring coupler in the feedforward loop system setup.

In others, a high power broadband is hitting a low power narrow band radio receiver. As a result, the band-stop resonator must be designed to separate two close Wideband signal (> 10 MHz) to match all the different interference scenarios. Implementing a low profile band-stop resonator for separating two Wideband signals with less than 20 MHz separation is still a research question. Hence, the following two chapters: Chapter V; and Chapter VI are focused on studying the design of this component.

3.7 Conclusion

Interference cancellation can now be fully implemented in RF domain without the need of any digital hardware using the new feedforward loop system presented in this chapter. The system employs the use of highly selective band-stop resonators to separate between the interference and the desired received signal. Both signals are known to be only few MHz away from each other making the design of these resonators be considered as a major challenge in setting up the new feedforward canceller system. And therefore, the following two chapters: Chapter IV; and Chapter V, are focused on studying

how to implement the band-stop resonator matching all the requirements discussed in this chapter.

High performance off-the shelf components from Mini-circuits are also used to setup a big part of the new feedforward canceller system, including: a fixed gain power amplifier; a bi-directional coupler; and a voltage controlled phase shifter. All these components are characterized and measured in this chapter using a Vector Network Analyzer (VNA). Measurements show that the phase shifter still suffers from poor phase linearity, which now introduces an additional challenge in the system realization encouraging the study of designing highly linear phase shifters, which will be discussed in detail in Chapter VI.

3.7.1 Contributions

This chapter has presented a new architecture for a feedforward interference cancellation system employing band-stop resonators. It has also explained and listed the specifications and requirements on the RF hardware used in this system, to enable handling large power interference signals located at small frequency offsets from the receiver.

Chapter 4

Multi-Tap Delay Resonators for Interference Filtering

4.1 Introduction

The feedforward interference cancellation system presented in the previous chapter still faces the challenge of generating an interference replica, which requires separating the interfering signal from the total received signal. The challenge appears when interference exists at only a few MHz away from the receiver edge, which is the case in some of the interference scenarios in the 700 MHz spectrum. According to the system requirements presented earlier, the process of separation requires a very high selective resonator with a fast switching between the pass and the stop band with a minimum roll-off rate of 1 dB per MHz, taking into consideration that each of the pass band and the stop band must cover a minimum bandwidth of 10 MHz. The additional size and cost constraints in small cell base stations suggest the use of microstrip planar circuits in developing the resonator used in the separation process.

In this chapter, the development of a new design for high selective band-stop resonators for separating close interference signals is presented. The idea of this design is

based on splitting the RF signal among multiple taps. Each tap is connected to a variable length transmission line with a short/open circuit termination. Having terminations with different lengths, a different time delay is encountered by the signal in each tap, and therefore this band-stop resonator is named as a “Multi-Tap Delay Resonator”. In this design, three parameters are controlling the frequency response of the band-stop resonator, which are the number of signal taps, the power split ratio among the taps, and the time delay step between the taps. In order to understand the effect on each of these parameters on the frequency response, a detailed study is performed in the first three sections of this chapter.

- Section 4.2 starts by carrying out a general analysis on the structure of a two-tap notch circuit being the basic building block of the new Multi-Tap Delay resonator. Followed by a discussion on the effect of varying the number of signal taps in the frequency response of the resonator.

- Section 4.3 presents two different prototypes for a four-tap band-stop resonator using uniform and non uniform amplitude distribution among the signal taps. An analysis is performed on the frequency response of the resonator with uniform amplitude distribution based on circuit model simulations using components from System Passive Library in ADS. Furthermore, a mathematical formula for the transfer function is derived. On the other hand, a new optimization technique is introduced for resonators with non-uniform amplitude distribution to obtain the ideal power split ratio required for maximizing the stop-band rejection.

- Section 4.5 discusses the pros and cons of using a non-uniform time delay step when designing Multi-Tap Delay resonators.

- Section 4.6 presents the microstrip implementation of four-tap resonators with uniform time delay step and non-uniform amplitude distribution, which is selected for achieving better stop-band rejection characteristics.

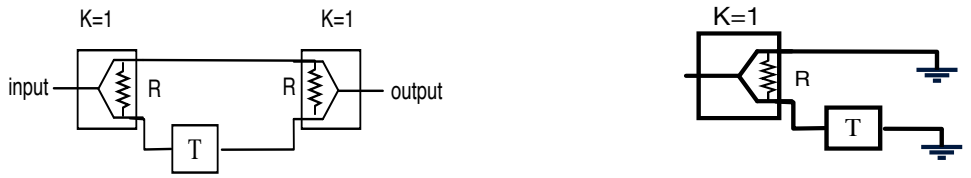

(a) 2-tap notch filter (b) 2-tap notch resonator

Figure 4.1: The circuit model of a simple 2-tap notch filter in a resonator in b with T= 9 ns. K is the power split ratio between the two ports of the Wilkinson power divider.

- Section 4.7 demonstrates an experiment for testing the performance of the feed-forward RF cancellation of interference signals using the newly fabricated four-tap band-stop resonator.

- Finally, in Section 4.8, the test results are analyzed, and evaluated by means of a comparison held between three different interference cancellation techniques, which are previously discussed in Chapter II. The three techniques are the feed-forward interference cancellation at intermediate frequency (IF) [28]; the hybrid RF-DSP interference cancellation [50]; and the N-path notch digital filtering [32].

4.2 The Structure of the Multi-Tap Delay Resonator

The block diagram of a conventional two-tap notch filter is shown in Fig. 4.1-a. It consists of a power splitter/combiner dividing the RF signal among two paths (referred to as taps), where one is holding a time delay element (T). The time delay can be defined as the ratio between the angular frequency and thephase of the reflected signal at a particular frequency, while the group delay is the rate of change of phase with respect to angular frequency. A two-tap notch resonator can be constructed by terminating the two taps with either a short or an open circuit instead as shown in Fig. 4.1-b. The signals are now reflected at the circuit termination and recombined back at the input of the power splitter. Ideally, the signal is perfectly reconstructed with zero insertion loss as long as the

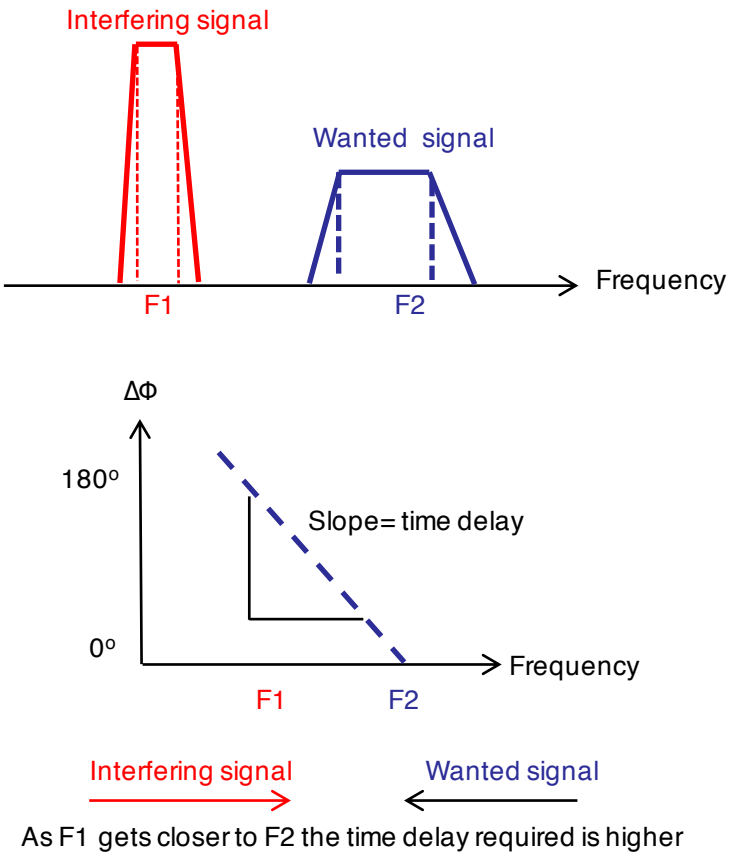

Figure 4.2: A diagram showing the relation between the time delay in a 2-tap notch resonator, and the frequency separation between the interferer and the receiver edge.

reflected signals from the two taps are in phase. As the phase difference increases, the insertion loss increases reaching infinity and a notch is created. A single notch appears in the frequency response of the reflection coefficient at frequencies $f_{notch} = \frac{n}{2T}$, where n is an odd number. At f_{notch}, the incident wave is reflected at the short circuit terminations of the two taps and destructively recombined, where the power of the signal is absorbed by the resistance of the power divider. In this case, the band-stop resonator doesn't represent any significant resistive losses to the receiver signal.

Separation of an interference signal from the receiver requires placing a notch at the

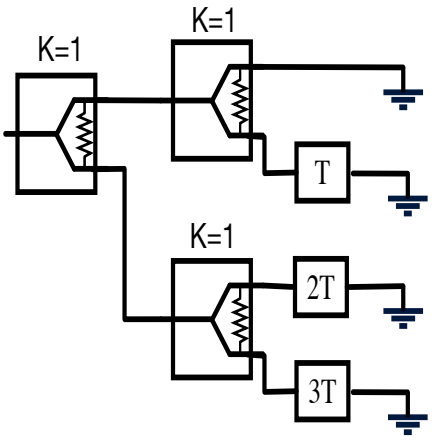

Figure 4.3: The circuit model of the 4-tap stop band resonator with ideal delay elements, T= 3 ns.

carrier frequency of either the interference or the wanted signal while leaving a maximum on the other. For example, given an interfering signal at F1 is affecting an RF receiver operating at a carrier frequency F2, a two-tap notch resonator can be used to place a notch at F1 while leaving a maximum at F2. In this case, the phase difference between the two taps is 180^o and 0^o at F1 and F2, respectively. The difference in the group delay between the two taps now becomes a function of the frequency separation between the two signals (ΔF= F2-F1). As the frequency separation between the two signals decreases, larger delays will be required as illustrated in Fig. 4.2.

Interferers are modulated signals with non-zero bandwidth and therefore multiple notch points are required for filtering out the signal rather than a single notch. The notch points in the frequency response must be selected such that they are close enough to form a stop band with low amplitude ripples. Increasing the number of taps creates more combinations where the divided portions of the signal are reflected out of phase and multiple notch points can be formed. The idea of constructing this resonator can be considered similar to tapped delay filters. There are two types of tapped delay filters:

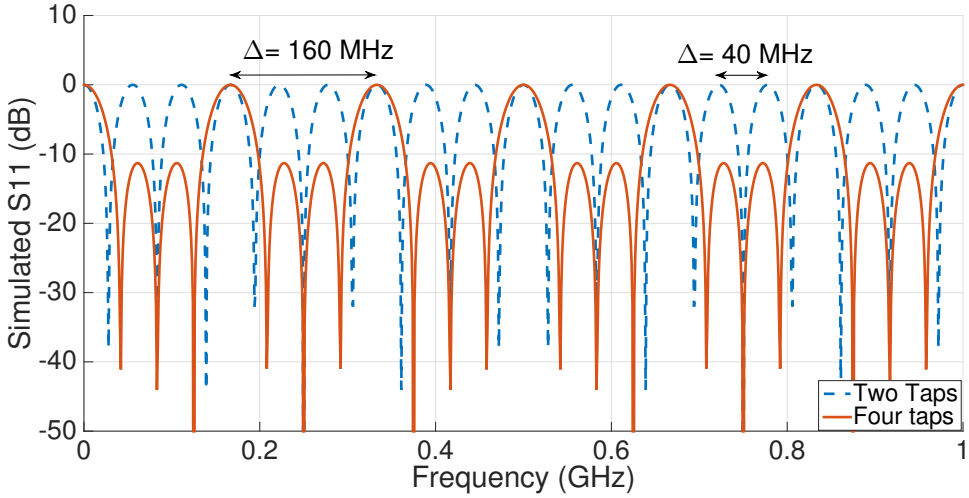

Figure 4.4: The simulated S-parameter for a two-tap and a four-tap resonator.

transversal digital filters which are also known as Finite impulse Response (FIR) filters; and transversal analog filters. Digital FIR filters are formed of a weighted summation of N+1 taps, each tap holds a sample of the digital signal delayed by one unit (-1) [55]. Unlike FIR, transversal analog filters use continuous time input signals, thus active integrating transistor circuits are used [56]. Fig. 4.3 show the structure of a four-tap delay resonator constructed using ideal components from System-Passive Library in Agilent ADS 2015. This resonator can be seen as the first attempt to design and implement tapped delay filters at high frequency.

The effect of increasing the number of taps can be demonstrated by carrying circuit simulations for the constructed two-tap delay resonator in Fig. 4.1-b and the four-tap delay resonator in Fig. 4.3. The delay component in the second tap of the first resonator is set to a value of 9 ns. While, the three delay components in the second, third and fourth taps of the second resonator are set to a value of 3 ns (T), 6 ns and 9 ns, respectively. Fixing the time delay differences between every two successive taps equates the frequency separation between the notch points. This can be seen in the circuit simulation results shown in Fig. 4.4, which also points to a doubling of the rejection bandwidth with three

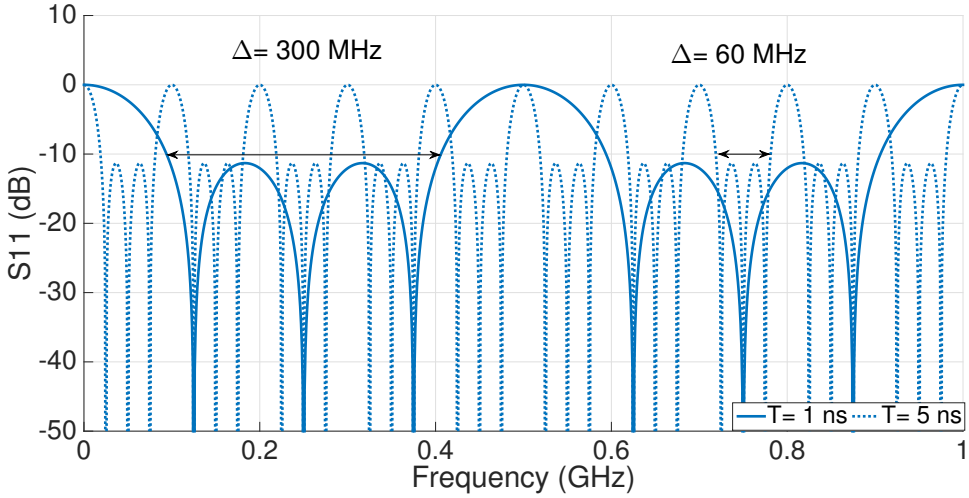

Figure 4.5: The simulated S-parameter for a four-tap band-stop resonator designed using step delays (T).

notch points for the four-tap delay resonator. The simulations of the four-tap resonator are again repeated using different step delays: T= 1 ns; and T= 5 ns, as shown in Fig .4.5. The results show an increase in the rejection roll-off rate from 0.1 dB per MHz to 0.5 dB per MHz after increasing the step delay from 1 ns to 5 ns. These results verify the direct relation between the time delay step and the rejection roll-off rate (dB/ MHz) of the band-stop resonator. This relationship is going to be used in Section 4.6 when discussing the implementation of the resonator required for the feedforward interference cancellation system.

4.2.1 Transfer Function Derivation for Multi-Tap Delay Resonators

In order to understand how the notch points are formed and how to control their location in the frequency domain, a mathematical analysis is performed for the transfer function. The transfer function of the Multi-Tap Delay resonator $H(\omega)$, defined as the ratio between the reflected and input signals, can be derived by referring to the mathematical derivation of an antenna array factor. According to antenna theory, the array factor combines the

effects of distributing the input power on multiple antenna elements on the overall radiation pattern, given a fixed step of phase shifts in the current feeding each two neighboring antenna elements [57]. Similarly, the transfer function of the resonator here is aimed to combine the effects of distributing the input power on a certain number of taps (N) with a fixed delay step between each two successive taps.

Given that the total input signal for an N-Tap Delay resonator with uniform amplitude and delay step is $A\,e^{jwt}$, therefore the total reflected signal back at the input $R(\omega)$ can be expressed as follows:

$$R(\omega) = [1 + e^{j\omega T} + e^{2j\omega T} + ...e^{(N-1)j\omega T}]\,ae^{j\omega t} \tag{4.1}$$

$$R(\omega) = (\frac{e^{j\omega T} - 1}{e^{j\omega T} - 1})\,[1 + e^{j\omega T} + e^{2j\omega T} + ...e^{(N-1)j\omega T}]\,ae^{j\omega t} \tag{4.2}$$

$$R(\omega) = ae^{j\omega t}\,\frac{(e^{jN\omega T} - 1)}{(e^{j\omega T} - 1)} \tag{4.3}$$

where ω is the angular frequency, $a = \frac{A}{N}$ and T is the time delay step between every two successive taps.

$$H(\omega) = \frac{1}{N}\,\frac{(e^{jN\omega T} - 1)}{(e^{j\omega T} - 1)} = \frac{1}{N}\,\frac{sin(\frac{N\omega T}{2})}{sin(\frac{\omega T}{2})} \tag{4.4}$$

Now, $H(\omega)$ forms a periodic sinc function whose period is equal to $\frac{1}{T}$. The number of stop band ripples located between every two successive peaks is always equal to $N-2$, while the number of notch points is $N-1$. By plotting the transfer function for different values of N, it can be noticed that the 3 dB bandwidth is reduced with the increase of N, thus higher roll-off rate is obtained for the resonator, as shown in Fig. 4.6.

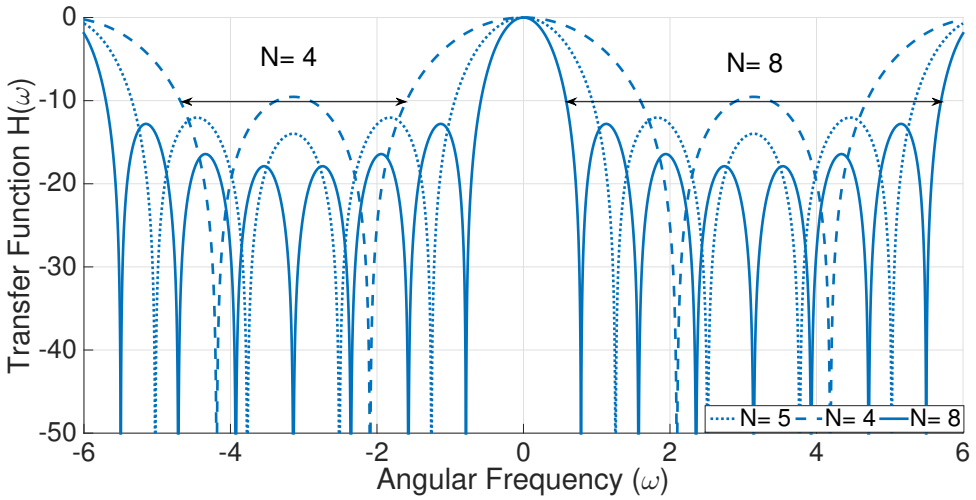

Figure 4.6: A plot for the transfer function $H(\omega)$ of Multi-Tap resonators with different number of taps (N).

4.3 The Effects of Unequal Tap Amplitudes on the Frequency Response

Multi-Tap Delay resonators can be classified based on the power split ratio (K) at the input into uniform and non-uniform amplitude resonators. For uniform amplitude resonators, K is equal to 1, and the power is distributed equally among all the signal taps of the resonator. One can assume that the power of each tap arrives equally at the short circuit termination and back to the power combiner. This assumption can be made true given that only ideal circuit components are used, which is never the case as all non-ideal effects must be involved. In fact, the power combiner will always receive unequal amplitude levels from each of the delay taps. The reason is the insertion loss of RF transmission delay lines increases with the increase of the group delay obtained by the line. However, peaks and notches can still be formed as long as the insertion loss is directly proportional to the time delay in each tap.

The effects of unequal tap amplitudes can be demonstrated by modifying the circuit

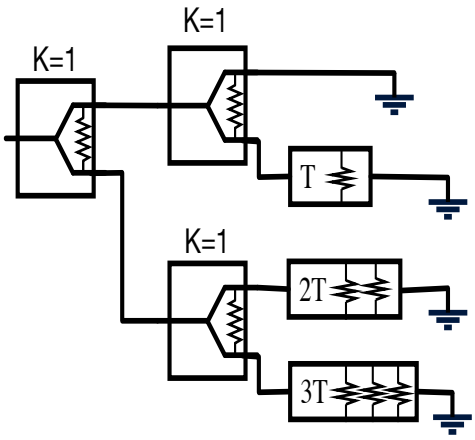

Figure 4.7: The circuit model of the 4-tap stop band resonator with lossy delay components, T= 3 ns.

block diagram introducing attenuators in each tap as shown in Fig. 4.7. The attenuation values are inserted assuming 1 dB loss for every 3 ns, which is a rough estimation for the insertion losses of large delay transmission lines. The simulation results in Fig. 4.8 shows how the lossy delays have affected the overall frequency response. The pass band is shifted down showing more than 3 dB insertion loss. Notch points are formed, but the rejection is reduced by more than 12 dB. On the other hand, the peaks of the stop band ripples are reduced by more than 9 dB, which can be seen as the only advantage of the losses. This single advantage has brought an interest in investigating the structure of non-uniform amplitude resonators, where the unequal tap amplitudes are not only a result of delay losses, but also a power split ratio of K$\neq$1 is imposed.

4.4 Non-uniform Amplitude Multi-Tap Delay Resonators

A study is carried on the effect of the amplitude variations between the resonator taps on the frequency response, where lowering the amplitude of the signals reflected back from

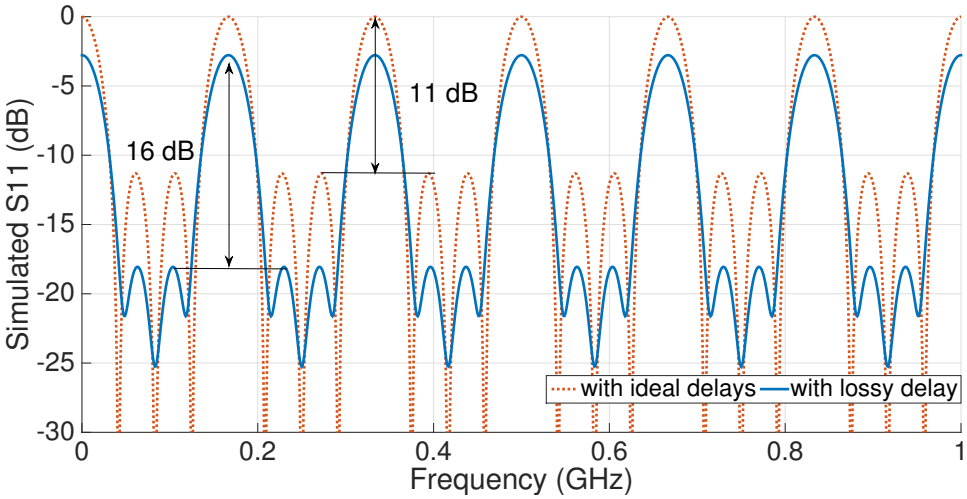

Figure 4.8: The simulated circuit model of a four-tap stop band resonator with lossy delay components, T= 3 ns

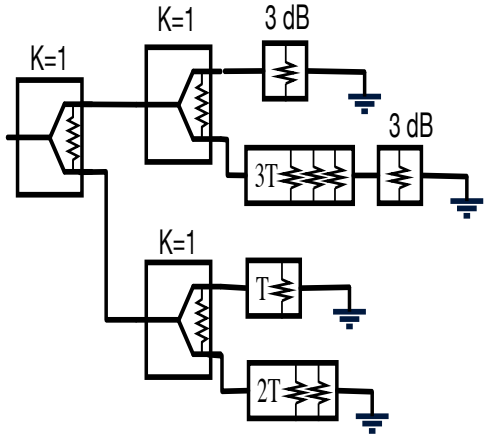

Figure 4.9: The circuit model of the new 4-tap stop band resonator with added attenuators, T= 3 ns.

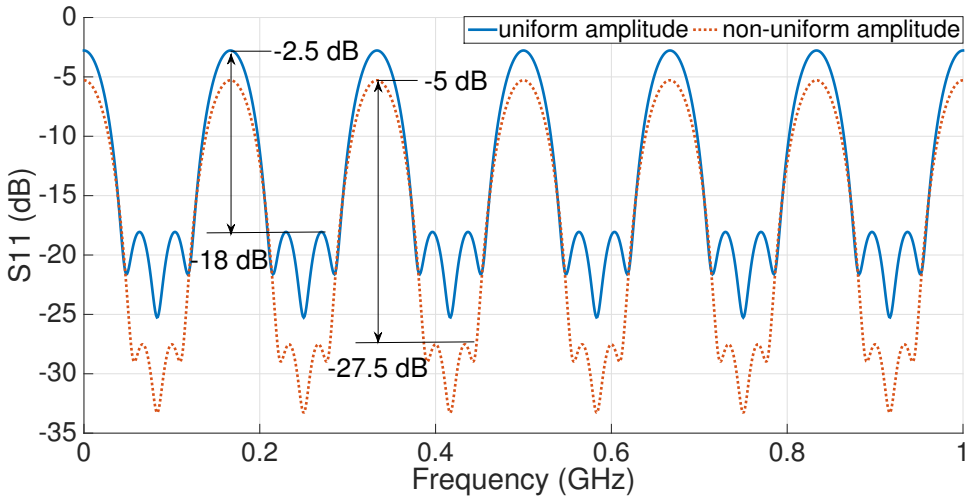

Figure 4.10: A comparison between the simulated circuit model of four-tap resonators with uniform and non uniform amplitudes.

the taps with both the smallest and largest delays has been found to improve the rejection characteristics. This can be demonstrated by inserting additional attenuators (e.g. 3 dB) to the first and fourth signal taps as shown in Fig. 4.9. The circuit simulations for the 4-tap model with, and without, the attenuators are now compared in Fig. 4.10, where more than 14 dB extra attenuation is achieved in the stop-band leaving the passband with additional losses of 2.5 dB.

To keep some of the improvements but avoid the additional losses, it is suggested to eliminate the 3 dB attenuators and adjust the power split ratio of the first power divider at the input port instead as shown in Fig. 4.11. The power split ratio (K) is the ratio between the power at the first output, to that in the second output in a four-tap resonator. Therefore, K= 0.5 suggests distributing one third of the signal among the two taps with the largest and smallest time delays leaving the remaining power equally distributed among the inner taps.

This can be explained by re-writing the transfer function of the four-tap resonator with unequal amplitude coefficients, as seen in Eqn. 4.5, then replacing every $e^{j\omega T}$ by x to

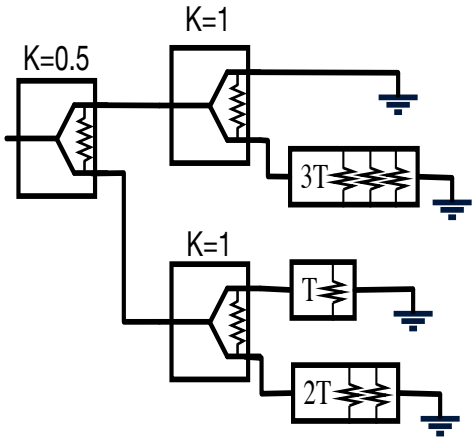

Figure 4.11: The circuit model of the new 4-tap stop band resonator with unequal power split ratio K= 0.5 , T= 3 ns.

obtain Eqn. 4.6. In this case, the amplitude losses of the delay taps are not considered, because they don't present a significant effect on the frequency response.

$$H(\omega) = e^{j\omega t}[A_o + A_1 e^{j\omega T} + A_2 e^{j2\omega T} + A_3 e^{j3\omega T}] \tag{4.5}$$

$$H(\omega) = e^{j\omega t}[A_o + A_1 x + A_2 x^2 + A_3 x^3] \tag{4.6}$$

Improving the rejection of the resonator means reducing the level of the stop band ripples, and these ripples can be totally eliminated by equating the amplitude coefficients of the transfer function $H(\omega)$ to the coefficients of the binomial expansion of $(x+1)^3$ determined using Pascal's triangle in Fig. 4.12. In this case the amplitude distribution among the four taps becomes 1: 3: 3: 1. It is not advised to use these exact coefficients as it will combine the three notch points into one thus reducing the rejection bandwidth. However, it is recommended to follow the nature of Pascal's distribution, such that the outer taps carrying the smallest and largest delays are fed by equal fractions of power.

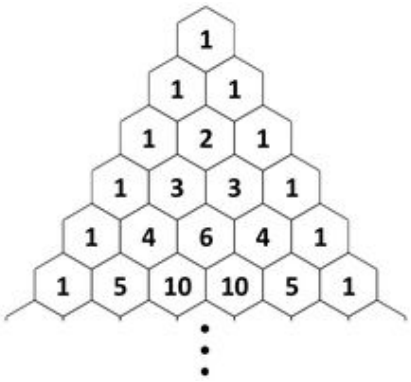

Figure 4.12: Pascal's triangle listing the coefficients of high order binomial expansions [58].

The same applies for the inner taps, thus the optimum power split ratio (K) of the second and third power dividers is 1. On the other hand, the power split ratio (K) of the first power divider must be set to a value less than one for reducing the level of the stop band ripples.

Fig. 4.13 shows the circuit simulation results of the modified resonator with different values for K for the first power divider. For K=1, the structure can be classified under uniform amplitude resonators whose insertion loss is equal to 3 dB, first notch point rejection equals to -18 dB, and stop band ripples level of -14 dB. For K= 0.7, the insertion loss remains the same, the rejection of the first notch is increased by more than 3 dB and the side lobe level is reduced by more than 5 dB. As K reduces to 0.6, the rejection of the notch is further reduced by another 2 dB, while the stop band ripples are reduced to reach -21 dB. This leaves a gap of more than 18 dB between the peak of the pass band and the peak of the stop band. This gap has previously been equal to 10 dB for uniform amplitude resonators (K=1), and now the K= 0.6 structure has the gap increased by 8 dB, while keeping the exact same insertion loss in the pass band. This recommends the use of non-uniform amplitude resonators with un-equal power split ratio among the taps for having a significant improvement in the stop band rejection over a wider frequency bandwidth.

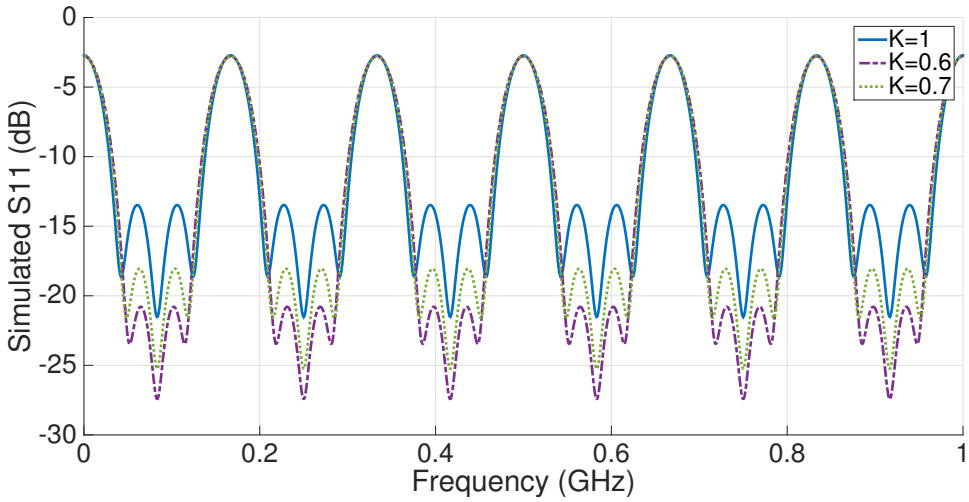

Figure 4.13: The simulated S-parameter for 4-tap band-stop resonators with different power split ratio K.

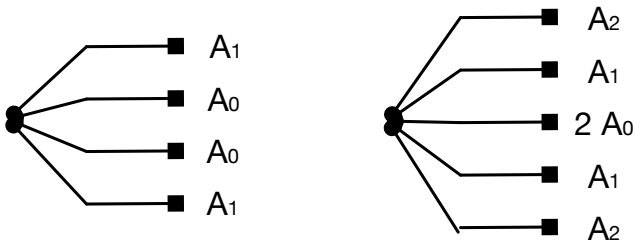

(a) Four taps (b) Five taps

Figure 4.14: Chebyshev amplitude distribution for even and odd number of taps (N).

4.4.1 Chebyshev Power Split Ratio Optimization

In this subsection, a methodology is suggested to optimize the power split ratio between the resonator taps for a specific required stop band attenuation. This methodology is based on the Chebyshev optimization used to obtain the amplitude ratio of the currents feeding an array of antenna elements for minimizing the side lobe level of the radiation pattern [59].

Assuming that the power distribution among N taps is symmetric across the $\frac{N}{2}th$ tap

for even N, or the $\frac{N+1}{2}^{th}$ tap for odd N. The reason behind this assumption is to simplify the transfer function $H(\omega)$ for N taps with un equal amplitudes, which can expressed as follows:

For even N, Fig. 4.14-a.

$$H(\omega) = A_o e^{\frac{\omega T}{2}} + A_o e^{\frac{-\omega T}{2}} + A_1 e^{\frac{3\omega T}{2}} + A_1 e^{\frac{-3\omega T}{2}} + A_2 e^{\frac{5\omega T}{2}} + A_2 e^{\frac{-5\omega T}{2}} + ...A_{\frac{N}{2}} e^{\frac{(N-1)\omega T}{2}} \tag{4.7}$$

$$H(\omega) = 2A_0 cos(\omega T) + 2A_1 cos(3\omega T) + 2A_2 cos(5\omega T) \tag{4.8}$$

$$H(\omega) = \sum_{n=0}^{n=(N/2)-1} A_n cos(\frac{2n+1}{2}\omega T) \tag{4.9}$$

For odd N, Fig. 4.14-b.

$$H(w) = \sum_{n=0}^{n=(N-1)/2} A_n cos(n\omega T) \tag{4.10}$$

Given that the attenuation level required is R, which is defined as the ratio between the peak of the stop band ripples to the pass band peak level. Then $A_o, A_{1,} A_2, ...A_{\frac{N}{2}}$ can be calculated by comparing the coefficients of $H(\omega)$ to the Chebyshev polynomial of the same order $T_m(\frac{x}{x_o})$, where x_o is equal to $T_m^{-1}(R)$.

4.4.1.1 Example

For a four-tapped delay resonator. The optimum amplitude ratio required for a minimum stop band attenuation of 20 dB can be obtained by applying the following steps:

- Step 1: Write down the transfer function $H(\omega)$

- $H(\omega) = A_o cos(\omega T) + A_1 cos(3\omega T)$

- Step 2: Expand the cosine with all the multiples of ωT to its equivalent series polynomial

  - $H(w) = A_o cos(\omega T) + A_1(cos^3(\omega T) - 3sin^2(\omega T)cos(\omega T)) = A_o cos(\omega T) + A_1 cos^3(\omega T) - 3A_1(cos(\omega T) - cos^3(\omega T))$

- Step 3: Replace every $cos(\omega T)$ with x , then select the Chebyshev polynomial $T_m(x)$ with the same order m= 3.

- Step 4: Determine the point x_o on $T_m(x)$ such that it satisfies the condition $T_3(x)_{x=x_o} = cosh[\frac{1}{3}cosh^{-1}(10^{20/20})]$, $x_o = 1.54$

- Step 5: Write the normalized transfer function $h(\frac{x}{x_o}) = 4A_1(\frac{x}{1.54})^3 + (A_o - 3A_1)(\frac{x}{1.54})$

- Step 6: By comparing the coefficients of the Chebyshev polynomial to the transfer function, A_o and A_1 will be equal to 6.33 and 3.65, respectively.

These results now correspond to an optimum power split ratio of K= 0.56. This ratio is less than the ratio proposed by Pascal's distribution above (K= 0.33), as the amplitude of the stop band ripples is now optimized rather than being totally eliminated.

4.4.2 Tuning Capabilities of Multi-Tap Delay Resonators

As the interference signals are not stationary, the capability of tuning the frequency response of the resonator is essential. In the proposed system, the resonators can be tuned by introducing slight adjustments in the delay step between the taps, which can be done using variable phase shifters. Fig. 4.15 shows the circuit structure of a four-tap Delay resonator with tuning phase shifters. It can be noticed that the three phase shifters are adjusted separately, so that the additional phase shifts become proportional to the time delay of each tap. For an example, if the phase of the second tap is selected to

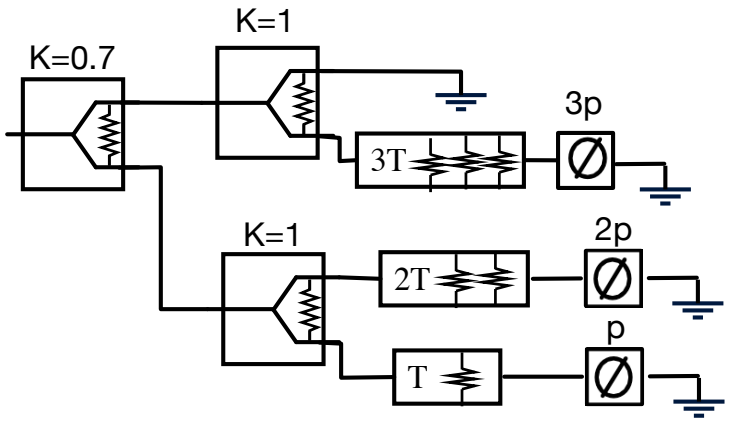

Figure 4.15: The modified circuit model for a tunable four-tap band stop resonator, T= 3 ns, K= 0.7.

be equal to 15^o, then the phase shifters in the third and the fourth tap must be adjusted at p= 15^o and p= 30^o, respectively. The simulation results of the circuit structure of the resonator in Fig. 4.16 now indicate a 15 MHz shift in the center frequency of the pass band for every added 15 degree. Also, it can be said that the precision of tuning these resonators only depends on the accuracy of the variable phase shifter to be used.

4.5 Multi-Tap Delay Band-stop Resonator with Non-uniform Delay Step

It is mentioned above that the delay step between the resonator taps must be fixed, similarly the phase step when tuning the resonator must also be fixed. This section now investigates varying the delay step between each two consecutive taps creating a non-uniform delay step type of resonator. The reason for carrying out this investigation is to allow some freedom in optimizing the width of the stop band of these resonators to cover not more than 10 MHz bandwidth. An interesting fact about this type of resonators is that it is possible to determine the least number of taps with the least delay values needed

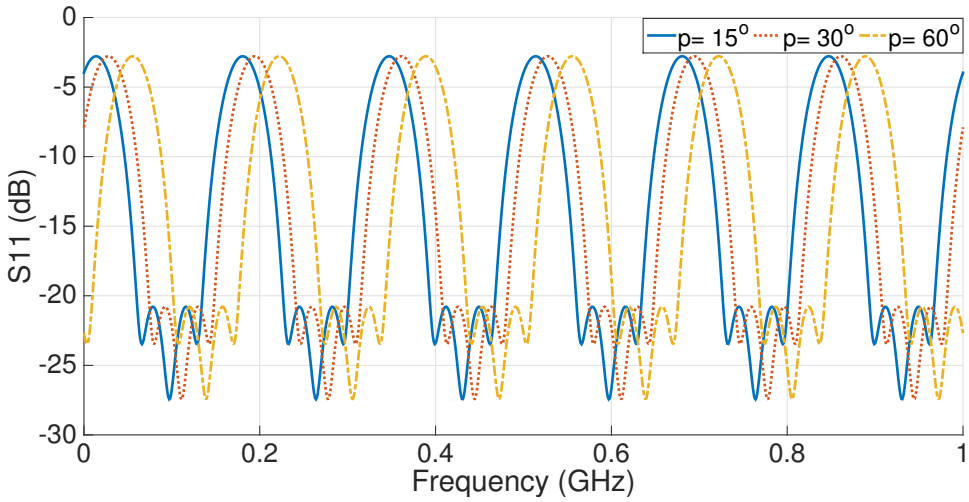

Figure 4.16: The simulation results for the model in Fig. 4.15 with different phase states.

to meet the given frequency response specifications. In other words, resonators with non-uniform delay step can become more efficient in terms of size and complexity.

Unfortunately, there is no formal methodology for designing band-stop resonators with non-uniform delay step. However, it is possible to construct a search algorithm, with a given range for each of the constructing parameters of the resonator: number of taps; delay in each tap; and the amplitude of each tap. The search algorithm is run to try all the different combinations. Each resulting function is evaluated based on meeting the specified rejection requirements, as shown in the example below.

4.5.1 Example

A search algorithm is built using Matlab to determine the constructing parameters for rejecting a 5 MHz signal located at 20 MHz away from the wanted signal centered at 780 MHz, given that more than 15 dB stop band attenuation is required. Table. 4.1 lists a summary for the results satisfying the search conditions. The frequency response of the three resonators constructed using the parameters in Table. 4.1 is plotted in Fig. 4.17. It can be seen that reducing the number of taps from 4 to 3 taps does not alter the

No. of taps	Delay in each tap (ns)	IL (dB)	Attenuation (dB)
2	T1= 16.61	< 0.7	18.2
3	T1= 21.7, T2= 10.18	< 1	> 20
4	T1= 24.3, T2= 17.93, T3=10.34	< 1	> 20

Table 4.1: Multi-Tap delay resonator with uniform amplitude and non uniform delay step

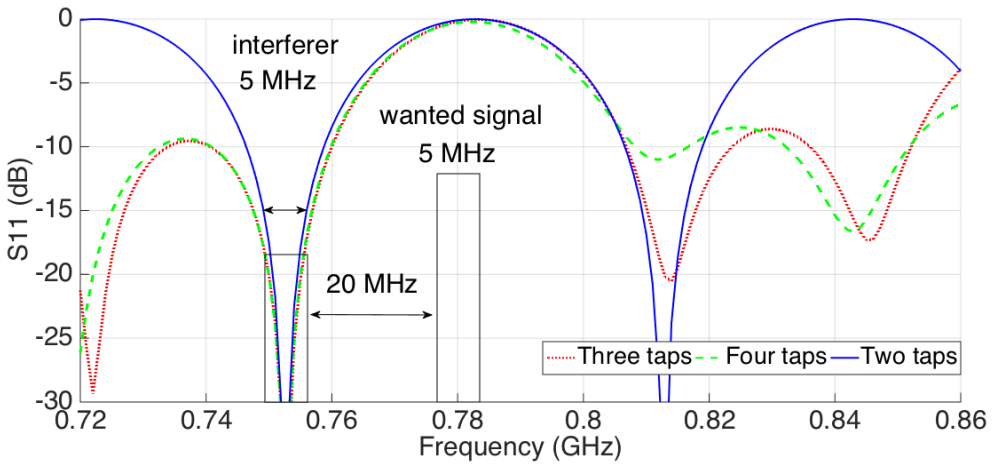

Figure 4.17: The transfer function of Multi-Tap band-stop resonator with non-uniform delay step whose design details are given in Table. 4.1.

attenuation, given that the signal to be rejected appears on the left side of the wanted signal.

Although, this approach offers advantages in terms of reducing the number of taps or in other words the physical size, this type of resonators is abandoned in the work presented in this thesis due to the high sensitivity of some of the parameters. In fact, the effects of any slight variation in either the amplitude or the group delays is unpredictable. On the other hand, it is not guaranteed to eliminate these small variations in the design parameters in practice due to fabrication tolerances.

4.6 Microstrip Implementation and Measurements

This section presents the implementation of the Multi-Tap Delay resonator employed in the feedforward interference cancellation system. The resonator must be able to separate two modulated signals whose maximum operating bandwidth can reach up to 10 MHz, and with a frequency separation ranging from 20 and down to 10 MHz only. The maximum required delay (T_{max}) is first calculated such that it satisfies the two conditions described in Eqn. 4.11 and 4.12, given that N= 2.

$$H_{normalized}(\omega_1) = \frac{1}{N}\frac{sin(\frac{N\omega T_{max}}{2})}{sin(\frac{\omega T_{max}}{2})} = 1 \tag{4.11}$$

$$H_{normalized}(\omega_2) = \frac{1}{N}\frac{sin(\frac{N\omega T_{max}}{2})}{sin(\frac{\omega T_{max}}{2})} = 0,\ first\ null \tag{4.12}$$

where ω_1 and ω_2 are the centre frequencies of the wanted received signal (770 MHz) and the interferer, respectively.

For circuit implementation, size is the one of the most important complexity measures. A four-tap resonator is therefore selected to minimize the size of the structure with three delays: τ= $\frac{T_{max}}{3} = 7.3$ ns; $\frac{2T_{max}}{3} = 14.6$ ns; and $T_{max} = 21.9$ ns. The circuit is implemented in microstrip technology for the ease of fabrication. Ceramic substrate (Rogers 6010) is selected with high permittivity ($\varepsilon_r = 10.2$, thickness= 1.27 mm) to obtain the large delays required with minimum circuit dimensions.

The optimum power split ratio (K) is calculated using the technique in Section 4.4 to be 0.56. Constructing Wilkinson power dividers with the calculated power split ratio requires very high impedance sections, whose physical dimensions falls below 0.2 mm. Since, the circuits here are fabricated using the standard milling tools available in the lab, it is advised to increase the power split ratio for the first power splitter up to 0.7 to ease the implementation issues. On the other hand, the second and the third power splitters

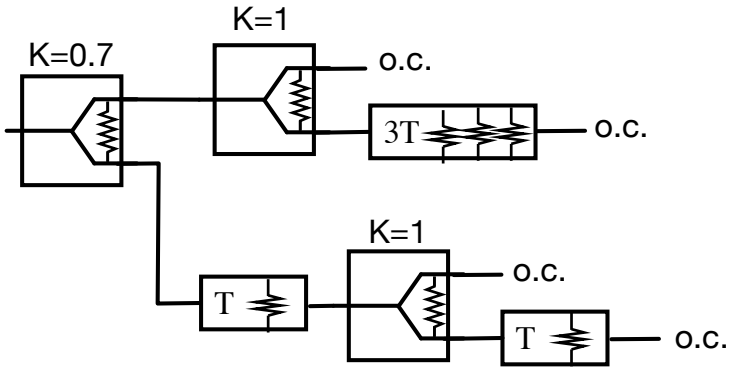

Figure 4.18: Four-tap resonator circuit model with reduced size.

are designed with equal power split ratio, K=1.

The RF delay components are constructed using 50 Ω meander transmission lines, whose height is designed to be less than quarter the propagation wavelength ($\lambda_g = 28$ mm), in order to avoid resonances and suppress higher order modes. The meander lines are also separated by a 2 mm gap to reduce coupling losses. Eqn. 4.13 is used to calculate the transmission line lengths (L) for the delays (τ) in each of the three taps.

$$L = \frac{\tau\sqrt{\varepsilon_r}}{c} \tag{4.13}$$

Each signal tap is terminated with an open circuited stub with the following dimensions:

- 15 mm for the first tap.
- 30 mm for the second tap.
- 20 mm for the third tap.
- 25 mm for the fourth tap.

These dimensions are chosen to maintain the fixed group delay between each two con-

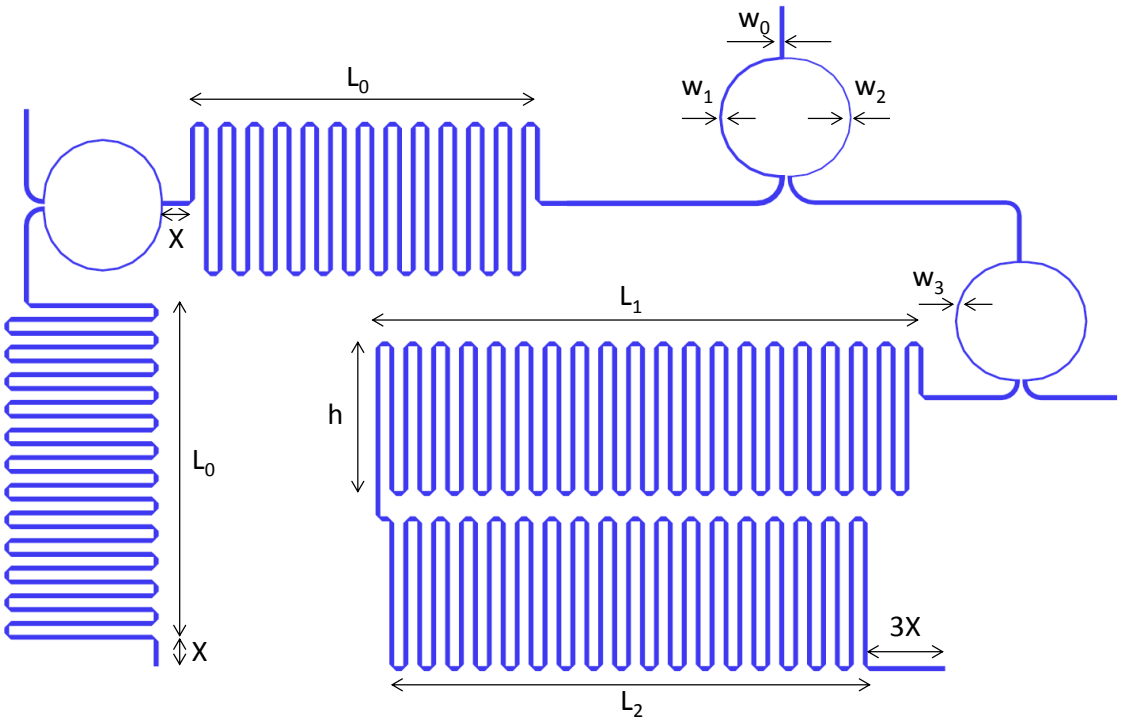

Figure 4.19: The board layout of the 4-tap band stop resonator with K= 0.7. The outline of the board is 13.5 cm x 22.5 cm.

secutive taps. Short circuit terminations are avoided to facilitate the fabrication process and avoid the losses introduced by grounded vias. For further size reduction, a 20 mm delay lines is shared between the third and fourth taps, as shown in Fig. 4.18.

Fig. 4.19 shows the top layer of the board layout which is built using the Passive Microstrip Circuits Library in ADS. Table.4.2 lists all the geometric dimensions for the four-tap band-stop resonator board.

Table 4.2: Geometric dimensions of the board in mm

w_0	1.367	w_2	0.281	L_0	69.3	L_2	97.8	h	30.5
w_1	0.772	w_3	0.497	L_1	108.5	s	1.75	X	5.0

Fig. 4.20 shows the fabricated microstrip four-tap Delay resonator with K= 0.7, whose circuit dimensions are 13.5 cm x 22.5 cm. Another board is fabricated with K=1 and Fig.

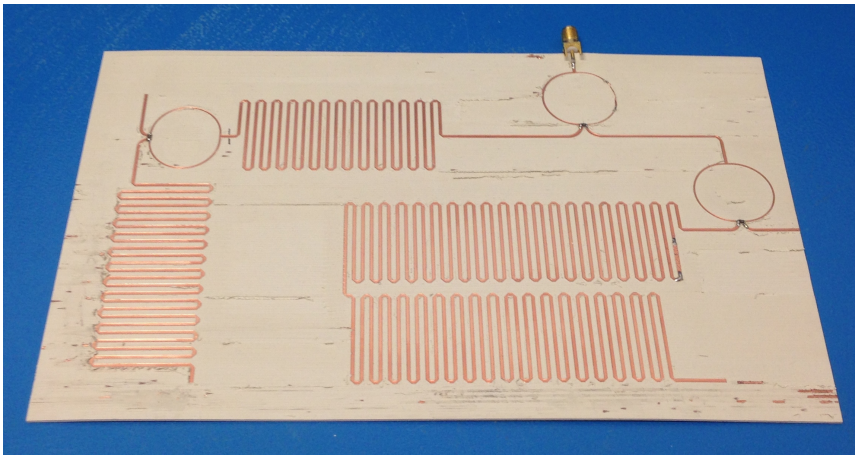

Figure 4.20: The fabricated microstrip 4-tap band-stop resonator with unequal power split ratio K =0.7 and a maximum delay of 22 ns. The dimensions are 22.5 cm x 13.5 cm.

4.21 shows a comparison between the measured S-parameters of the two boards. Measurements show a good agreement with the circuit simulation at frequencies around 770 MHz which is the same frequency on which the Wilkinson power splitters are designed. In order to obtain the same agreement on a wider band of frequencies, the power splitters should be designed using more than a single section of quarter wave transformers. The measured resonator with unequal power split ratio shows a 2 dB less insertion loss compared to the resonator designed with equal power ratio. The results of the measured resonator with K= 0.7 show a very high selectivity with a 3 dB bandwidth of 11 MHz only. A maximum insertion loss of 3.9 dB is also measured, in addition to more than 30 dB rejection with the stop band ripples reaching a peak of -25 dB. Furthermore, the 30 dB rejection appears at less than 20 MHz away from the pass band resulting in a high roll-off rate which exceeds 1 dB per MHz.

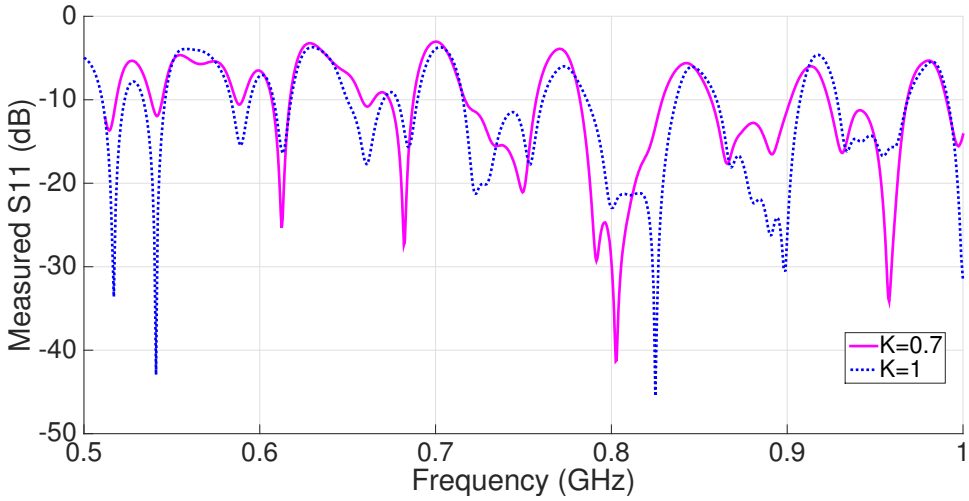

Figure 4.21: The measured s-parameter at the input of the fabricated 4-tap band-stop resonator with K =1 and K =0.7.

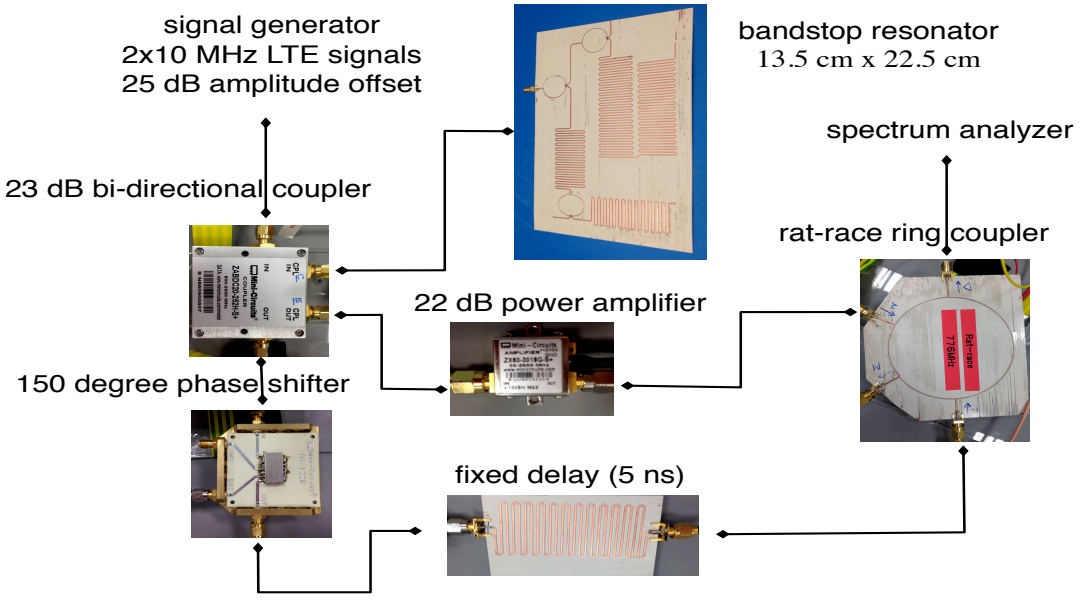

Figure 4.22: The test bench for the interference cancellation using the four-tap band-stop resonator (K= 0.7).

4.7 Experimental Results

4.7.1 Test Bench Setup

Fig. 4.22 shows the setup of the test bench used to demonstrate the feedforward interference cancellation system using the newly fabricated four-tap band-stop resonator with unequal power split ratio of K= 0.7. The test bench consists of a vector signal generator (Rhode & Schwarz SMU 200 A), a spectrum analyzer (Rhode & Schwarz FSL), a 20 dB bi-directional coupler (Mini-Circuits ZABDC20-252H-S+), a 24 dB gain amplifier (Mini-Circuits ZX60-3018G-S+) and a microstrip 3 dB Rat-Race-Ring coupler. The vector signal generator is configured to combine two LTE base band signals (A and B), whose symbol rates are adjusted such that each signal occupies a signal bandwidth of 10 MHz. A and B represent the wanted received signal and the interferer, respectively. The two signals are combined in the base band after a frequency offset and a path gain are assigned to signal B. The generator up-converts the combined signals to RF using the carrier frequency and the output power level assigned which are 795 MHz and -50 dBm, respectively.

Next, the output of the signal generator is connected to the FSL spectrum analyzer showing one modulated LTE signal. The path gain assigned to signal B is given a fixed value of 25 dB, while the frequency offset is given different values creating three test cases. In the first test case, the frequency offset is equal to 25 MHz. The interfering signal is located between 765 and 775 MHz with a peak power level of -25 dBm. The signal generator is then disconnected from the spectrum analyzer and injected to the input-port of the 20 dB coupler as shown in Fig. 4.22. The through-port of the coupler forms the main signal path, while the isolation-port forms the auxiliary path where a replica of the interferer is reconstructed. The coupled-port is terminated by the new band-stop resonator. Here, a fraction of the interferer signal is reflected back leaving a small fraction of the wanted received signal after being absorbed in the stop band of the resonator.

The reflected signal carrying a fraction of the interferer then leaves the coupler from the isolation-port reaching the amplifier, which is used to readjust the amplitude of the signal. The gain of the amplifier exceeds the coupling coefficient by 4 dB to account for the insertion loss of the band-stop resonator. Furthermore, a 5 ns microstrip meander delay is fabricated and connected to the through port of the coupler to compensate for the delay encountered in the auxiliary path. A voltage controlled phase shifter is also used to maintain zero phase difference between the two signal paths. Finally, the two signals are then subtracted using the Rat-Race-Ring coupler.

The test is repeated after reducing the frequency offset down to 20 MHz followed by 15 MHz for the second and the third test cases. At each time, the output of the signal generator is first connected directly to the spectrum analyzer to capture the input RF signal before applying it to the interference cancellation system.

4.7.2 Test Results

The measured results of the first test case show more than 45 dB cancellation at the center frequency of the interferer, and more than 25 dB cancellation over the whole band of the interfering signal, as seen in Fig. 4.23. The results also indicate more than 29.5 dB increase in the average signal to interferer power ratio (SIR), which is calculated before and after cancellation in the same figure. Measurements of the second and third cases with the frequency separation between the interferer and the edge of the received signal reduced to 15 MHz followed by 10 MHz, are shown in Fig. 4.24 and 4.25. In each case the voltage controlled phase shifter is slightly tuned and a successful cancellation for the interferer is obtained leaving the receiver band attenuated by less than 5 dB. The SIR is increased by more than 26.5 dB and 12 dB for the second and third test cases, respectively.

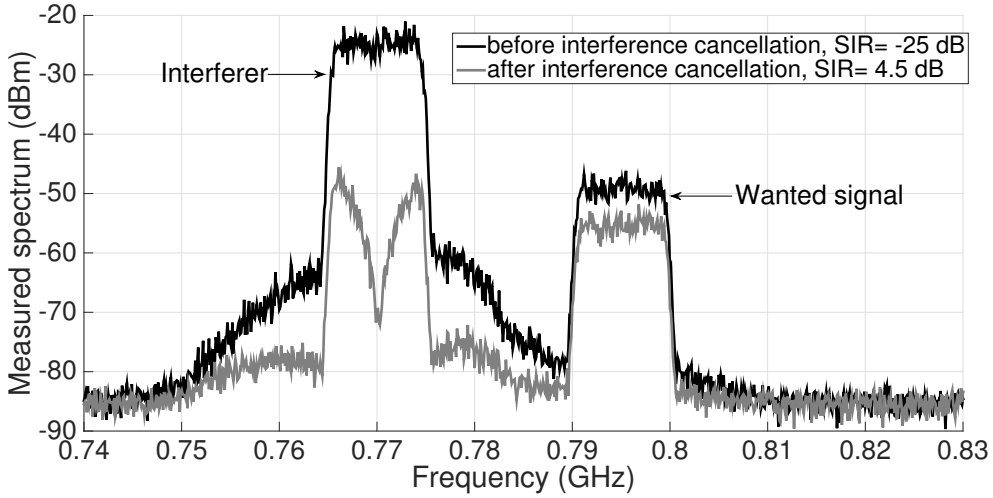

Figure 4.23: The measured power spectrum for the received signals before and after interference cancellation with (d) at 795 MHz, (i) at 20 MHz offset.

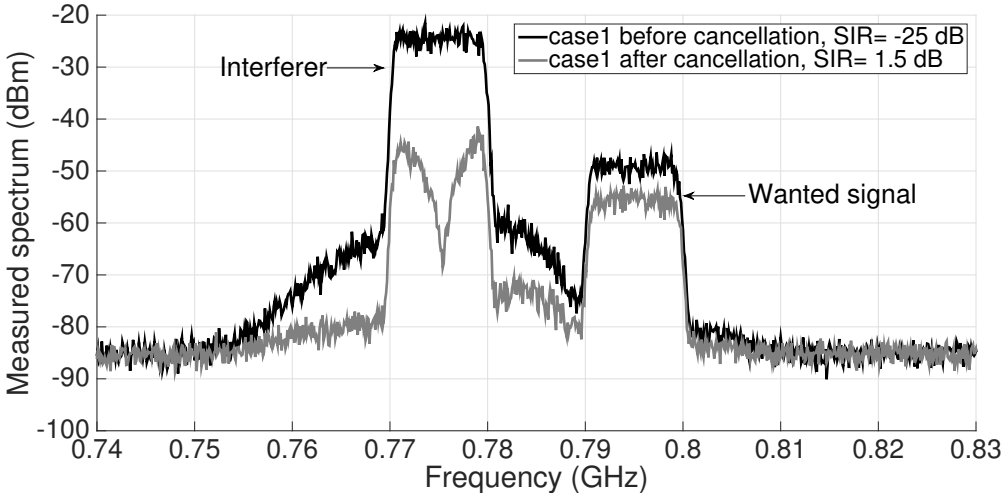

Figure 4.24: The measured power spectrum for the received signals before and after interference cancellation with (d) at 795 MHz, (i) at 15 MHz offset.

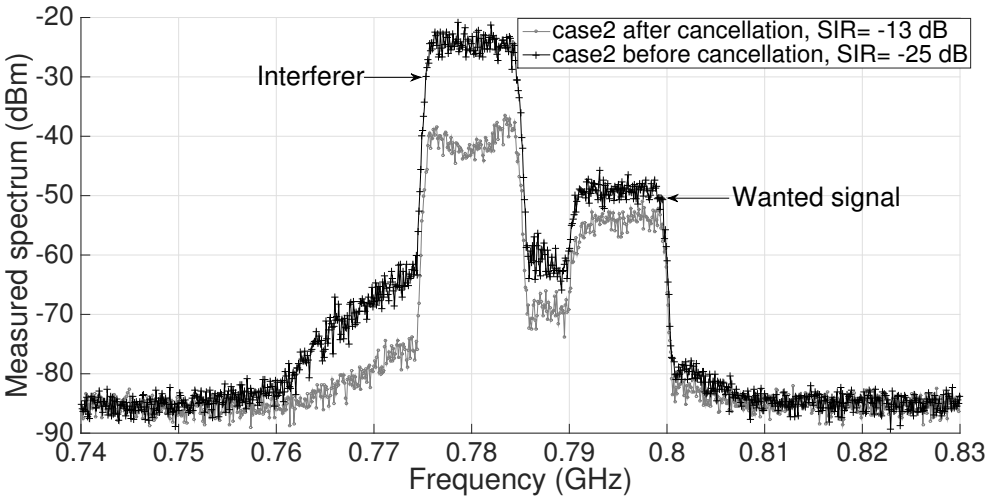

Figure 4.25: The measured power spectrum for the received signals before and after interference cancellation with (d) at 795 MHz, (i) at 10 MHz offset.

4.8 Conclusion

High power Wideband interferers appearing at 20, 15 and 10 MHz away from the receiver band edge can now be suppressed by applying a feedforward cancellation system using the new four-tap band-stop resonator, which is designed in this chapter. The new band-stop resonator is designed based on tapped delay line filter structures, which are implemented in the RF domain. The new design is named as “Multi-Tap Delay Resonator” as it consists of multiple transmission line delay taps. It offers high selectivity, high rejection and higher than 1 dB per MHz roll-off rate.

4.8.1 Summary of the Results

- Three different prototypes for the new resonator are evaluated by applying mathematical analysis and circuit simulations. The signal taps are characterized by uniform amplitude distribution and delay step in the first prototype, non-uniform amplitude distribution in the second prototype and non-uniform delay step in the third prototype. The circuit analysis of the second prototype achieved 10 dB more

stop band rejection for the same number of taps when compared to the two other prototypes.

- A new methodology is introduced to optimize the amplitude ratio between N number of taps based on Chebyshev algorithm. According to the optimization results, more than 20 dB stop band rejection can be obtained using a four tap resonator given that the power split ratio among the outer and the inner delay taps is less than 0.6.

- A four-tap microstrip band-stop resonator with non-uniform amplitude is designed with 0.7 power split ratio instead of 0.6 to facilitate the fabrication process. Measurements of the resonator indicate a very high selectivity with a 3 dB bandwidth of 11 MHz only, in addition to a high stop-band rejection of more than 30 dB with the stop band ripples reaching a peak of -25 dB and a maximum insertion loss of 3.9 dB. These losses can however be compensated by re-adjusting the gain of the amplifier in the auxiliary path in the feedforward interference cancellation system, thus no degradation in the system performance is going to take place due to that loss.

- A test bench is setup to evaluate the performance of interference cancellation using the new fabricated four-tap resonator. Two 10 MHz LTE modulated signals are used to represent the desired received signal (-50 dBm) and the interferer (-20 dBm). The power spectrum measurements show more than 45 dB cancellation for interferers located at 20 and 15 MHz frequency separation from the receiver, while a 20 dB rejection for the interferer located at 10 MHz away. The measured insertion loss in the receiver band after interference cancellation is less than 5 dB. These losses are caused by a number of factors, which are the losses of the voltage controlled phase shifter and the large fixed delays lines in the main path of the feedforward loop, in addition to the amplitude and phase mismatches between the two paths of the feedforward loop. The results have also shown absolutely no degradation in the

Table 4.3: Summary of the measured parameters and comparison

	[29]	[50]	[32]	This work
Filtering domain	IF	Digital	Digital	RF
Cancellation domain	IF	RF	N/A	RF
Frequency offset	20 MHz	21 MHz	>60 MHz	20-10 MHz
Attenuation amp.	23- 26 dB	24 dB	18 dB	23 dB
Attenuation BW.	<1 MHz	8 MHz	6 MHz	10 MHz
In-band losses	< 1dB	> 5 dB	2.8 dB	> 5 dB
SIR improvement	+17 dB	+24 dB	+15 dB	+29.5 dB
P-1dB, IIP3 (dBm)	-29.5, -	<-30 dBm	6, >17	12.8, >25

noise figure at all measured frequencies which is a big advantage of employing RF filtering and cancellation systems. Overall, the signal to interference ratio (SIR) is improved by more than 29.5, 26.5 and 12 dB for interference at 20, 15 and 10 MHz.

4.8.2 Evaluation of the Results

A comparison is made between the results obtained in this chapter and three of the interference cancellation techniques previously discussed in Chapter II. The three techniques are the feedforward interference cancellation at intermediate frequency (IF) [29]; the hybrid RF-DSP interference cancellation [50]; and the N-path digital notch filtering [32]. Table. 4.3 shows a summary for the results of the comparison. The results indicate that the technique introduced in this chapter succeeded to perform a high rejection for wide band interferers at smaller frequency offsets with acceptable insertion losses and reasonable implementation complexity. It has provided the highest improvement in the SIR level which is the main concern of this research. Unlike all other previous solutions, RF feedforward interference cancellation has not altered the noise figure of the receiver, which is another big advantage for the solution presented. Furthermore, a higher 1 dB compression point is obtained, when compared to the previous solutions from the literature. This makes the system more capable of handling public safety interferers whose power levels can reach the receiver with more than -15 dBm.

4.8.3 Limitations

As the interference signal appears closer to the receiver, larger group delays will be required in the design of the band-stop resonator. Here, the implementation of these delays uses true delay transmission lines whose length exceeds 2.0 m. The use of microstrip meander lines and a high permittivity substrate have managed to reduce the dimensions of the circuit down to 10 cm x 10 cm, which is still relatively large in size considering the small cell application. Hence, the objective of the following chapter is to examine the large delay properties of composite right left handed transmission lines in separating the interferer from the receiver signal with the aim to reduce the size of the resonator.

4.8.4 Contributions

In this chapter, a new design method is introduced for constructing high selective band-stop resonators using RF tapped delay lines, which enable separating two wide band signals that are less than 20 MHz away from each other. A mathematical analysis is also introduced on each of the parameters used to construct the resonator, in addition to an optimization method for increasing the stop-band attenuation. The new resonators are implemented and successfully tested as a separate component and after being impeded in the feedforward cancellation system test bench. The test results achieved successful cancellation for 10 MHz signals appearing at 20, 15 and 10 MHz away from the receiver band.

Chapter 5

CRLH-TL Model Based Resonator for Interference Filtering

5.1 Introduction

This chapter studies the design of high selective band-stop resonators using artificial left-handed transmission lines. As the propagating electromagnetic (EM) fields experience a large time delay, a fast change in the phase characteristics is obtained. This implies a fast switching in the amplitude response from a maximum to a minimum over a narrow frequency band. Accordingly, high selective band-stop resonators require the use of large time delay elements. In the previous chapter, true time delay transmission lines are employed in the design of high selective band-stop resonators. These lines provide a constant large group delay, which is independent of the operating frequency. Knowing that, band-stop resonators do not necessitate maintaining a large delay over an infinite band of frequencies, more research is carried on other microwave structures, specifically left-handed transmission lines, searching for an alternative design that can improve the efficiency of band-stop resonators in terms of size and complexity. The alternative design must still provide a large group delay, while covering a sufficient frequency band of

not more than 100 MHz. In fact, less than 100 MHz can also be sufficient, since it is only required to cover the total bandwidth of the receiver (< 10 MHz), in addition to the interfering signal (<10 MHz), and the frequency separation between the two, which is not meant to exceed 25 MHz.

The chapter starts by describing a new observation on the behavior of the group delay of left-handed transmission line circuit model at the Bragg cutoff frequency, given that the model is constructed using a finite number of cells. The observation is explained in Section 5.2 by applying circuit simulations using ideal RF components from Passive System Library in ADS 2015. Section 5.3 presents the employment of the new theory in developing a new design for band-stop resonators using left-handed transmission line circuit model. Three band-stop resonators are designed and simulated using different number of cells corresponding to different roll-off rates and operating bandwidths. Furthermore, tuning the center frequency of the stop band using variable capacitors, is explained at the end of this section. Section 5.4 presents the microstrip implementation of the composite right left-handed (CRLH) band-stop resonator. In addition, it demonstrates the full EM simulation performed to combine the non-ideal effects of the RF circuit in order to increase the accuracy of the results, while optimizing the circuit dimensions. Finally, Section 5.5 demonstrates the feedforward interference cancellation system setup evaluating the new CRLH-TL band-stop resonator. The setup is used for testing the cancellation of interferers located at 20, 15 and 10 MHz away from the edge of the receiver band using two-cell and three-cell CRLH band-stop resonators.

5.2 A New Observation on the Bragg Cutoff of Artificial LH Transmission lines

Left-handed transmission lines, which are also known as metamaterials, are defined as any transmission medium that can exhibit negative values for permittivity and permeabil-

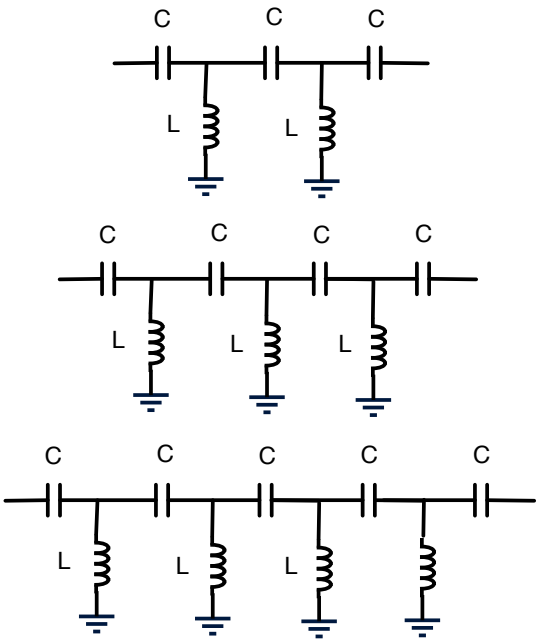

Figure 5.1: The equivalent circuit model of LH transmission line constructed using using two cells, three cells and four cells.

ity simultaneously over the same frequency range. This results in an inverse EM wave propagation. Several studies were conducted on analyzing the behavior of the inverse propagation of the EM-fields using artificial left-handed transmission line, which can be seen as the lumped circuit model of metamaterials. Artificial left-handed transmission line can be constructed from a cascade of series capacitors and shunt inductors [60]. Studies have also introduced the "Bragg Cutoff" term defined as the frequency at which the left hand propagation mode starts to propagate [61]. The Bragg Cutoff is a function of the equivalent series capacitance and shunt inductance used to construct the line circuit model as described in Eqn. 5.1. This definition is based on the assumption that the number of cells used to implement the lumped circuit model for the line is infinite . In this chapter, a new observation is made which points out that the Bragg Cutoff of artificial left hand transmission lines constructed using a finite number of cells is no longer a function of the lumped elements only, but also the number of cells.

$$f_{Bragg} = \frac{1}{4\pi\sqrt{LC}} \tag{5.1}$$

5.2.1 Mathematical Analysis

In this section, a mathematical analysis is performed to analyze the effects of the number of cells on the frequency response of artificial left-handed transmission lines. A two-cell line is composed of two T-networks and two series capacitors, as shown in Fig. 5.2. The equivalent characteristic impedance of a unit T-network can be given using Eqn. 5.2, while the phase response of the same unit cell is defined in Eqn. 5.3 [63]. By cascading two T-networks, the overall characteristic impedance remains the same and the phase is doubled as illustrated in Fig. 5.3. In this case, the input impedance seen from one side of the line ($Zin'_{n=2}$) can be given using Eqn. 5.4, given that the line is terminated by a load impedance Z_L at one end. The two capacitors are then inserted at the terminals of the line as shown in Fig. 5.3 and the total input impedance ($Zin_{n=2}$) is calculated in Eqn.

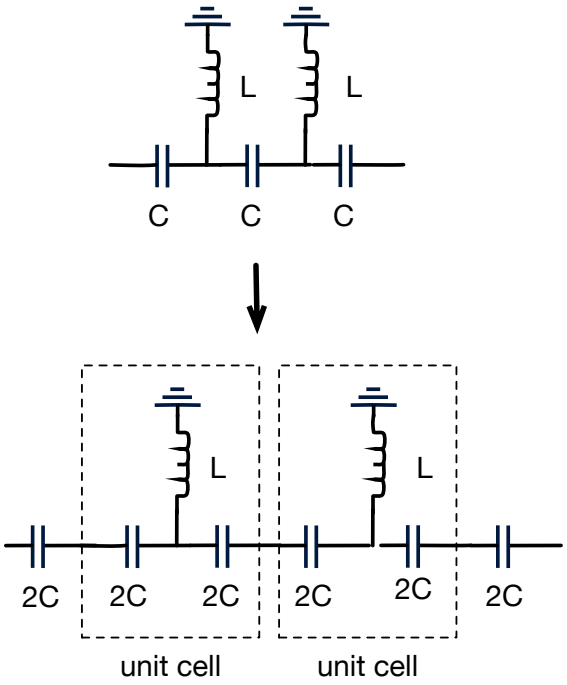

Figure 5.2: The decomposition of the two-cell artificial left-hand transmission line into two T-networks and two series capacitors.

n	C	L	Z_o	Z_c	Y_l	Z_L
2, 3, 4	3.0 pF	5.95 nH	50Ω	$\frac{-j}{2\pi fC}$	$\frac{-j}{2\pi fL}$	50Ω

Table 5.1: The parameters used in the mathematical analysis for the finite cell artificial left-hand transmission line, where Z_o is the characteristic impedance of the line, Z_c is the impedance of the capacitor and Y_l is the admittance of the inductor.

5.5. The input reflection coefficient can also be computed using Eqn. 5.6. By plotting the reflection coefficient in Matlab using the parameters in Table. 5.1, the effects of changing the number of cells (n) can be noticed by looking at the 3 dB cutoff frequency on each curve, as shown in Fig. 5.4.

$$Z_{unit} = \sqrt{Z_c(Z_c - \frac{2}{Y_l})} \tag{5.2}$$

$$\phi_{unit} = 2sin^{-1}(j\sqrt{\frac{Z_cY_l}{2}}) \tag{5.3}$$

$$Zin_n^{'} = Z_{unit}\frac{Z_{unit} + jZ_Ltan(n\phi_{unit})}{Z_L + jZ_{unit}tan(n\phi_{unit})} \tag{5.4}$$

$$Zin_n = Z_{unit}\frac{Z_{unit} + j(Z_L + Z_c)tan(n\phi_{unit})}{(Z_L + Z_c) + jZ_{unit}tan(n\phi_{unit})} + Z_c \tag{5.5}$$

$$\Gamma_n = \frac{Zin_n - Z_o}{Zin_n + Z_o} \tag{5.6}$$

The results of the mathematical analysis performed above have indicated a 3 dB cutoff frequency of 626, 645, and 687 MHz for the two-cell, three-cell and the four-cell artificial left-hand transmission lines, respectively.

This observation can also be noted by applying circuit simulations on the same three artificial transmission lines: the two-cell line; the three-cell line and the four-cell line shown in Fig. 5.1, while using the same values in Table 5.1. The Bragg Cutoff of the infinite line

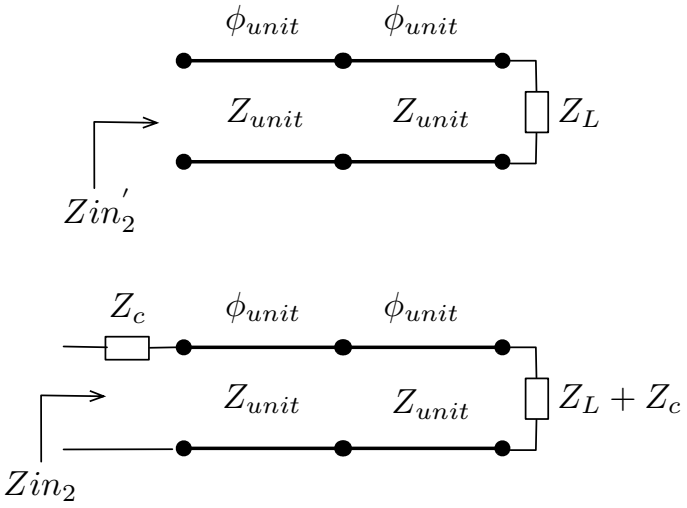

Figure 5.3: The transmission line equivalent circuit for the two T-networks.

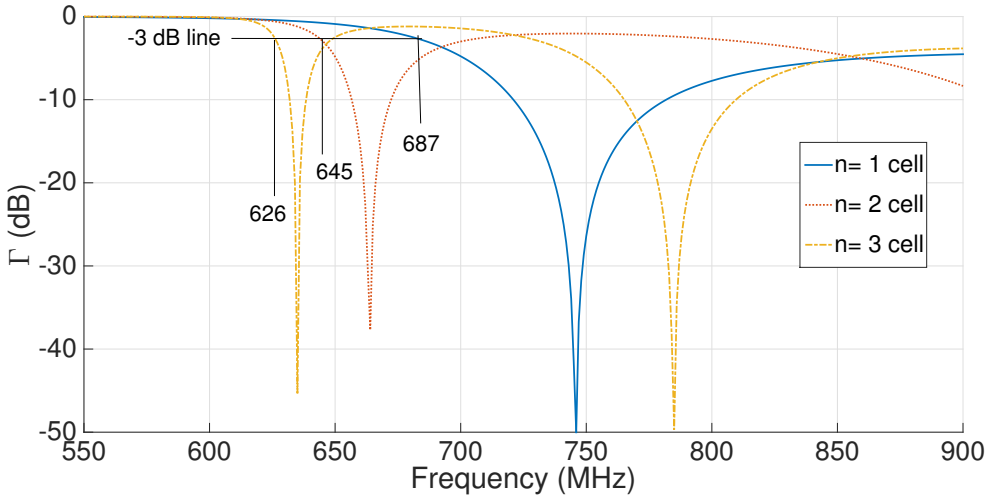

Figure 5.4: The matlab plots for the reflection coefficient of finite cell artificial left-hand transmission lines, which is defined in Eqn. 5.6 and using the parameters in Table. 5.1.

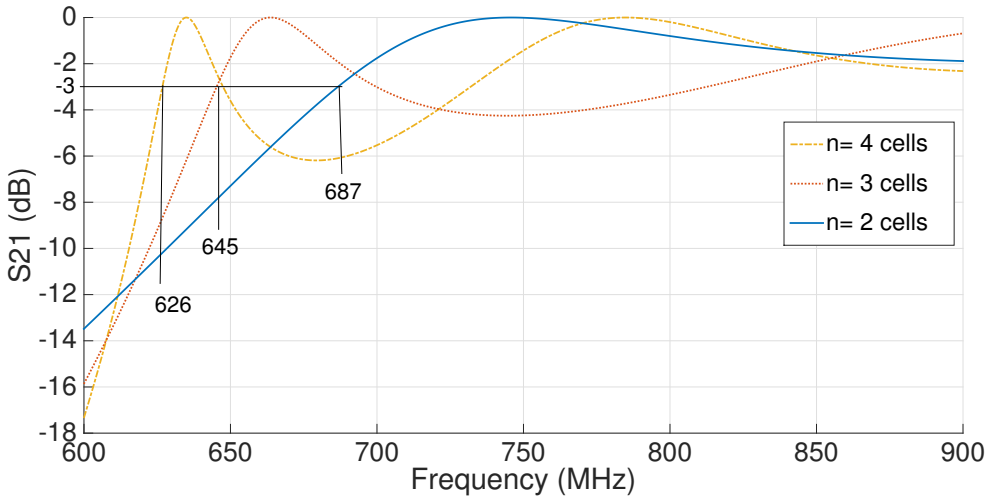

Figure 5.5: The simulated transmission S-parameter of the three circuit models of LH-TL constructed using two cells, three cells and four cells.

is 595 MHz, which is calculated according to Eqn. 5.1. On the other hand, the simulations results show different values for the cutoff frequency. The new cutoff frequencies match those calculated above using Matlab. Fig. 5.5 shows the simulated S-parameters for the three different lines in Fig. 5.1, which indicate that each of the three lines act as a high pass filter whose 3 dB cutoff frequency can match the definition of the Bragg Cutoff. According to the results, the three lines have formed three different high pass filters, with different amplitude ripples in the pass band as well as different cutoff frequencies. This is due to the variations in the Bragg Cutoff of the left hand propagation mode, as it is shifted between 626 MHz, 645 MHz, and 687 MHz for the two-cell, three-cell and four-cell transmission lines. As the number of cells increases, the Bragg Cutoff frequency decreases until it reaches the value defined by Eqn. 5.1.

Moreover, the three transmission lines are terminated by a short circuit at one end and the same S-parameters simulations are applied, while extracting the group delay of the reflection coefficient. Fig. 5.6 shows the simulated group delays for the three lines, which again demonstrates how the location of the group delay peaks varies as a result

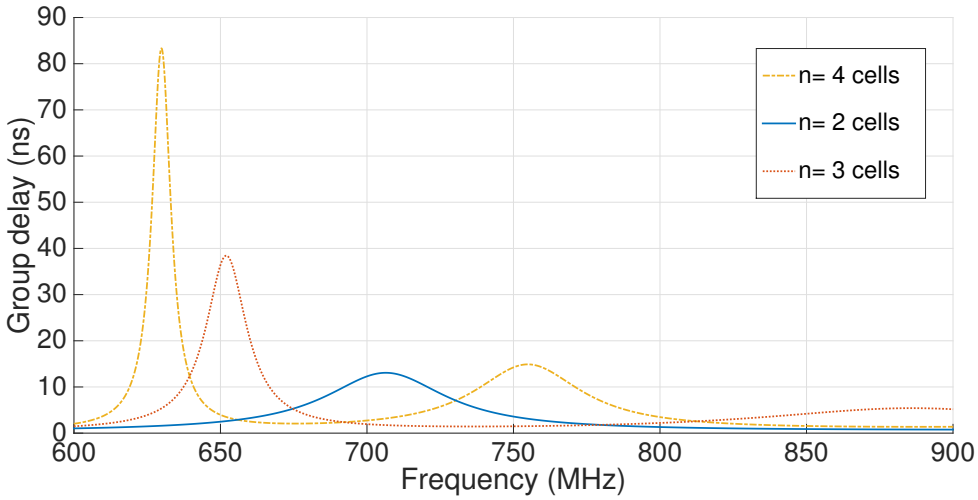

Figure 5.6: The simulated group delay of the reflection coefficient for the circuit model of pure LH-T lines constructed using different number of cells, given that each circuit is terminated by a short circuit at one end.

of the shifts in the Bragg Cutoff frequencies. Knowing that, the EM propagating fields experience an anti-parallel phase and group velocities at the Bragg Cutoff of the line, which allows it to convey energy leading to a significant rise in the group delay [61]. Furthermore, it can be noticed that the bandwidth of the region where the group delay significantly rises decreases with the increase in the number of cells forming the line. This is due to the increase in the amplitude of the pass band ripples, which rises significantly with increasing the number of cells.

In this chapter, the significant rise in the group delay of the three artificial left-handed transmission lines has become advantageous, since these small sections of lumped elements can be used to replace the large true delay transmission lines in the band-stop resonators designed in the previous chapter. Unlike true delay lines, artificial transmission lines exhibit large group delays over a narrow frequency bandwidth, which are insufficient to form the maxima and minima required to separate interfering signals from the receiver band. According to the results in Fig. 5.6, group delays are larger than 10 ns over a 25 MHz bandwidth for the two-cell, and 20 MHz for the four-cell line.

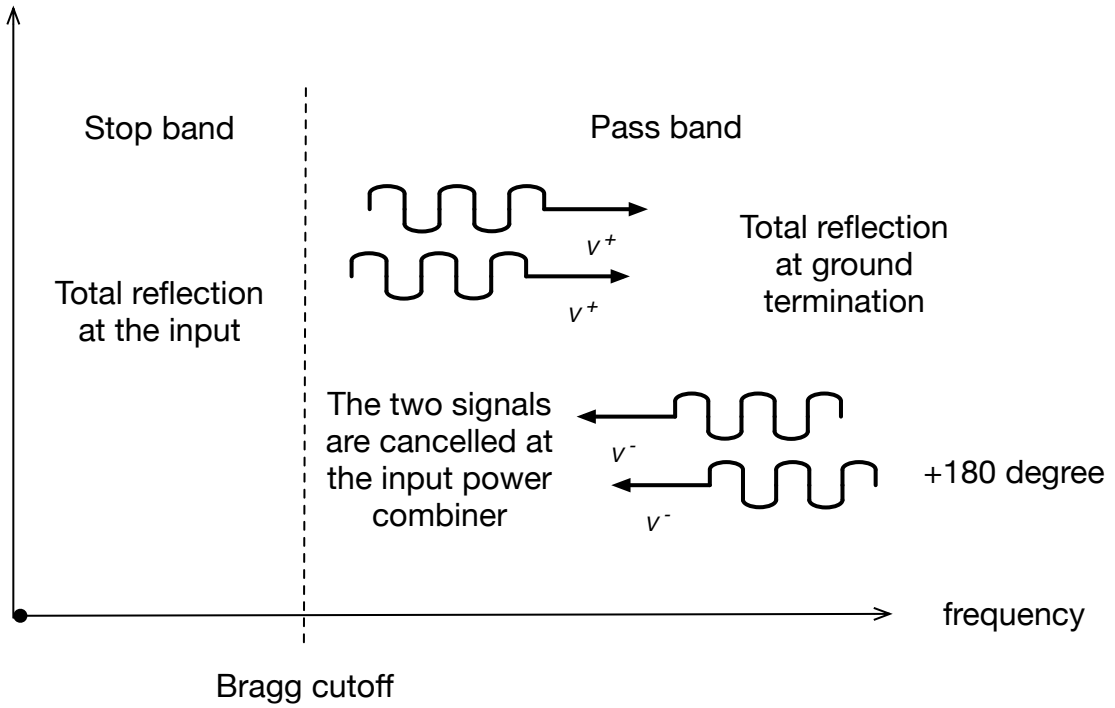

Figure 5.7: A diagram showing the mechanism of LH band-stop resonators.

Nevertheless, the separation of wide band interfering signals using artificial left-handed transmission lines can still be made possible, as they can be seen as high pass filters, whose pass and stop bands are separated by the Bragg Cutoff. In these lines, all frequencies below the Bragg Cutoff are totally reflected, while the frequencies above the Bragg Cutoff are transmitted through the line, but the transmission losses are very high due to the large pass band ripples in the frequency response. After terminating the line with a short circuit at one end, only a small fraction of the wave at frequencies above the Bragg Cutoff is absorbed. In this case, the separation of the two signals can be very poor, since the large pass band ripples can not be avoided.

The only way to improve the separation is to guarantee that frequencies above the Bragg Cutoff are totally transmitted to the short circuit termination. In other words, these frequencies are totally absorbed by the termination. This can be achieved by constructing

two different length artificial transmission lines with a phase difference of 180 degree at frequencies above the Bragg Cutoff. Upon splitting the RF signal equally on the two lines, all frequencies below the Bragg Cutoff are reflected and all frequencies above the Bragg Cutoff are cancelled, as illustrated in Fig. 5.7.

The phase difference can be obtained by increasing the number of cells in one of the two lines, however increasing the number of cell will always alter the location of the Brag Cutoff as mentioned earlier. This leads to a second condition, which states that the two lines must exhibit the same Bragg Cutoff frequency. In this chapter, a new idea is proposed for how to use artificial left-handed transmission lines while satisfying the conditions above to successfully implement a band-stop resonator separating wide band interference signals.

5.3 The Structure of the New LH Band-Stop Resonator

Similar to Multi-Tap Delays, the structure of the new LH band-stop resonator proposed in this chapter is based on dividing the RF signal among two short terminated taps. Each tap is designed to add a different phase shift as well as a different group delay. The two taps are constructed using artificial left-handed transmission lines, whose series capacitance and inductance are selected so that Bragg Cutoff matches the cut off frequency of the resonator. The number of cells used to construct the artificial lines in each tap must be selected so that the group delay in one tap is equal to double the group delay of the other. This can be achieved by introducing double the number of cells of the first tap to the second one. However, not only the number of cells is to be doubled up, but the whole circuit used in the first tap must be duplicated twice in the second tap. In this case, the second tap will have two identical capacitors in series at the middle of the circuit. The reason for duplicating the circuit rather than doubling up the number of cells, is to maintain the same Bragg Cutoff for the two taps, which is necessary to obtain a common

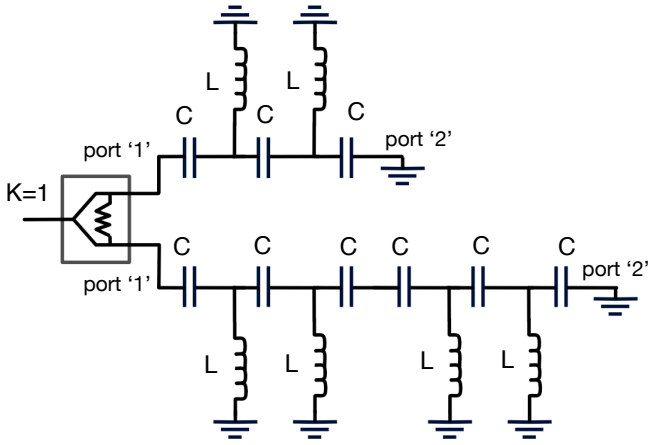

Figure 5.8: The equivalent circuit model of the new band-stop resonator constructed using two cells and their duplicates. All capacitors (C) are 3.0 pF, while inductors (L) are 5.95 nH.

stop band for the frequencies located below the Bragg Cutoff.

5.3.1 A Two-cell Band-Stop LH Resonator

Fig. 5.8 shows the proposed circuit structure of a two-cell band-stop resonator constructed using the same capacitance and inductance values in the previous section. It consists of a Wilkinson RF power splitter or combiner, whose power split ratio K is equal to 1. The first tap is formed of a two-cell transmission line, while the second tap is formed of a duplicated two-cell transmission line. The two-cell lines consists of three series capacitors and two shunt inductors, and the duplicated two-cell consists of six series capacitors and four shunt inductors. The LC network in the first tap starts and ends with a series capacitor, so that it features the reciprocity of transmission line networks. Another form for the circuit model of these resonators can be constructed using three shunt inductors and two series capacitors in the first tap followed by their duplicates in the second tap. In this case, an open circuit termination replaces the short termination at the end of each tap, as shown in Fig. 5.9.

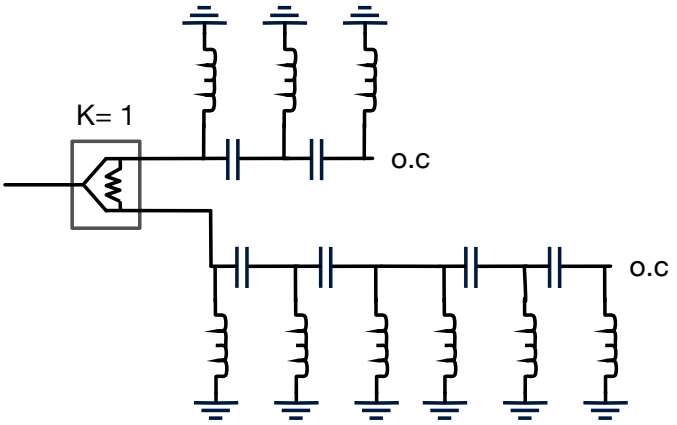

Figure 5.9: Another form for the circuit model of the new band-stop resonator.

To prove that the two artificial lines in the two taps are now sharing the same Bragg Cutoff, the transmission coefficients of the two lines are first simulated before placing the short circuit terminations. Fig. 5.10 shows the simulation results for the transmission coefficient, which indicate that the Bragg Cutoff of the two taps are less than 10 MHz away, and the shared pass band between the two forms is more than 50 MHz.

The two taps are then terminated with a short circuit at the end, and both the magnitude and the phase of the reflection coefficient at the input of each of the two taps are simulated, as shown in Fig. 5.11. The results show a 0 dB reflection coefficient for both taps, which indicate a total reflection for the signal at all frequencies. At the same time, the two lines show a nearly equal response at all frequencies above the Bragg Cutoff, then, the phase difference between the two lines has switched from 0 degree to a 180 degree at 706 MHz. Two more frequency points have also shown a phase difference of 180 degree between the two lines, which are 717 and 736 MHz, as shown in Fig. 5.11.

As mentioned earlier, a large variation in the group delay is always required to alternate the phase by 180^o over a narrow frequency band. By plotting the group delay of the two shorted transmission line taps, it can be seen that large delay variations have appeared between the two taps at frequencies higher than the Bragg Cutoff, except for

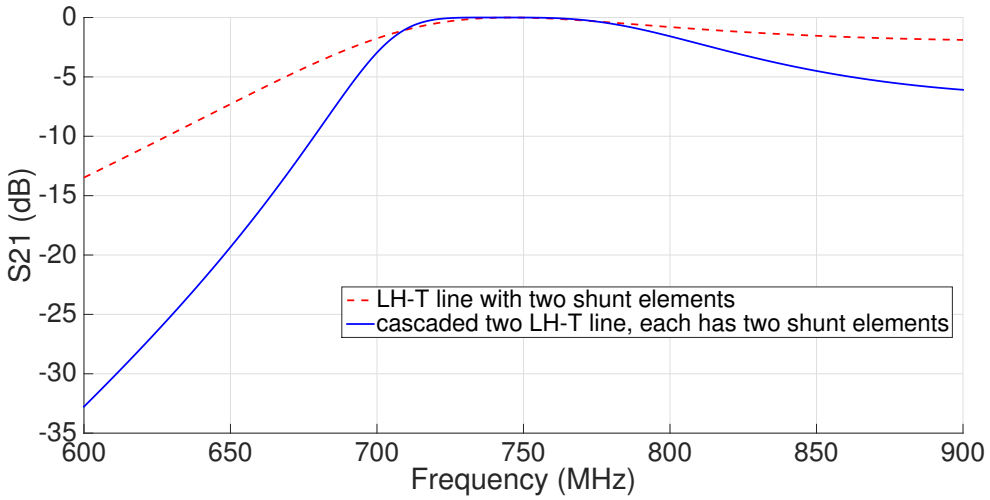

Figure 5.10: The simulated S-parameters of the two branches of LH-T lines forming the new band-stop resonator in Fig. 5.8.

two frequency points, which are 710 and 726 MHz, as shown in Fig. 5.12.

Fig. 5.13 shows the simulated phase and group delay difference between the two taps. It can be noticed that the phase difference is maintained around 180^o starting from 706 MHz and until 736 MHz. This 30 MHz bandwidth marks the stop band region of the resonator. The group delay difference have also shown a significant rise from 0 up to more than 45 ns in less than a 10 MHz bandwidth, which means that the resonator can be used to separate two signals that are 10 MHz apart. Fig. 5.14 shows the simulation results for the magnitude of the reflection coefficient seen at the input of the resonator constructed using these two taps. The results show three transmission zeros appearing in the frequency response of the resonator, which corresponds to the three out of phase points in Fig. 5.11 and 5.13. The first two transmission zeros also refer to the positive peak delay of the first tap and the negative peak delay of the second one indicated in Fig. 5.12. On the other hand, the two ripples appearing in the stop band are caused by the intersection of the group delays of the two taps as also indicated in the same figure.

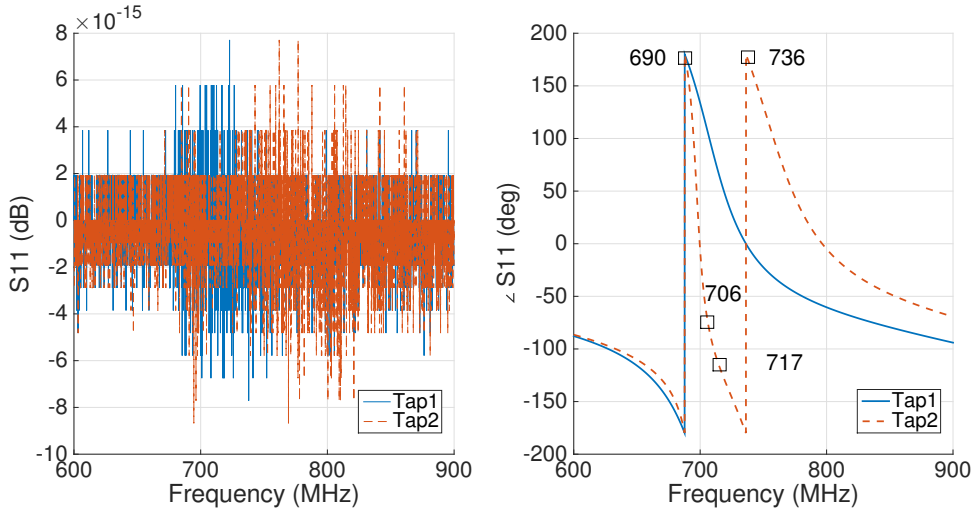

Figure 5.11: The simulated amplitude and phase response of the two short terminated taps forming the two-cell band-stop resonator in Fig. 5.8.

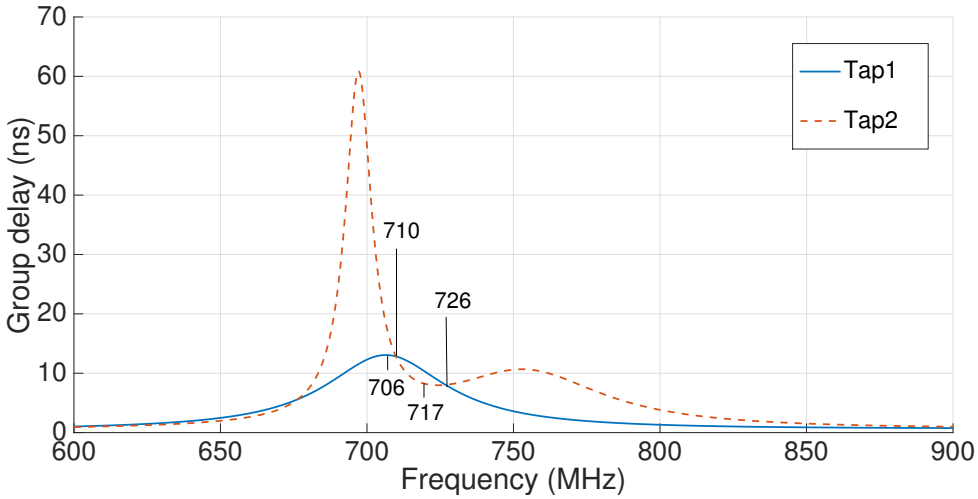

Figure 5.12: The simulated group delay of the two short terminated taps forming the two-cell band-stop resonator in Fig. 5.8.

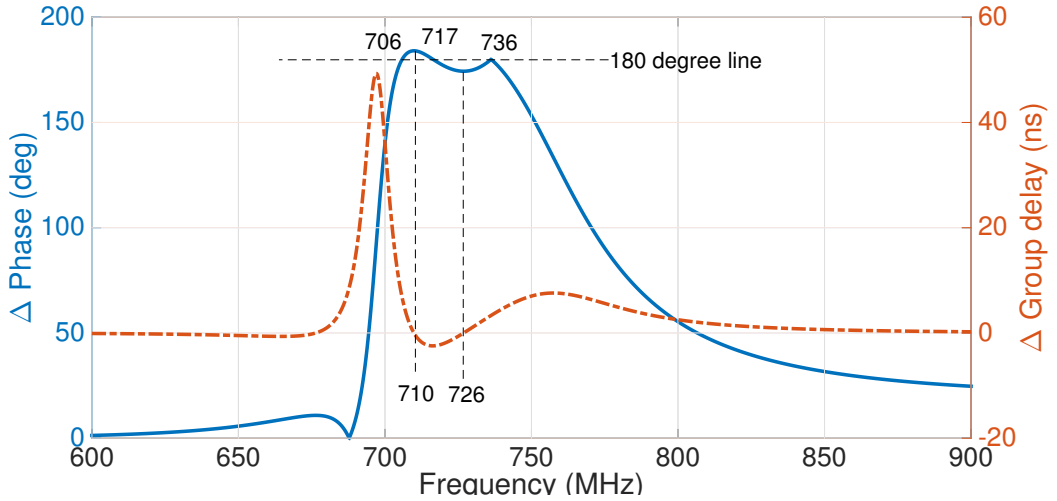

Figure 5.13: The simulated phase and group delay difference between the two short terminated taps forming the two-cell band-stop resonator in Fig. 5.8.

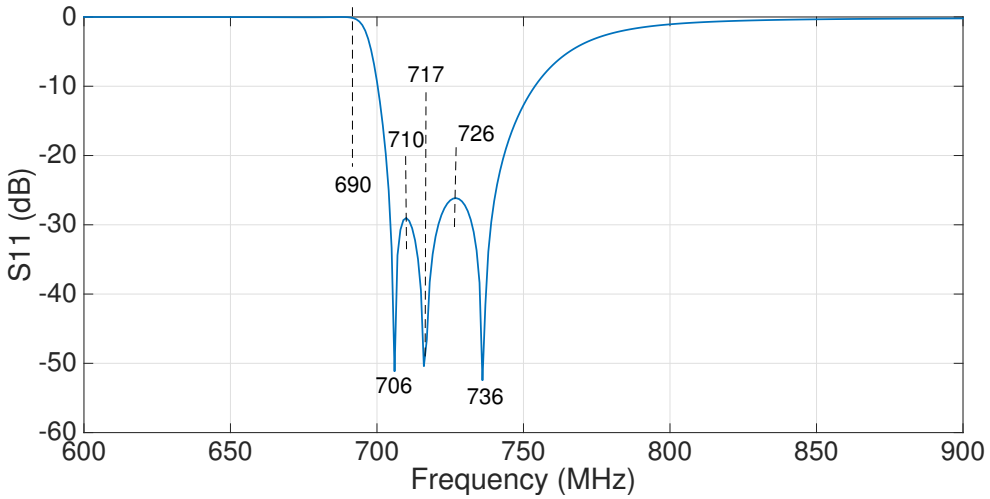

Figure 5.14: The simulated amplitude response or the reflection coefficient at the input of the two-cell band-stop resonator in Fig. 5.8.

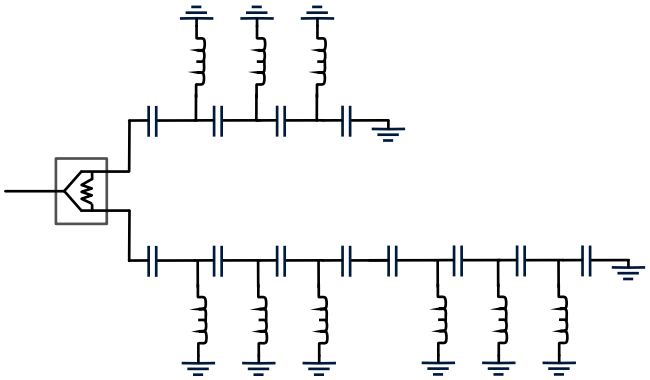

(a) three-cell band-stop resonator

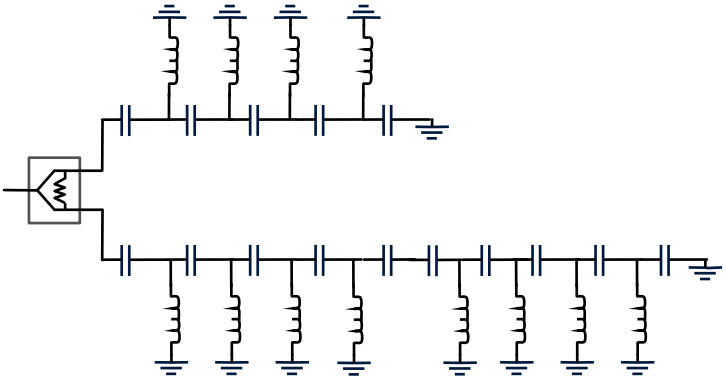

(b) four-cell band-stop resonator

Figure 5.15: The circuit model of three-cell (a) and four-cell (b) band-stop resonators, given that all the inductors and capacitors are equal to 5.95 nH and 3.0 pF, respectively.

5.3.2 Three-cell and Four-cell Left-Hand Band-Stop Resonator

Here, the effect of increasing the number of cells on the frequency response of the band-stop resonator is demonstrated. Increasing the number of cells in the two taps of the resonator increases the difference in group delay between them, which is necessary to increase the roll off rate. This increases the ability of the resonator to handle interferers appearing at closer frequency separation from the receiver. Fig. 5.15 shows a three-cell and a four-cell band-stop resonators constructed similar to the two-cell resonator above. Fig. 5.16 shows the simulation results of the three band-stop resonators. The results

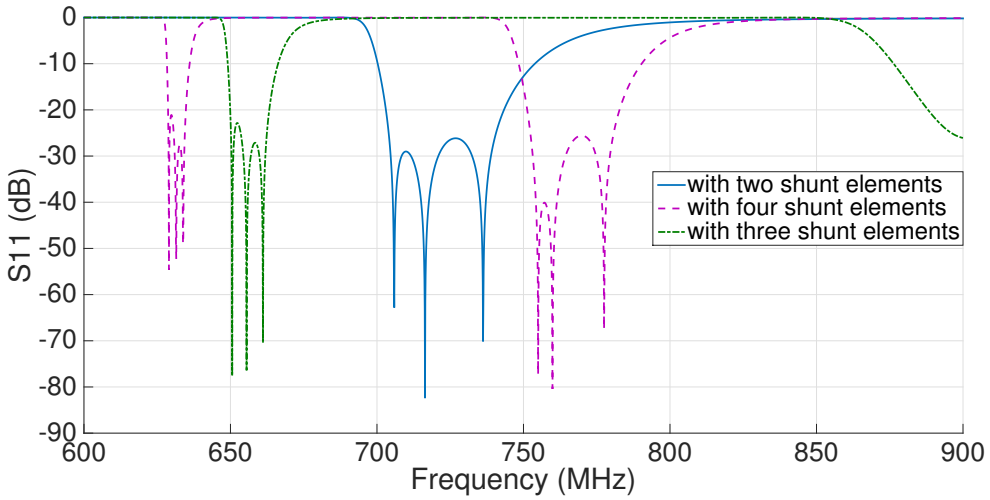

Figure 5.16: Simulations for the magnitude of the reflection coefficient at the input of the new band-stop resonators constructed using different number of cells.

are showing another important effect of increasing the number of cells, which is having the gaps between the three transmission zeros as well as the bandwidth of the stop band significantly reduced. This is due to the nature of the frequency response for the group delay of artificial left-handed transmission lines in general. On the other hand, the rejection roll off rate increases significantly. A further increase in the number of cells can result in eliminating two transmission zeros, and only one notch is created. The reason is the cutoff frequency of each tap starts to converge back to the theoretical Bragg Cutoff, which is previously defined for an infinite number of cells.

5.3.3 Tunable Left-Hand Band-Stop Resonator

As the LTE standard features carrier aggregation, which adopt flexible channel bandwidths between 1.4 MHz and 20 MHz, the location of the interferer as well the wanted received signal can vary. In this case, tuning the stop band of the resonator used to separate these two signals becomes essential. An interesting fact about the new design of band-stop resonators, proposed in this chapter, is that the cutoff frequency can be easily

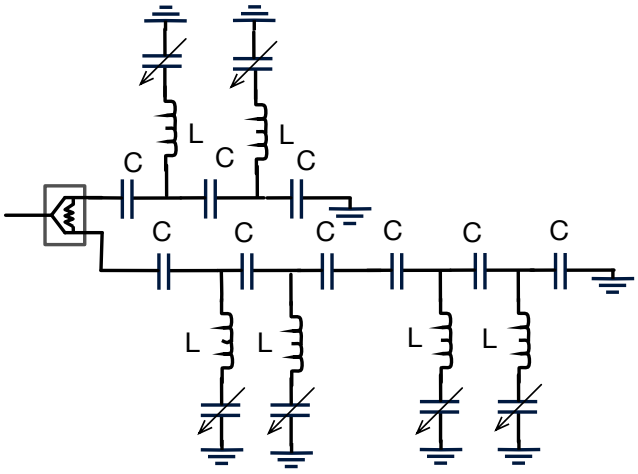

Figure 5.17: The structure of a varactor tuned two-cell CRLH band-stop resonator. L= 6.75 nH and C= 3.0 pF.

tuned by varying either the series capacitance or shunt inductance of the circuit. Voltage controlled capacitors (known as varactors) can be used to tune the shunt inductance of the resonator, as illustrated in Fig. 5.17. Varactors with low capacitance values can alter the rejection of the resonator, however increasing the shunt inductance can eliminate these effects. The tuning performance can be tested by carrying simulations for the amplitude response of the band-stop resonator after placing a varactor whose variable capacitance (VC) is set between 20 pF and 80 pF. After placing the varactor in the schematic, the shunt inductance is slightly increased from 5.95 nH to 6.75 nH to readjust the level of the stop-band ripples. Fig. 5.18 shows the simulation results with a 100 MHz tuning range for the cutoff frequency. Tuning the new band-stop resonator over larger bandwidths is not recommended, since it can result in raising the level of the stop band ripples to above -20 dB.

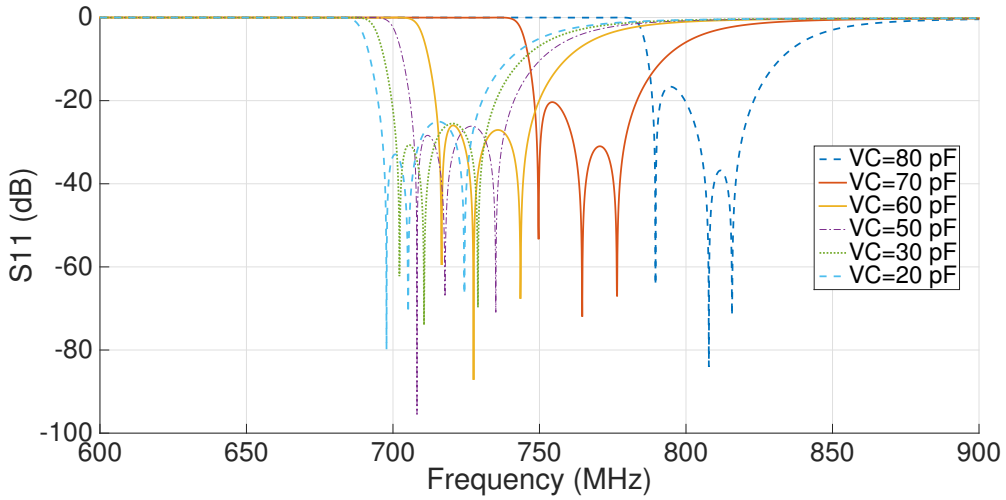

Figure 5.18: Simulations results for tuning the band-stop resonator with VC values between 20 and 80 pF.

5.4 Microstrip Implementation of CRLH Band-stop Resonators

Pure left-handed transmission lines can not be practically implemented using Microstrip technology, since they require extra sections of right handed transmission lines to connect the series capacitors and shunt inductors. These extra sections create what is known as composite right left-handed transmission lines (CRLH-TL) [62]. These sections introduce extra parasitic capacitances and inductances altering the behavior of the left-handed fields. Their effect can be avoided by increasing both the series capacitance and shunt inductance of the left-handed line [62].

All series capacitors are replaced by lumped elements, whereas the shunt inductors are realized using $50\,\Omega$ short circuited stubs. The stubs are terminated by solid ground vias. The RF circuit design tool in Agilent ADS is used to build the Microstrip layout of the power divider, whose output ports are also connected to the left-handed lines. Standard FR4 dielectric material is selected with a thickness of 1.6 mm. The dimension of the short circuited stubs are determined by applying the following steps:

1- Choose a random value for the length of the transmission line stub (L).

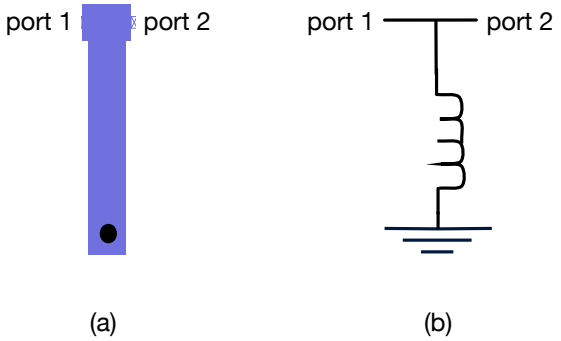

Figure 5.19: The comparison performed to determine the equivalent stub length for a shunt inductor.

2- Add the 0.5 mm sections which are used to connect the series capacitors on both sides of the line, as shown in Fig. 5.19-a.

3- Run the simulations for the phase and amplitude of the transmission coefficient for each of the two networks in Fig. 5.19.

4- Compare the results and tune the length of the stub until it matches that of the lumped element.

Fig. 5.20 shows the layout of the two-cell microstrip resonator. The 0.5 mm gap between the stubs as well as the 0.5 mm extra transmission line sections are selected to match the 0402 footprints of the lumped capacitor. The dimensions of the pad placed at the via termination is selected such that the total length of the transmission line sections used in the first tap is doubled in the second tap.

After that, the board layout is exported from ADS to CST Microwave design tools, where full electromagnetic wave simulation is carried out in order to verify the design. The fabrication of the microstrip circuit and the assembly of the vias should be done carefully, since the frequency response of these resonators is very sensitive to any variations in the shunt inductance even though they operate at low frequencies. Fig.5.21 shows pictures of the fabricated microstrip two-cell and three-cell band-stop resonators. The S-parameters of the two circuits are measured using the Vector Network Analyzer. Fig. 5.22 shows the

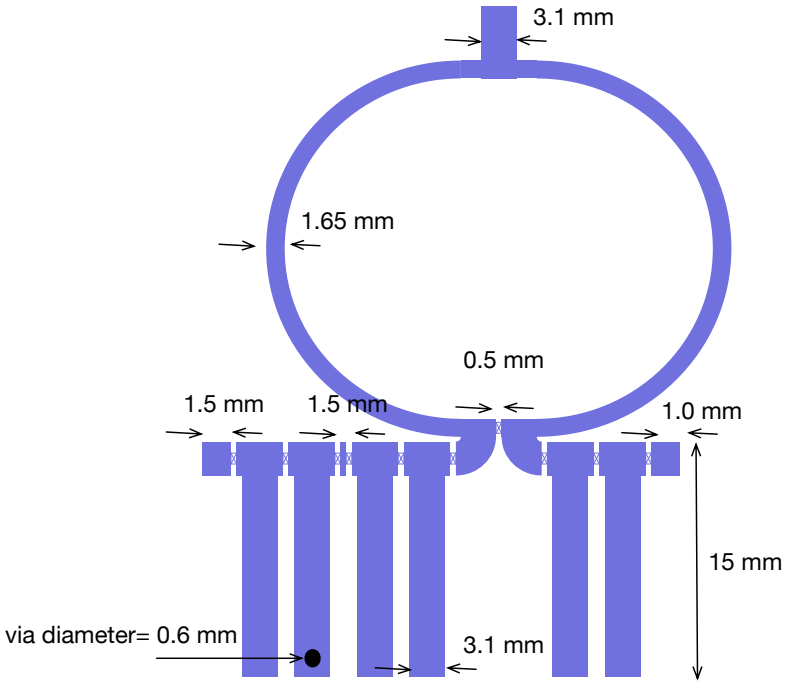

Figure 5.20: The comparison performed to determine the equivalent stub length for a shunt inductor.

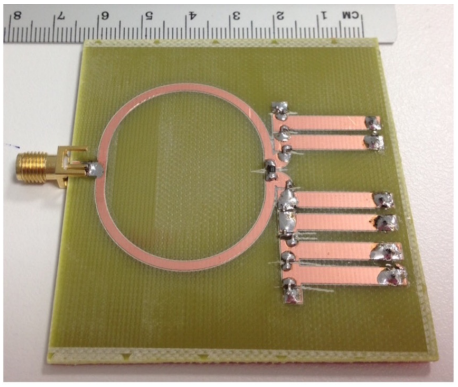

(a) two-cell CRLH band-stop resonator (50 mm x 60 mm)

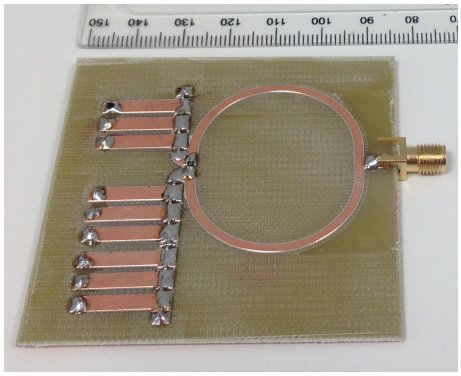

(b) three-cell CRLH band-stop resonator (60 mm x 65 mm)

Figure 5.21: The new fabricated Microstrip CRLH band-stop resonators.

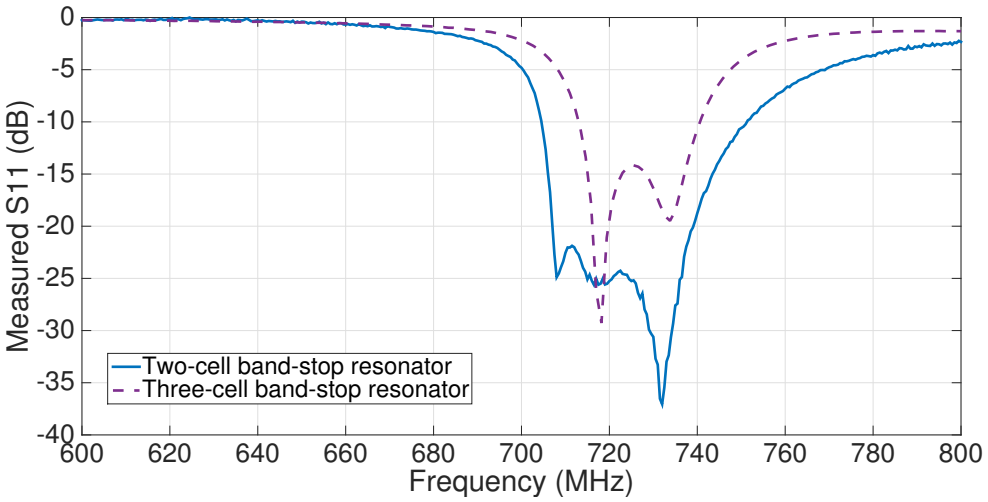

Figure 5.22: The measured input reflection coefficient of the two Microstrip CRLH band-stop resonators fabricated with different number of cells.

measured results, which indicate a good agreement with the circuit simulations conducted above. Measurements of the two-cell resonator show three transmission zeros with more than 25 dB rejection and less than 2 dB insertion loss at 20 MHz away from the receiver band. This points to a 1.14 dB per MHz roll off rate. On the other hand, the measured three-cell resonator shows 30 dB rejection with 1.41 dB per MHz roll off rate.

By comparing the physical dimensions of the new band-stop resonators with those designed in the previous chapter, it is seen that the new design has significantly reduced the size by more than 66%, which can be seen as a big advantage for the new design in this chapter. Unlike the band-stop resonators designed in Chapter IV, the new design is very sensitive to any slight changes in either the series capacitance or shunt inductances. Thus, the microstrip realization, layout preparation and the fabrication process must be all done carefully.

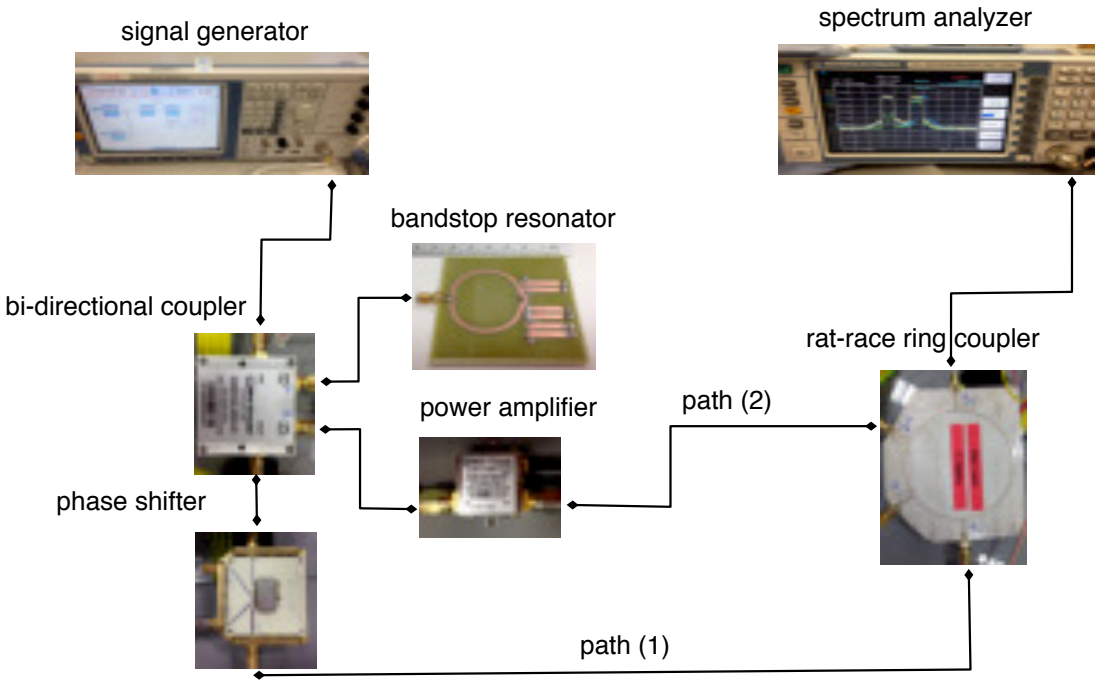

Figure 5.23: The feedforward interference cancellation system setup using the new fabricated CRLH band-stop resonators.

5.5 Interference Cancellation using the New CRLH Band-Stop Resonators

5.5.1 Test Bench Setup

The diagram in Fig. 5.23 shows the test setup used to test the interference cancellation using the new CRLH band-stop resonators. The setup used here is very similar to the test setup presented in the previous chapter, however, the fixed delay component is removed, as it is no longer needed. In the previous setup, the fixed delay component is used to compensate for the constant large group delay introduced by the multi-tap delay resonators, which is not the case anymore with the new CRLH resonators. This can be seen as another big advantage for the new resonator. Here, the feedforward interference cancellation system again consists of two paths: the main path; and the auxiliary path.

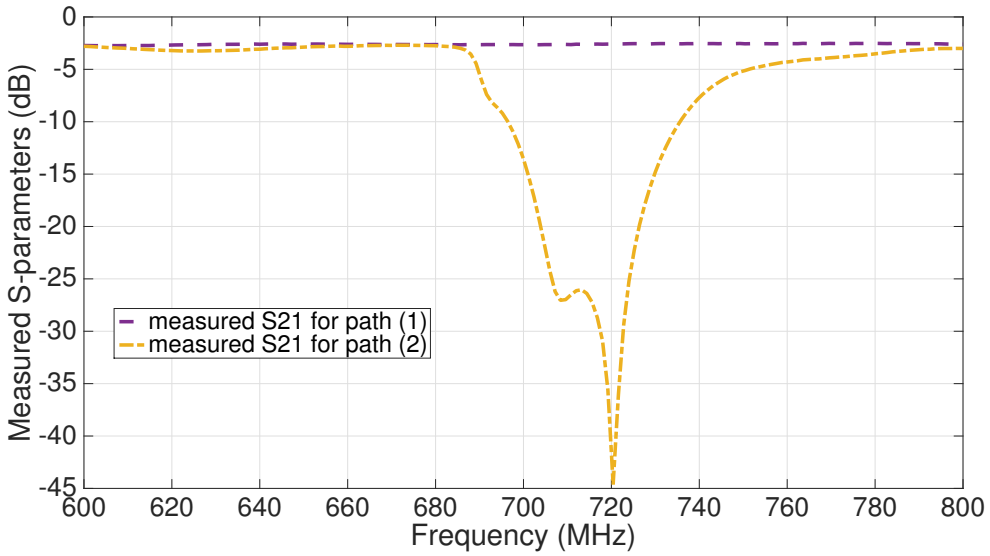

Figure 5.24: The measured transmission S-parameters between the input of the 20 dB bi-directional coupler, and the two inputs of the rat-race ring coupler: path (1); and path (2).

The main path (path 1) represents the output of the phase shifter, while the auxiliary path (path 2) is at the output of the fixed gain amplifier. The phase shifter is adjusted to match the phase of the signals in the two paths at 680 MHz, which is the frequency location of the interferer located at 20 MHz away from the edge of the receiver band (10 MHz bandwidth centered at 698 MHz). Fig. 5.24 shows the measured transmission S-parameters for the two paths, which are measured between the input of the bi-directional coupler and the differential inputs of the Rat-Race Ring coupler.

5.5.2 Test Cases and Results

Two LTE modulated signals are generated to represent both the desired received signal and the interferer. Each of the two signals occupies a bandwidth of 10 MHz. In the first test case, the center frequency of the interferer is set to be located at 20 MHz away from the edge of the desired signal, and the two signals are injected with equal average peak

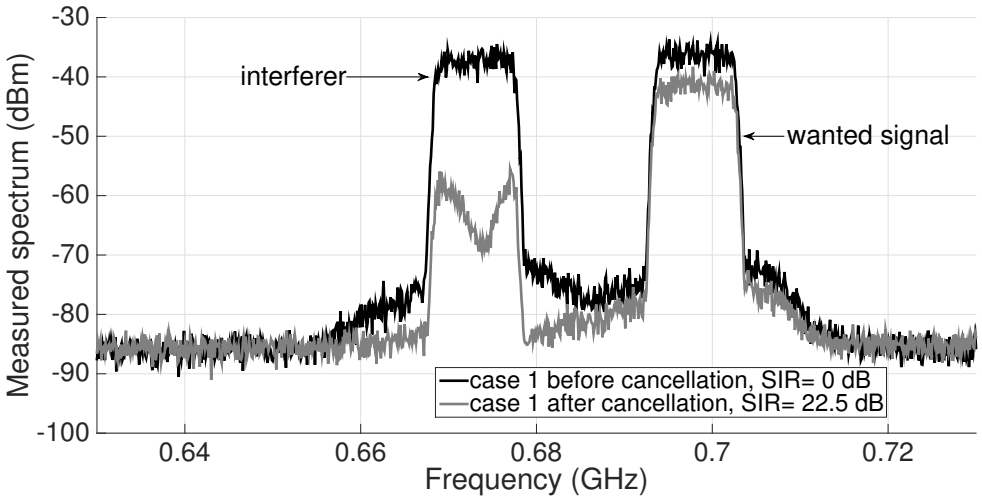

Figure 5.25: Test case 1 power spectrum measurements for the interferer and the wanted received signal before and after interference cancellation.

power ($\simeq$40 dBm). The spectrum is measured once at the output of the signal generator, and another time at the output of the Rat-Race-Ring coupler. Fig. 5.25 shows the measured power spectrum before and after interference cancellation. Measurement results show a maximum of 34 dB cancellation at the center frequency of the interferer, while more than 20 dB are obtained across the whole bandwidth of the interfering signal. Furthermore, the results have shown a reduction in the noise level in the band surrounding the wanted receiver signal. Overall, this cancellation technique has improved the SIR level by 22.5 dB.

In the second test case, the interferer is set to occupy higher power of approximately 30 dB, when compared to the receiver signal level. The measurements are repeated, without adjusting any of the setup components including the phase shifter and amplifier. Fig. 5.26 shows the power spectrum measurements for the signals before and after cancellation, which indicates no degradation in the cancellation performance obtained in the previous case. Leading to the conclusion that, this cancellation technique can handle interferers with any power levels, where no tuning is required for the RF hardware.

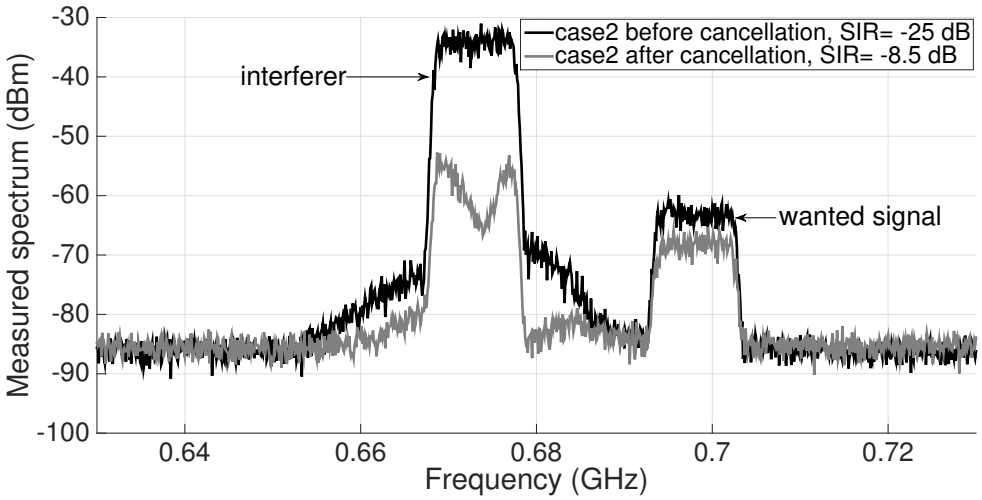

Figure 5.26: Test case 2 power spectrum measurements for the interferer and the wanted received signal before and after interference cancellation.

This can be listed as another advantage over other base band interference cancellation methods.

In test cases 3 and 4, the two signals hold the same power level, but the separation between them is now reduced down to 15 MHz, followed by 10 MHz. This time, the two-cell band-stop resonator is replaced by the three-cell resonator in Fig.5.21 -b. Power spectrum measurements are again recorded for each of the two cases before and after interference cancellation, as shown in Fig. 5.28 and 5.28. Measurement results of the third test case show more than 45 dB cancellation at the center frequency of the interferer, and 25 dB cancellation on the 10 MHz band. In addition, the noise level in the upper side and lower side band of the receiver is reduced by approximately 10 dB and 5 dB, respectively. Measurement results of the fourth test case in Fig. 5.28 show 35 dB cancellation at the center frequency of the interferer and a minimum of 20 dB over the whole band of the signal. Similarly, the noise, which is previously introduced by the interferer on both the upper and lower side bands of the wanted signal, is eliminated. Most importantly, the SIR levels have improved by 26.5 dB and 20.5 dB for the interferers located at 15 and 10

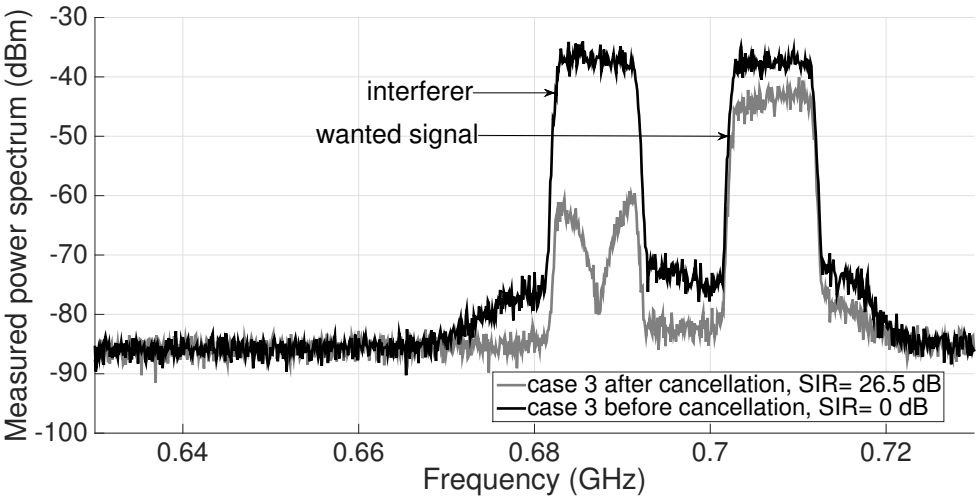

Figure 5.27: Test case 3 power spectrum measurements for the interferer and the desired received signal before and after interference cancellation.

Table 5.2: A performance comparison between the Multi-Tap Delay resonator and the CRLH-TL resonators.

	Multi-Tap Delay Resonator	CRLH_TL Resonator
Board size	135 x 225 mm^2	60 x 65 mm^2
PCB material (ε_r)	Expensive Ceramic material (10)	Standard FR4 (4.3)
Rejection	30 dB	25 dB- 30 dB
Insertion loss	3.9 at 20 MHz offset	2 dB at 20 MHz offset

MHz away from the edge of the wanted signal, respectively.

According to the power spectrum measurements in the four cases, the insertion loss introduced to the receiver signal on average is not more than 3 dB. The same degree of losses is seen in the main path measurements in Fig. 5.24. Knowing that the insertion loss in the Microstrip band-stop resonator itself is less than 1.2 dB only, more than 1.5 dB loss can be further reduced by replacing the voltage controlled phase shifter, which is going to be the topic of the next chapter (Chapter VI).

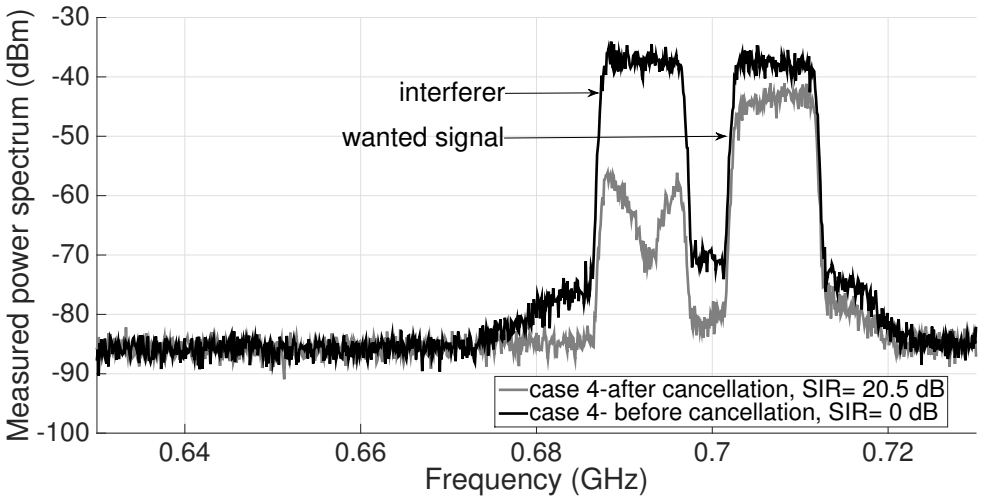

Figure 5.28: Test case 4 power spectrum measurements for the interferer and the desired received signal before and after interference cancellation.

5.6 Conclusion

This chapter introduced a new design for band-stop resonators employing composite right-left-handed transmission line structures. The new resonator represents a more efficient alternative for the Multi-tap delay resonators discussed in the previous chapter. Since it replaces the large meander delay lines with artificial left-handed transmission lines, constructed using a finite number of cells, it offers much smaller circuit dimensions, in addition to less fabrication costs and complexity. Furthermore, the new resonator shows the same frequency selectivity offered by the large delay lines with much lower pass band losses, as the cut off frequency of the band-stop resonator is designed near the Bragg Cutoff of the left hand propagation mode.

5.6.1 Summary of the Results

Two Microstrip CRLH band-stop circuits are designed, fabricated and measured using two-cell and three-cell of lumped capacitors and short circuited stubs.

- Measurements of the two-cell resonator show three transmission zeros with more than 24.8 dB rejection and less than 2.1 dB insertion loss at 20 MHz away from the receiver band. This points to a 1.14 dB per MHz roll off rate.

- Measurements of the three-cell resonator show three transmission zeros with more than 30 dB rejection and less than 1.8 dB insertion loss at 20 MHz away from the receiver band, which indicates more than 1.41 dB per MHz roll off rate.

The feedforward cancellation system is again tested using the new band-stop resonator presented in this chapter. Four test cases are defined where the interferer is located at different locations away from the receiver edge, and at different power levels.

- In the first test case, the interference signal is located at 20 MHz away from the receiver band. And the test results show more than 34 dB rejection with less than 3 dB losses introduced in the band of the wanted signal. Most importantly, the SIR is improved by more than 22.5 dB.

- In the second test case, the power level of the interference signal is increased by 30 dB. Measurements show the same performance is obtained in terms of interference signal rejection and SIR level improvements, which proves that this cancellation technique is able to handle interferers with any power levels with no hardware tuning.

- In the third and the fourth test case, the interference signal is brought closer to the edge of the band. And the test results show more than 45 dB and 35 dB rejection for interferers located at 15 MHz, and 10 MHz away from the receiver edge, respectively. Furthermore, the improvements in the SIR increased to reach 26.5 dB and 20.5 dB for the two cases.

5.6.2 Evaluation of the Results

Table. 5.2 shows a performance comparison between the new band-stop resonator designed in this chapter and the Multi-Tap Delay resonator introduced in Chapter IV.

5.6.3 Limitations

The limitations of the CRLH-TL resonator appear only at high frequency applications (e.g. > 5 GHz), where high frequency lumped capacitors are abandoned. At high frequencies, the wave length becomes shorter than the physical dimensions of the lumped component. This introduces additional phase changes and the lumped circuit model becomes inaccurate. Multilayer PCB technology can be used to implement the high capacitance required for the design of the CRLH signal taps.

The following chapter introduces the design of controlled phase shifters using RF switched MEMS devices. The phase shifters are designed to improve the linearity of the interference cancellation system, which can minimize the level of distortion at the receiver band. Furthermore, it can reduce the losses added by the JSPHS-1000+ voltage control phase shifter.

5.6.4 Contributions

In this chapter, a second design methodology for band-stop resonators is introduced offering many advantages over the design presented in the previous chapter. The new resonators are developed based on a new observation of the behavior of artificial left-handed transmission lines. This observation is carefully analyzed using circuit simulations. It is also proven mathematically using the transmission line equivalent circuit of T networks. The author believes that this new design is based on a simple but very interesting and novel idea. The new design has dramatically reduced the circuit size of the resonator used in the previous chapter by more than 66 %, and the authors believed that the size

can be further reduced after eliminating the matching sections in the power dividers. The new resonators have shown a very high roll-off rate that enables the separation of two close wide band signals. The resonators are implemented, tested and employed in the interference cancellation test bench. The test results have shown successful cancellation for interferers located at 20, 15 and 10 MHz. It is believed that by increasing the number of cells in the design of these resonators, interference signals at even smaller frequency offsets can be handled.

Chapter 6

MEMS Phase Shifters for High Accuracy Signal Cancellation

6.1 Introduction

Phase linearity is a critical parameter, as well as a major challenge, in the design of microwave phase shifters. In this thesis, controlled phase shifters are required for matching the RF signals in both the main and the auxiliary paths of the feedforward interference cancellation system. For successful interference cancellation, the phase shifters must be characterized by low frequency dispersion on both the phase and the amplitude. The frequency dispersion is controlled by the phase linearity characteristic of the phase shifter. Passive phase shifters tend to have a substantially higher phase linearity when compared to active devices. In this chapter, a new passive switched delay line phase shifter is designed to replace the JSPHS-1000+ active phase shifter, used in the feedforward interference cancellation system in the previous chapters. The objective of the new design is to improve the phase and amplitude deviation to reach a maximum of 1^o and 0.1 dB, respectively over 50-100 MHz frequency bandwidth.

The new phase shifter is designed using RF micro-electromechanical systems (MEMS)

switches. RF MEMS switches have been employed as an alternative technology for PIN diodes and FET transistors in many wide band applications, for offering a higher performance [64].

RF MEMS devices with integrated switching driver are selected for their fast switching response, low losses and many other advantages. Section 6.2 presents the characteristics and advantages of the RF MEMS device used in this chapter. Section 6.3 studies the phase linearity of different microwave structures that can be used for constructing the RF interface of the MEMS device as well as the meander delay lines of the phase states. Section 6.4 studies and compares two different topologies for building the phase shifter circuit, which are known as “Reflective” and “Non-Reflective”. Section 6.5 presents the design procedures of a small-step and a large-step phase shifter, which are designed using the selected microwave structure for the device integration from Section 6.3 and the selected topology from Section 6.4. In addition, full electromagnetic simulation are applied on the two phase shifters. Section 6.6 shows the fabrication and measurements of all the performance parameters including the phase curves, the amplitude losses, the RMS phase and amplitude deviation. Furthermore, a linearity test is conducted, followed by a performance comparison with OMRON Phase Shifters.

6.2 Characterization of the ADG MEMS Device

A new MEMS switch has been designed by Analog Devices Inc. offering many advantages over other MEMS devices [65]. It is a very low loss packaged MEMS switch which operates over a very wide band starting from low frequencies near DC up to 14 GHz. ADG1904 is the part number for the single-pole-four-throw (SP4T) device used in this work, thus it is referred to as ADG MEMS device. This device is enclosed in a 24-lead 5 mm x 4 mm x 0.95 mm package whose pin configuration is shown in Fig. 6.1. It consists of four RF input ports, which are RF1, RF2, RF3, RF4, and one RF common output port,

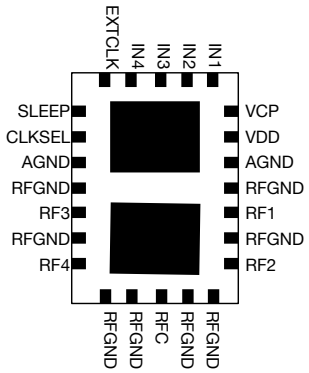

Figure 6.1: The land pattern for SP4T ADG MEMS Switch (ADG1904)

whose pin is referred to as RFC. Each RF port uses three pins, a signal pin surrounded by two ground pins (RFGND). All the RF ports are matched to a system impedance of 50 Ω, which facilitate the integration of these devices. The switching functions are controlled via four digital inputs (IN1, IN2, IN3 and IN4), whose ON and OFF voltage states are equal to 3 V and 0 V, respectively. Only one digital input can be turned on at a time since it controls the state of the connection between one of the RF inputs and the RF common port (RFC). For example, RF1 port is activated when IN1 is turned ON and all other digital inputs are OFF.

Like other metal-based devices, a high driving voltage of about 80 V is required to actuate the device, however the ADG MEMS device here needs a 3 V signal only, since it incorporates a boost circuitry generating the 80 V via a charge pump capacitor at the VCP pin. A 3 V supply is also connected to the VDD pin. A schematic for a typical operating circuit for the device is shown in Fig. 6.2.

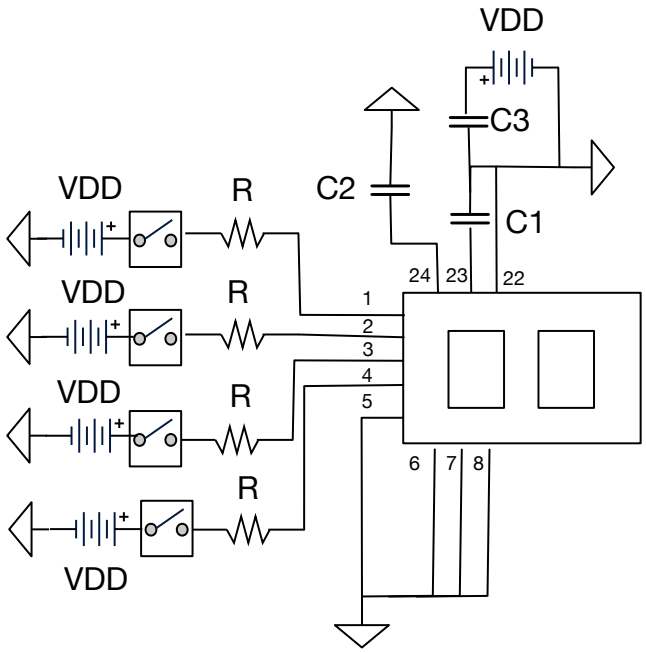

Figure 6.2: A schematic for the DC connections required for operating the ADG MEMS switching device.

The ADG MEMS device is also characterized by a very low ohmic resistance (=1 Ω) resulting in a maximum insertion loss of about 3 dB at 11 GHz, respectively. It also offers more than 25 dB isolation between the RF ports and less than -35 dB crosstalk. These data are collected using the device evaluation board in Fig. 6.3, which consists of three parts: a reference line; the DC control circuit; and the RF inputs/outputs transmission lines. The reference line is used to characterize both the amplitude and phase response of the device. This can be achieved by comparing the measurements of the four switching states to the reference line, whose length is set to be equal to the combined length of the output and input RF transmission lines/tracks.

The S-parameters of the five RF ports are measured to determine the phase shifts encountered by the signal at each of the four switching states. The phase shifts are later used in the design of the phase shifter to compensate for having more devices in some

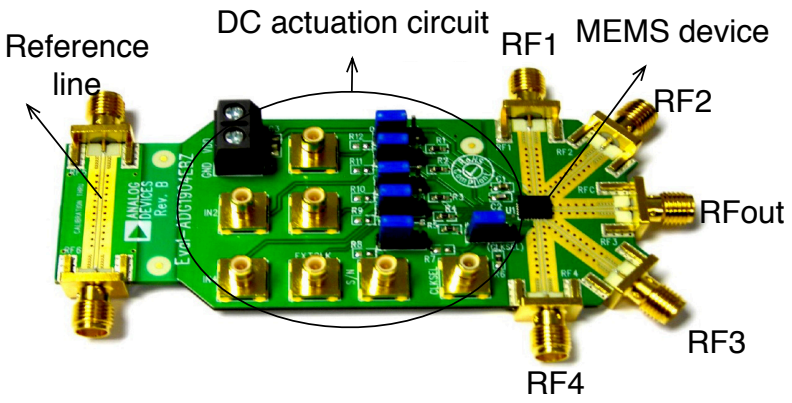

Figure 6.3: An evaluation board for one ADG MEMS device.

Switching state	RF1	RF2	RF3	RF4
S21 (dB)	-0.2	-0.14	-0.21	-0.14
S11 (dB)	-29.8	-28.3	-28.8	-30.5
$\angle$S21 (deg)	-18.8^o	-18^o	-18.2^o	-18.7^o

Table 6.1: The measured S-parameters for the ADG MEMS device

phase state when compared to others. Other parameters provide a rough estimate for the amplitude losses of the phase shifter to be designed. Table. 6.1 lists the measured S-parameters of the device at 900 MHz. In addition, the measurements show greater than 25 dB isolation between the RF ports and < -35 dB crosstalk.

Furthermore, ADG features high power handling capabilities which makes this device suitable for cellular applications. A linearity test was conducted and resulted in a minimum IP3 of 67 dBm with a maximum input power of 36 dBm. This device is also characterized by a fast switching response (5 microsecond) as well as high reliability with a typical life time of 10 billion cycles [65].

Laminate Type	Rogers 6010	Rogers 4003
Permittivity (ε_r)	10.7	3.55
Thickness	1.9 mm	0.2 mm
Effective Permittivity (ε_{eff})	5.8	2.7
Dielectric loss (α_d)	1.4 dB/m	0.45 dB/m

Table 6.2: The specifications of the two substrates selected to design the RF interface of the ADG MEMS devices.

6.3 ADG MEMS RF Interface and Meander Delay Lines

The ADG MEMS device has a large number of pins underneath the package which need to be connected to several transmission lines. Thus care has to be taken when integrating the device on a printed circuit board. A coplanar waveguide transmission (CPW) line type is selected for the design of the RF interface of the device as it matches the arrangement of the RF pins, which requires two RF ground connections surrounding the RF signal. Two different substrates can be used to realize a 50 Ω impedance CPW line with the dimensions matching the device pin separation. Table 6.2 shows the specifications of the two substrates: Rogers 6010; and Rogers 4003.

There are different CPW structures that can be used to construct the RF tracks as well as the meander delay lines for the ADG MEMS-based phase shifter. Here, three different prototypes are presented, studied and their phase linearity characteristic evaluated by applying full wave simulations. The first prototype uses conventional CPW lines at the interface of the device and microstrip transmission lines for the meander delays. The second prototype uses conventional CPW for both, while the third prototype uses grounded coplanar waveguide (GCPW) structures, as shown in Fig. 6.4 and 6.5.

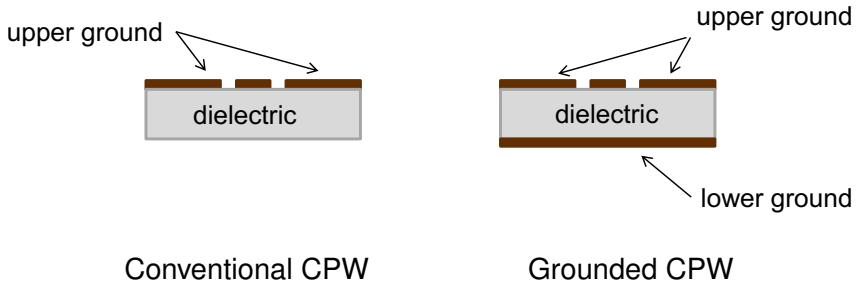

Figure 6.4: A side view for the structure of conventional and grounded CPW transmission lines.

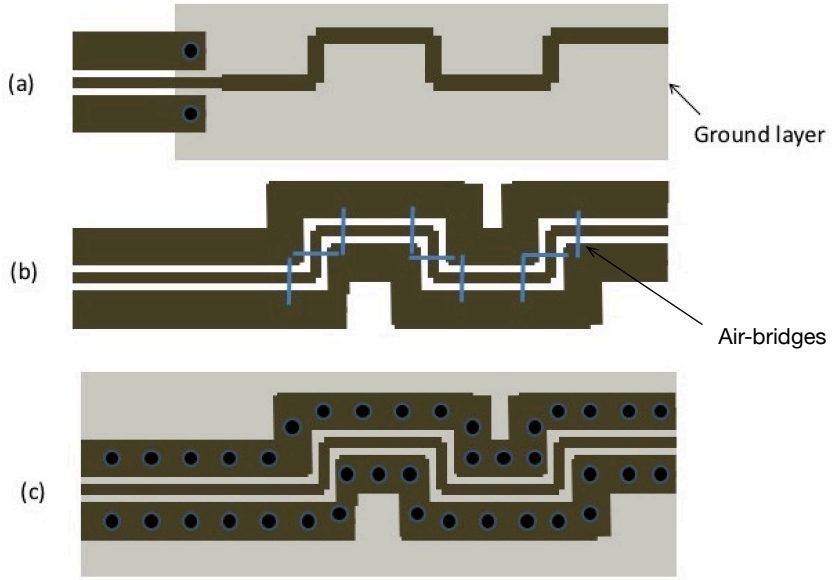

Figure 6.5: The structure for the RF tracks together with the meander delay lines. a) prototype 1: micro strip meander delay lines, b) prototype 2: conventional coplanar waveguide with airbridges, c) prototype 3: grounded coplanar waveguide with vias.

6.3.1 Prototype 1: Microstrip Meander Delay Lines

Meander delay lines are commonly designed using Microstrip line (MSL) structures for offering higher robustness to the excitation of undesired parasitic modes resulting from line bending. Another advantage, meander MSL usually occupy less space when compared

to other microwave structures. In this prototype, a transition is required to connect the MSL meander lines to the CPW lines at the interface of the switch. As introduced earlier by Chen et. al. [66], CPW to MSL transitions can be designed by extending the lower ground of the MSL line underneath the CPW line, and placing two solid vias to connect the upper ground of the CPW lines with the lower ground of the MSL line. CPW to MSL transition proved to deliver a good wide-band performance with low insertion and return losses [66]. However, the effect of CPW to MSL transition on phase linearity was never mentioned. For the consideration of this work, poor phase linearity can hugely degrade the signal cancellation performance causing large deviations in the group delay. Fig. 6.6 shows the structure of the device interface with the CPW to MSL transition. High permittivity Rogers 6010 material is used in order to realize a 50 Ω conventional CPW whose dimensions matches those described in the footprints of the ADG MEMS device. The phase linearity of this prototype is tested in Section 6.3.4.

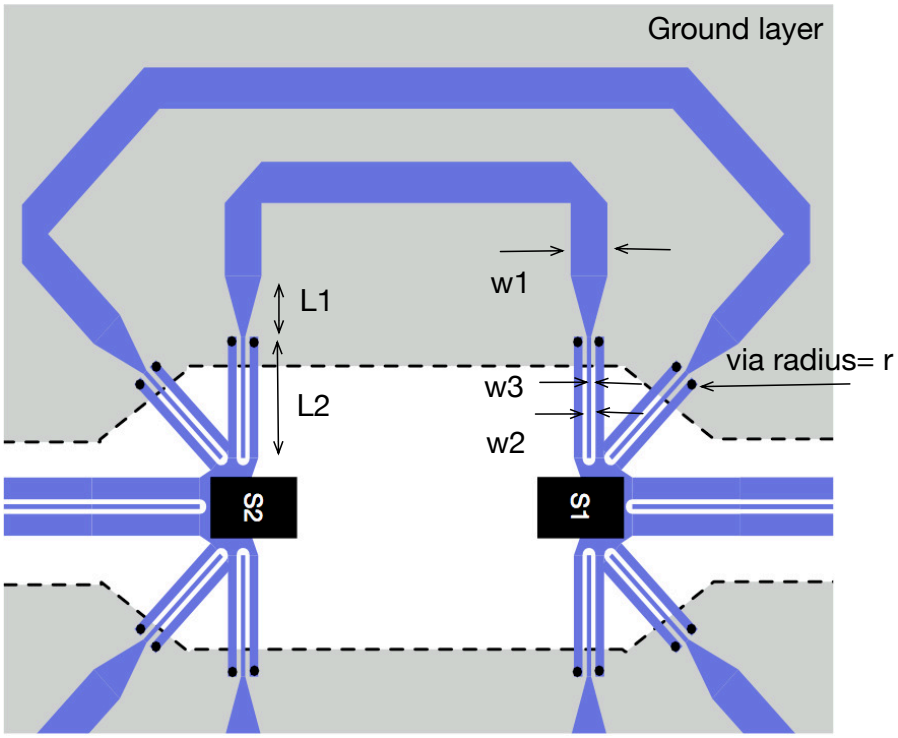

w1	w2	w3	L1	L2	r
1.7	0.8	0.2	2.5	5.0	0.2

Figure 6.6: The structure for the RF tracks together with the meander delay lines in prototype 1 using the CPW to MSL transition, whose dimensions are all listed in mm.

6.3.2 Prototype 2: Conventional Coplanar Waveguide with AirBridges

The second prototype uses conventional CPW lines to construct both the interface of the device and the meander delay lines. In this case, no transitions are required which is an advantage over the first prototype.

Since more than one switches is needed and the integration of chips requires a large number of transmission lines with lots of bending, discontinuities of the center conductor and asymmetries between the two finite ground planes. Therefore, the effects of the CPW higher modes should be considered. For example, consider a 90 degree cpw, the wave propagating in the outer slot will experience a phase shift for taking a longer path

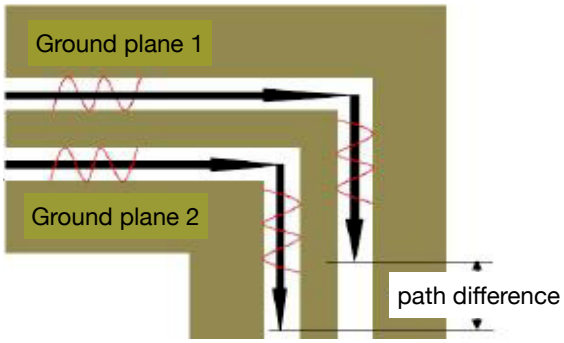

Figure 6.7: Un-equal potential in conventional coplanar waveguide 90 degree bend.

compared to the one in the inner slot as shown in Fig. 6.7. This extra phase difference leads to having a potential difference between the two ground planes, thus the slot line mode is excited and coupled to the cpw mode. Also, if there is asymmetry between the two nite ground planes of a CPW line, further modes can be excited which are the c-mode (cpline-like mode) and pi mode (slotline-like mode). All these modes will result in an undesired resonance in the response of the whole circuit [67].

An air-bridge is a wire connection which is used to connect the two upper ground planes of CPW lines on the top of the substrate (in the air). Air-bridges are used in CPW discontinuities to maintain a zero potential difference between the ground planes. At high frequency, the potential of the ground planes varies through the line and connecting the two grounds at a certain point in the line with a small bonding wire will equalize the potential between the ground planes only at this point. Thus its required to place the air bridges at every bending or discontinuity in the line. If there is an asymmetry between the two finite ground planes, these unequal potentials will persist through the whole line. In this case, more bonding wires need to be placed or one large air bridge to cover the whole line. Small air bridges placed with regular intervals can result in a standing wave mode between each two corresponding air bridges which degrades the performance, while using one large air bridge will result in increasing the shunt capacitance which

again leads to undesired reflections of the transmitted signal increasing the transmission losses. If a large air bridge is required, the capacitance of the air bridges must be reduced and this can be done by adjusting the height of the bridge. A very high air bridge will add a lower shunt capacitance to the line but more modes are also excited at higher frequencies causing more resonances. The height has to be optimized for reducing the parasitic losses without exciting higher modes. Wire airbridges are designed such that the parasitic capacitances added by the wires are minimum. In this design, copper wire airbridges with 0.1 mm radius are placed at 2 mm above the surface of the board, and Fig. 6.8 shows the structure of the device interface with the meander lines used in this prototype. The phase linearity of this prototype is tested and compared to other solutions in Section 6.3.4.

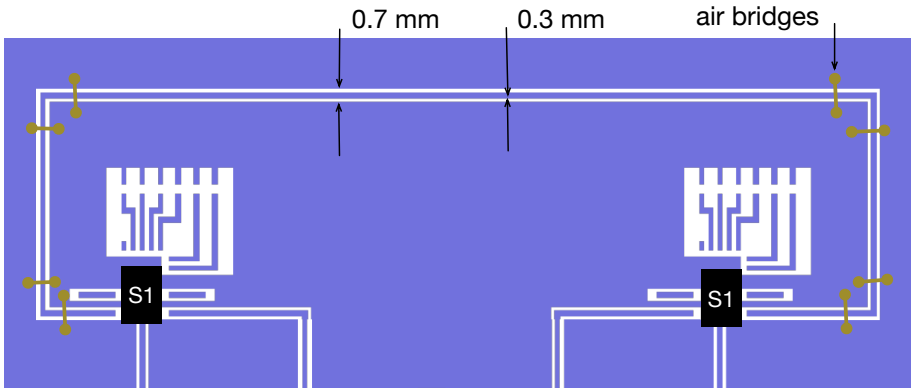

Figure 6.8: The structure for the RF tracks together with the meander delay lines in prototype 2.

6.3.3 Prototype 3: Grounded Coplanar Waveguide with Vias

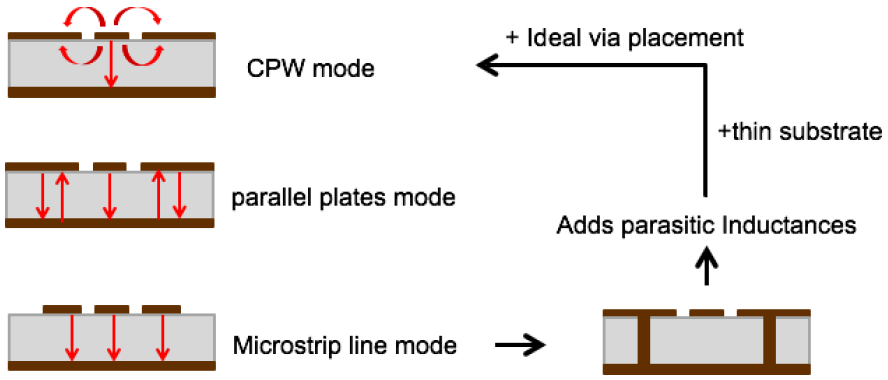

Figure 6.9: Propagating modes in grounded coplanar waveguide structures (GCPW).

In the third prototype, finite grounded coplanar waveguides (GCPW) are used instead of conventional CPW. GCPW lines also suffer from undesired propagating higher modes for having multiple ground layers. Unlike CPW, the higher modes in GCPW are not only generated at the line bends. In fact, unequal potential between the upper and lower ground layers can occur at any part of the line due to the excitation of either parallel plates mode or micro strip line mode as shown in Fig. 6.9 [68]. As a result, solid vias need to be inserted along the line connecting both left and right upper ground planes to the common ground under the substrate. The separation between the vias should not exceed one tenth of the guided wavelength at the highest frequency of operation. Thin layer substrates are recommended to reduce the parasitic inductance of the vias and therefore Rogers 4003 makes a better candidate. Multilayer substrates can further assist the vias to suppress the parallel plate modes.

6.3.4 Phase Linearity Test for the three Prototypes

Three different meander delay lines are designed with equal electrical length to provide a fixed group delay of 600 ps. The first two lines are constructed by applying the structures

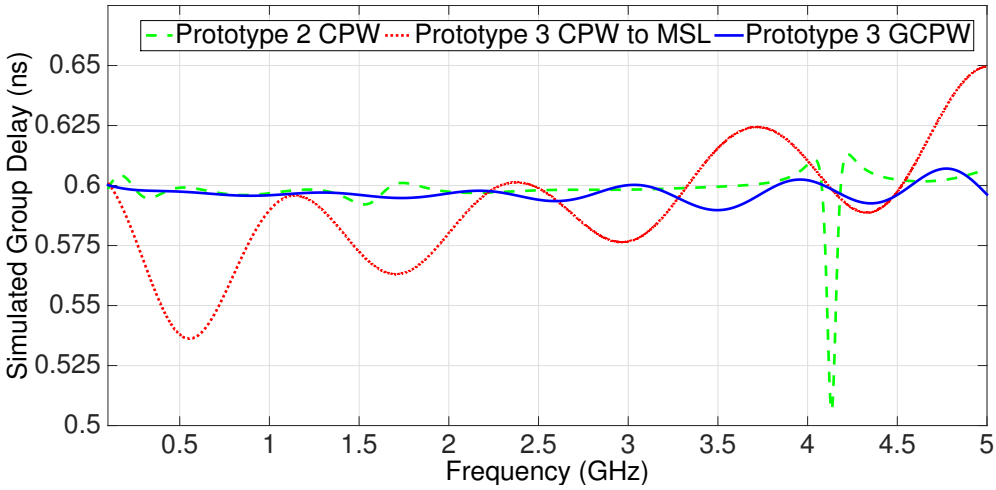

Figure 6.10: A comparison between the simulated group delays for the three proposed prototypes

in Prototype 1 and 2 using a single layer substrate of Rogers6010. The third line uses the GCPW prototype 3 with a stacked substrate layers of Rogers4003 and standard FR4 (thickness= 0.94 mm). The three lines are simulated using the transient solver in CST Microwave Studio. Fig. 6.10 shows the simulation results for the group delay, which indicates a minimum delay deviations ($\tau_{deviation}$) of only ±4 ps (±1%) for the GCPW prototype, while a maximum deviation in the group delay of ±63 ps (±10.5%) occurs in Prototype 1 over the same frequency bandwidth. Table. 6.3 shows a comparison between the three prototypes including a summary of the simulation results up to 2.7 GHz. Prototype 3 has shown the minimum group delay deviation which is only 0.67% when compared to the other two designs. This indicates that finite grounded CPW structures provide higher phase linearity for the propagating fields and makes a better candidate for constructing the phase shifter circuits.

Table 6.3: A comparison between the simulation results of the three proposed prototypes

	Prototype1	Prototype2	Prototype3
ADG MEMS tracks	CPW	CPW	GCPW
meander lines	MSL	CPW+ airbridges	GCPW+ vias
substrate	Single subs.	Single subs.	Multilayer
insertion loss	<0.8 dB	< 1 dB	< 0.28 dB
$\tau_{deviation}$	$\pm$63 ps (10%)	$\pm$7 ps (1.16%)	$\pm$4 ps (0.67%)

6.4 Reflective and Non-Reflective ADG MEMS Phase Shifter Topologies

As mentioned earlier, the structure of the phase shifter presented in this chapter is based on true delay lines. The ADG MEMS device is used to switch between delay lines with different lengths creating different paths for the RF signal and thus the phase is adjusted based on the propagation path length. Two different topologies can be used to switch between these lines, which are referred to as “Reflective” and “Non-Reflective”. Fig. 6.11 and Fig. 6.12 show examples of the two topologies. In Reflective topology, the RF input ports of each switch are connected to short circuited stubs with different lengths. Stubs can always offer a smaller size for realizing large delays or phase shifts, which is a big advantage for Reflective topology over Non-Reflective. The design of short and open GCPW stubs was introduced earlier with optimized insertion and return loss characteristics over a wide range of frequencies in [69]. However, fabrication tolerances in the practical realization of these structures using printed circuit boards might still alter their performance. Hence, a mathematical analysis is conducted to study the effect of impedance mismatches due to fabrication tolerances on the phase linearity of GCPW stubs and compare them to GCPW loaded transmission lines.

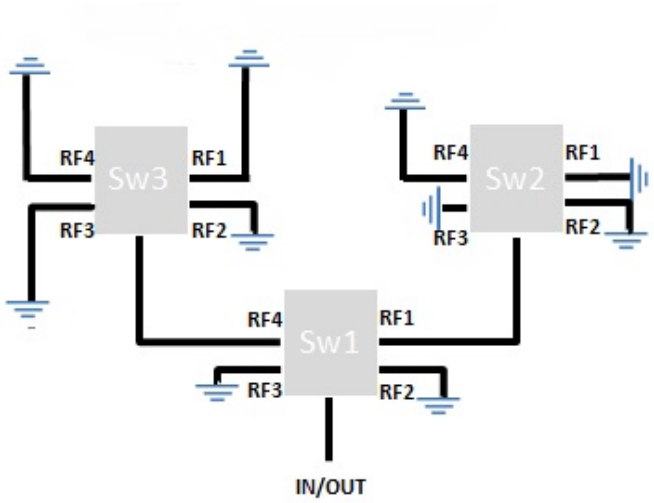

Figure 6.11: An example of Reflective topology using 3 ADG MEMS switches to create 10 phase states.

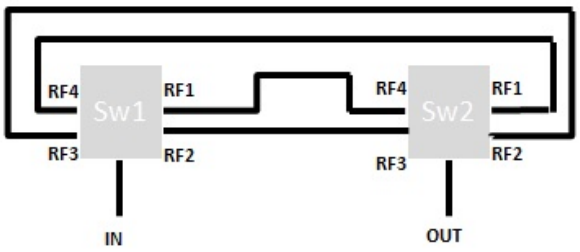

Figure 6.12: An example of Reflective topology using 2 ADG MEMS switches to create 4 phase states.

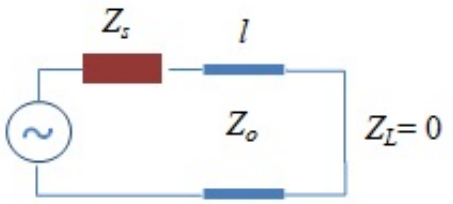

(a)

(b)

Figure 6.13: a: short circuited stub, b: loaded transmission line.

6.4.1 Mathematical Analysis of Phase Sensitivity of Reflective and Non Reflective Topologies

Consider a lossless transmission line terminated by a short circuit load ($Z_L = 0$) as shown in Fig. 6.13-a. The input impedance and reflection coefficient seen from the source can be expressed using Eqn. 6.1 and Eqn. 6.2, respectively, based on the transmission line theory in [70]. In this case, the phase of the reflection coefficient is characterized by a perfect linear response at any frequency as seen in Eqn. 6.3. If the impedance of the line is slightly shifted from the source impedance such that $\frac{Z_o}{Z_s} = \delta$, the magnitude and the phase of the reflection coefficient can be modified as in Eqn. 6.4 and Eqn. 6.5, respectively. By comparing Eqn. 6.3 and Eqn. 6.5 the condition of obtaining a linear phase response in a short loaded stub is $\delta^2 = 1$. Similarly, this condition also applies if the transmission line is terminated by an open circuit.

$$Z_{in} = jZ_o tan(\beta l) \tag{6.1}$$

$$\Gamma = \frac{tan^2(\beta l) - 1 + 2jtan(\beta l)}{1 + tan^2(\beta l)} \tag{6.2}$$

$$\Gamma_{ph} = tan^{-1}(\frac{2sin(\beta l)cos(\beta l)}{sin^2(\beta l) - cos^2(\beta l)}) = -2\beta l \tag{6.3}$$

$$\Gamma = \frac{Z_{o1}^2 tan^2(\beta l) - Z_o^2 + 2jZ_oZ_{o1}tan(\beta l)}{Z_o^2 + Z_{o1}^2 tan^2(\beta l)} \tag{6.4}$$

$$\Gamma_{ph} = tan^{-1}(\frac{2\delta sin(\beta l)cos(\beta l)}{\delta^2 sin^2(\beta l) - cos^2(\beta l)}) \tag{6.5}$$

where β is the propagation constant and l is the length of the transmission line.

Now, consider a lossless transmission line terminated with a load impedance Z_L as shown in Fig. 6.13b. If Z_L is perfectly matched to the impedance of the source (Z_s), while the line impedance (Z_o) is slightly shifted with the same impedance mismatch δ, then the magnitude and phase of the transmission coefficient (T_{21}) from the source to the load can be expressed using Eqn. 6.6 and Eqn. 6.7, respectively. In this case, a linear phase response for the wave propagating from the source to the load is only obtained under the condition of $\frac{2}{\delta + \frac{1}{\delta}} = 1$, as seen in Eqn. 6.8.

$$T = \frac{(Z_o^2 + Z_s^2)tan^2(\beta l) + 2jZ_sZ_otan(\beta l)}{\frac{1}{(Z_o^2 - Z_s^2)}(4Z_o^2Z_s^2 - (Z_o^2 + Z_s^2)^2 tan^2(\beta l))} \tag{6.6}$$

$$T_{ph} = tan^{-1}(\frac{2Z_sZ_o}{(Z_o^2 + Z_s^2)tan(\beta l)}) \tag{6.7}$$

$$T_{ph} = tan^{-1}(\frac{2cot(\beta l)}{\delta + \frac{1}{\delta}}) \tag{6.8}$$

By comparing the phase linearity conditions of the two different scenarios for the same impedance mismatch δ, it can be seen that the value of δ will always have a larger effect

on short and open terminated stubs when compared to the loaded transmission lines. For example, a 5 % impedance mismatch (δ= 0.95) implies a value of $\delta^2 = 0.9025$ and $\frac{2}{\delta+\frac{1}{\delta}} = 0.9986$ for the short/open stubs and loaded lines, respectively. This makes the phase linearity of stubs much more sensitive to impedance mismatches when compared to loaded lines.

6.4.2 Verification Test

To verify the results obtained by the above mathematical analysis, a GCPW shunt stub and transmission line are designed with the dimensions matching a 50Ω system impedance. They use a conducting material of annealed copper (conductivity= 5.813x E7 S/m, surface roughness= 3.4μm, and thickness= 33.02μm), and Rogers 4003 substrate ($\varepsilon_r = 3.55$, loss tangent= 0.0027, and thickness= 0.203 mm). The width of the signal line is 0.42 mm, and the gap between the upper ground and the signal line is only 0.3mm. The lengths are designed such that both lines deliver the same group delay with 400 ps (τ) over a frequency range from 0.1 GHz up to 5 GHz. The length (l) of the transmission line is calculated using Eqn. 6.9.

$$l = v_{phase} \cdot \tau = c\frac{\tau}{\sqrt{\varepsilon_{eff}}} \tag{6.9}$$

where v_{ph} is the phase velocity of the corresponding medium and $\varepsilon_{eff} = 2.726$ is the effective dielectric constant [70].

Consider a 72.6 mm long GCPW transmission line whose signal line width is accompanied by a small error (w= 0.42$\pm\Delta$mm), where Δ can be used as a reference for possible fabrication tolerances. Applying the transmission line circuit model simulations in ADS using different values of Δ results in slightly different group delays curves shown in Fig. 6.14, which indicates a maximum time deviation of ± 0.4 ps and ± 3 ps for 1.6% and 8.5% impedance mismatch (δ= 0.984 and δ=0.915), respectively. Repeating the simulations

for a 36.3 mm GCPW short stub results in a larger time deviation of ± 6 ps and ± 29.5 ps for the same impedance mismatch values, as seen in Fig. 6.15.

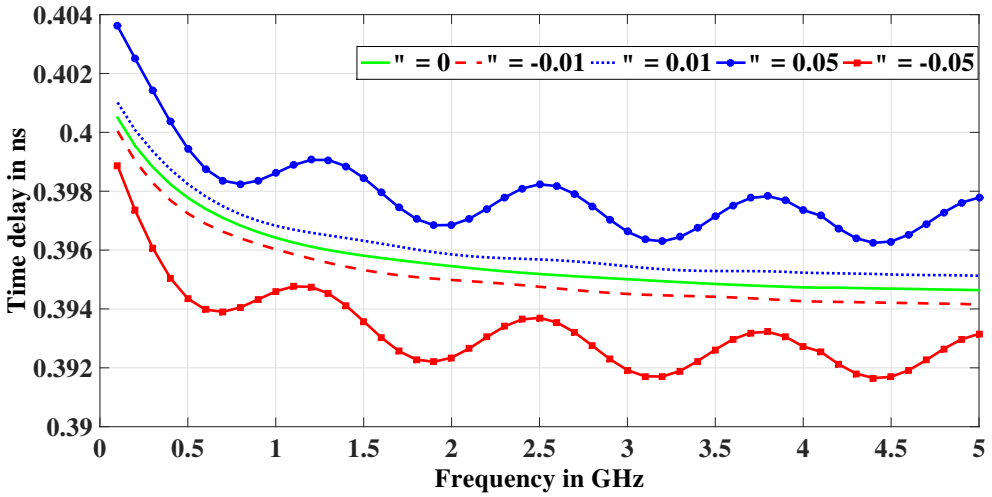

Figure 6.14: Simulated time delay of GCPW transmission line at different line width

Without any impedance mismatches (Δ= 0), fixed dimensions are set for the two lines and electromagnetic simulations are applied using discrete port excitation as seen in Fig. 6.16. Fig. 6.17 shows a comparison between the simulated group delay for the wave reflected from the short stub together with the delay of the wave transmitted through the line. The results indicates a larger time deviation for the stub reaching ± 15 ps at 2 GHz, and is further increased to ± 30 ps at 4.5 GHz, given that the dimensions of both structures are identical.

6.5 ADG MEMS Phase Shifters Design and Simulations

As mentioned earlier, phase linearity is a critical parameter in the design of phase shifters, since it improves the accuracy of signal cancellation. Based on the studies conducted in the previous sections, a Non-Reflective topology is selected for the design of the phase shifters using the GCPW structures (Prototype 3) for showing a higher phase linearity.

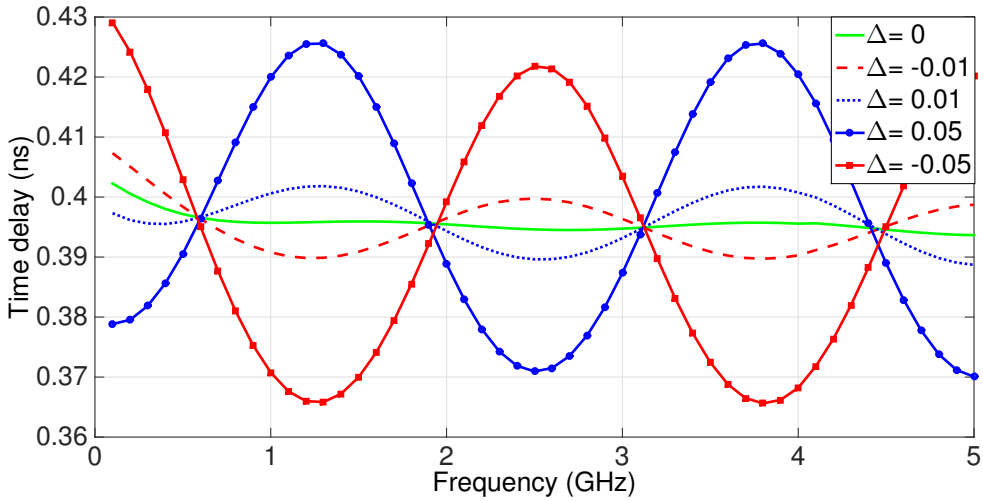

Figure 6.15: Simulated time delay of GCPW short stub at different line width

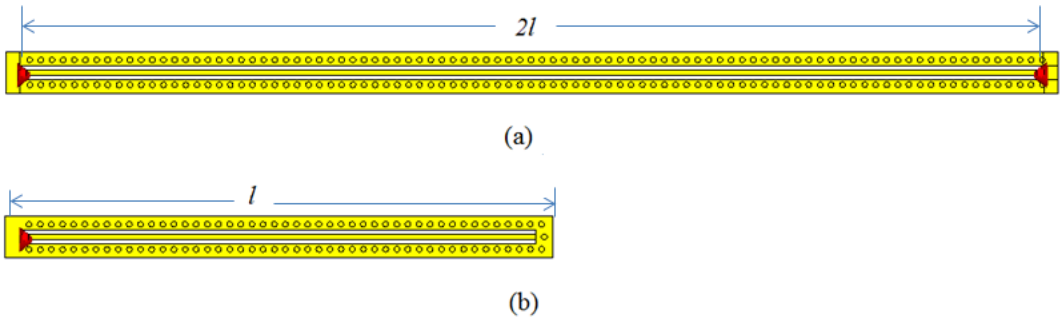

Figure 6.16: The electromagnetic simulation setup for a 400 ps transmission line and short circuited stub.

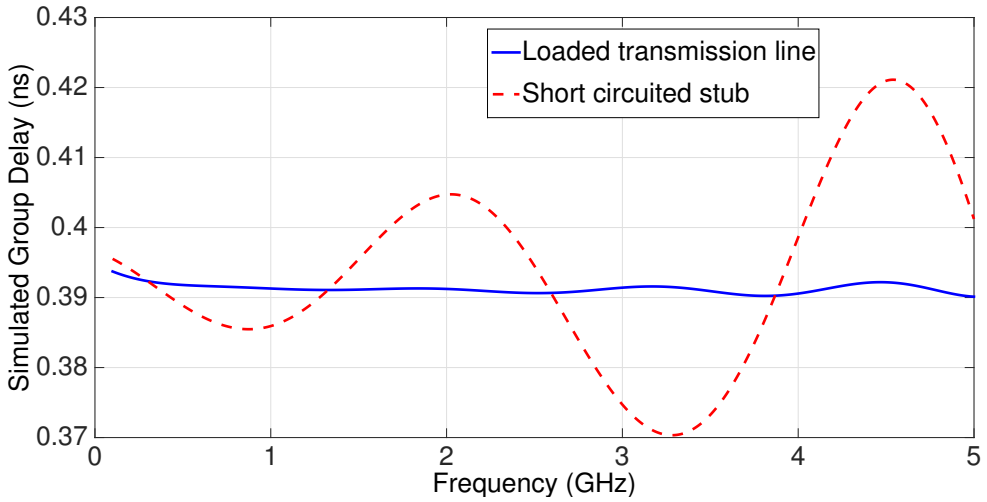

Figure 6.17: Simulated time delay of GCPW short stub and transmission line using microwave simulation tools.

The ADG MEMS switches are designed to handle high power levels as discussed in [65]. Accordingly, the phase shifter circuit layout is designed using four layers of copper to increase the available area for heat dissipation from the device. The layers are connected using multiple vias placed every 0.2 mm reducing the thermal resistance from the IC to the dissipating planes. Rogers 4000 C series material is also selected to have a lower dielectric constant together with a high thermal conductivity (0.71 W/m/K).

Two phase shifter circuits are designed: a small step; and a large step phase shifter. Fig. 6.18 shows the structure of the stacked substrates used as well as the dimensions of the GCPW lines. The circuits are designed based on switched group delay lines, therefore the switching states can be expressed either in time delays (ns) or in degrees at a certain frequency point.

6.5.1 ADG MEMS Small Step Phase Shifter

A small step phase shifter is required to increase the accuracy of signal cancellation which highly depends on phase matching. A minimum phase step of $\Delta = 3.24^o$ at 900

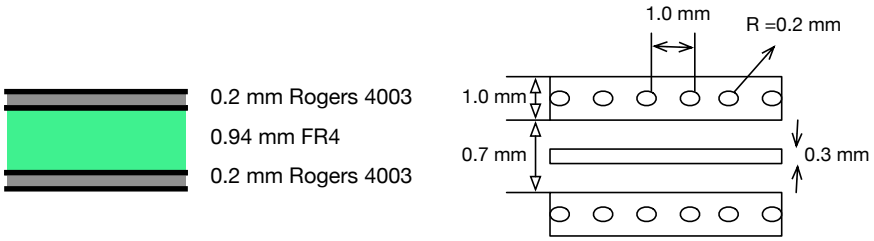

Figure 6.18: The layout of the GCPW 50Ω line used to integrate the ADG MEMS device.

MHz (group delay= 10 ps) is obtained by constructing two GCPW connections (Tr1 and Tr2) between two ADG MEMS devices, such that the difference in the length of the two lines is minimum, as shown in Fig. 6.19. The dimensions of the inner signal line and the gap of the GCPW lines are tapered at the interface of the device in order to improve the isolation between the two ports. The tapering is performed on the signal line width to reduce it from 0.38 mm down to 0.3 mm. Also, the gap width is reduced from 0.3 mm to 0.2 mm, in order to match the exact dimensions of the pins of the ADG MEMS device. The tapering is done carefully, and the length of the tapered line is optimized to avoid impedance mismatches.

More phase states are obtained by switching between Tr1 to Tr6, whose lengths are calculated to obtain continuous phase steps of Δ. This is achieved using six ADG MEMS devices, which are connected according to the configuration illustrated in Fig.6.20. Tr1 is the phase reference line with 0^o . Tr2, Tr5 and Tr6 are designed to add a phase shift of Δ, 2Δ and 4Δ, respectively. The length of Tr3 is equal to twice the length of Tr4 plus “m”, where m is the length required to compensate for the phase shift through devices no. 5 and 6. The length of Tr4 can take any value, here, it is selected to be 22 mm, so that there is enough space for the DC wiring of the devices. Six phase states are thus formed by combining the labeled tracks in Fig. 6.20-a as follows: Tr1, Tr3; Tr2, Tr3; Tr1, Tr4, Tr5; T2, Tr4, Tr5; Tr1, Tr4, Tr6 ; and Tr2, Tr4, Tr6.

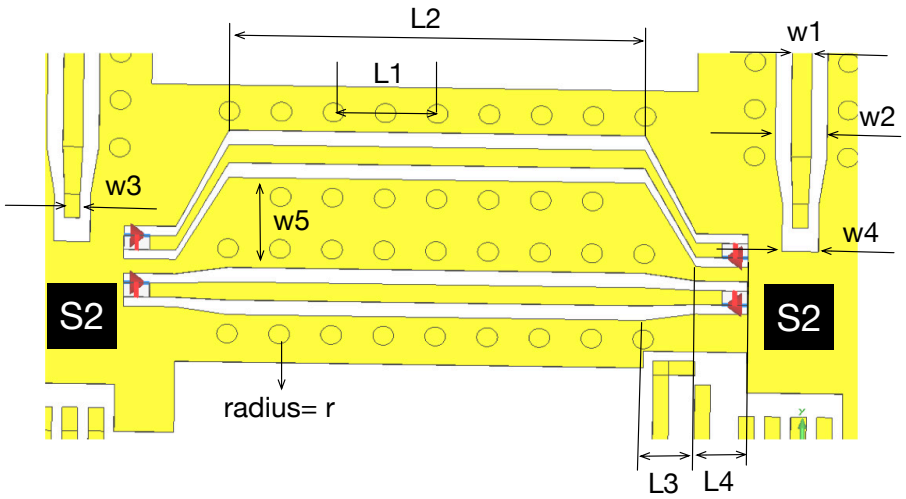

w1	w2	w3	w4	w5	L1	L2	L3, L4	r
0.38	0.98	0.3	0.5	1.8	2.0	10.0	1.0	0.2

Figure 6.19: The layout for the two GCPW lines: Tr1; and Tr2, creating the smallest phase step between two ADG MEMS devices. All dimensions are in mm.

Full wave simulation is carried out on the circuit without the ADG MEMS devices leaving their land patterns on which discrete port excitation is applied. Fig. 6.21 shows the insertions and return losses of all the RF tracks, while Fig. 6.22 shows the group delays showing the 10 ps steps. The ports are placed to connect the signal and ground pads of each device feeding the RF tracks as indicated in Fig. 6.23. This figure also show the simulation results for the phase response of the tracks connecting the six devices.

6.5.2 ADG MEMS Large Step Phase Shifter

Another phase shifter is designed with a larger step to increase the range of phase shifts required for signal cancellation. Fig. 6.24 shows the layout of the board consisting of two stages. Each uses two ADG MEMS devices to switch between four different tracks whose lengths are designed to form continuous steps of $\delta = 5\Delta$, group delay= 50 ps. The phase shifts introduced by the tracks labeled in Fig. 6.24 are distributed as follows: Tr1= δ; Tr2=Tr4= 3δ; Tr3= 2δ; Tr5= 9δ; and Tr6= 12δ, providing 16 different phase states starting

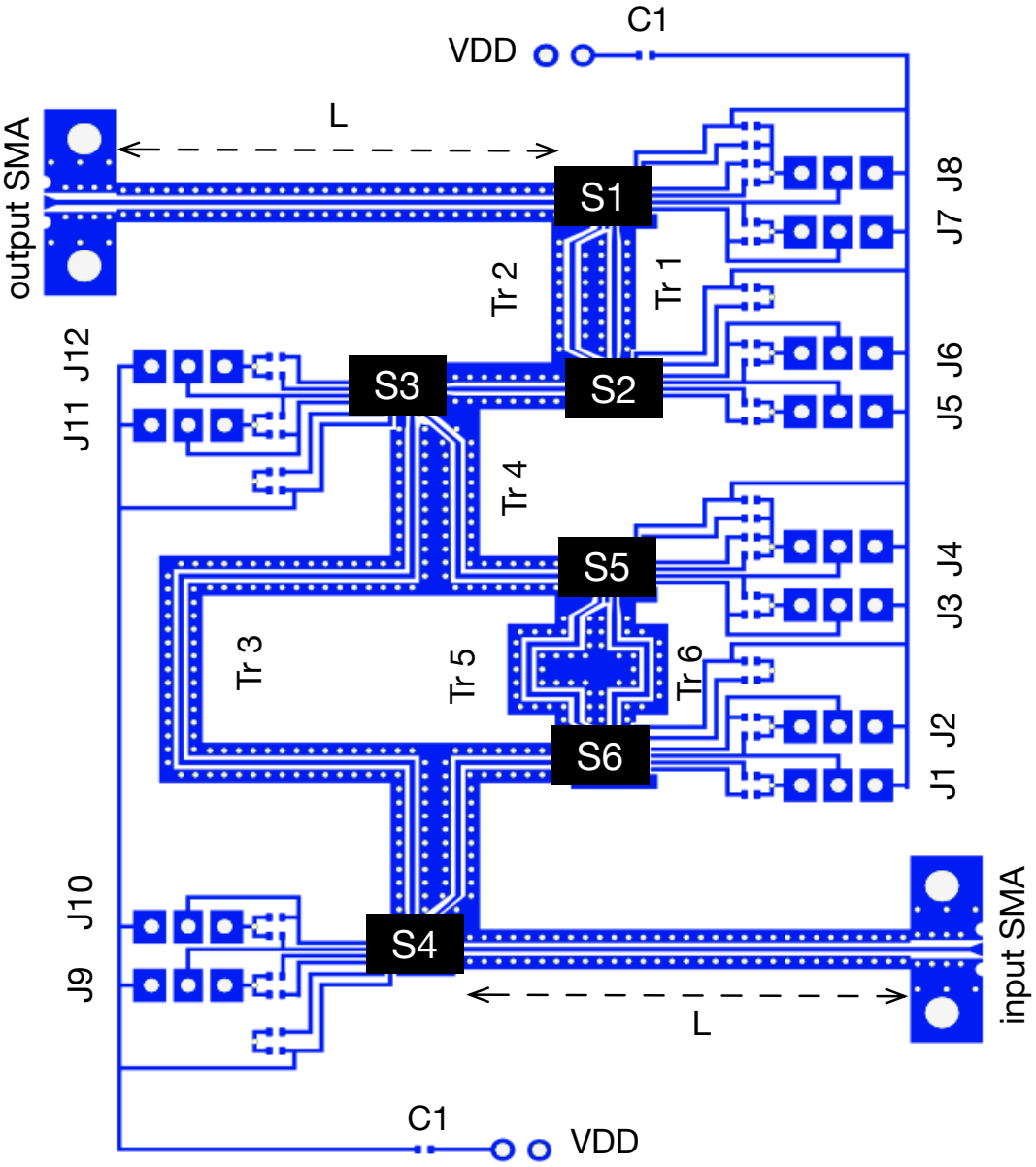

L	Tr1	Tr2	Tr3	Tr4	Tr5	Tr6
31.5	11.0	13.0	68.4	22.0	15.8	11.1

Figure 6.20: The circuit layout of the ADG MEMS phase shifter with small phase step, $\Delta = 3.24^o$ at 900 MHz. All RF tracks are labeled with Tr_n, whereas other tracks are carrying DC signals of the digital control inputs.The board dimensions are 90 x 65 mm^2 .

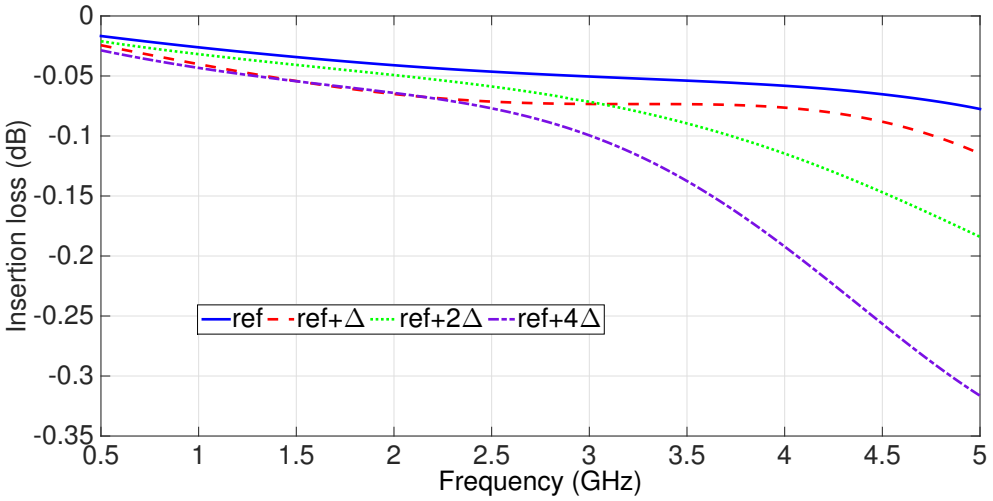

(a)

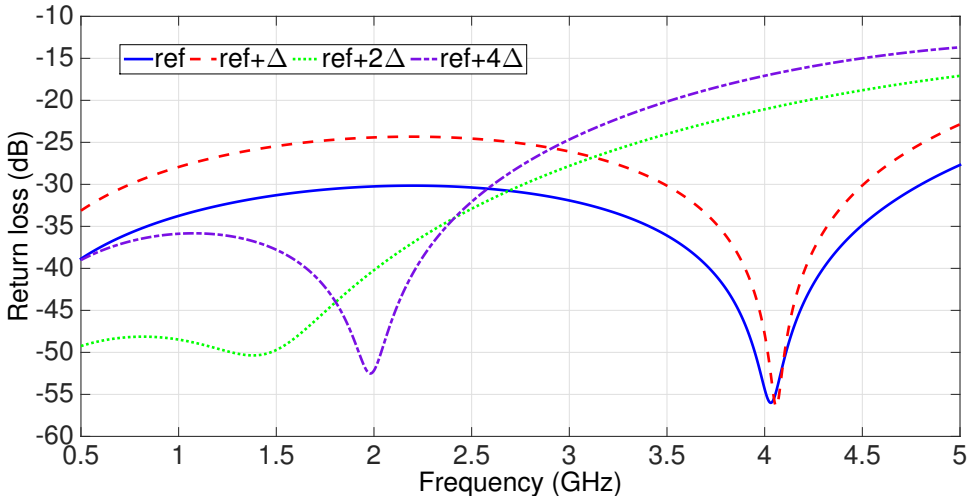

(b)

Figure 6.21: The simulated insertion (a) and return losses (b) of the six RF tracks of the small step phase shifter marked in Fig. 6.20.

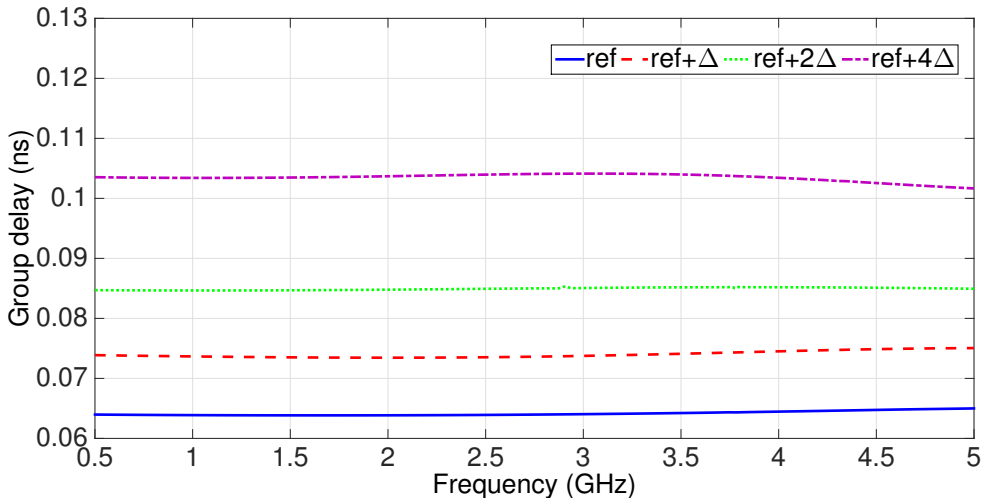

Figure 6.22: The simulated group delay of the six RF tracks of the small step phase shifter.

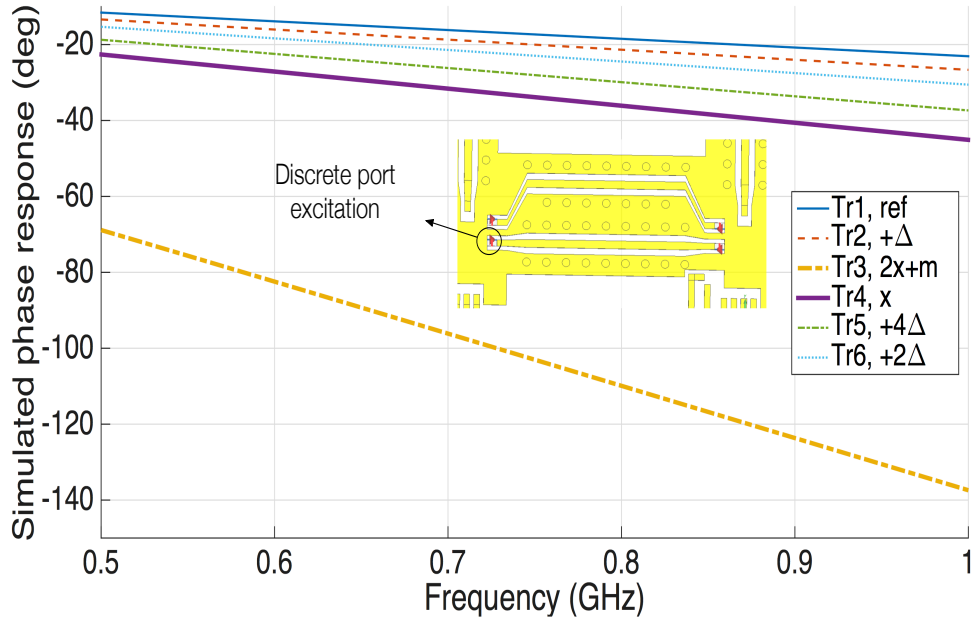

Figure 6.23: The simulated phase response of the six tracks of the small step phase shifter marked in Fig. 6.20, where x is a constant= 20^o at 900 MHz.

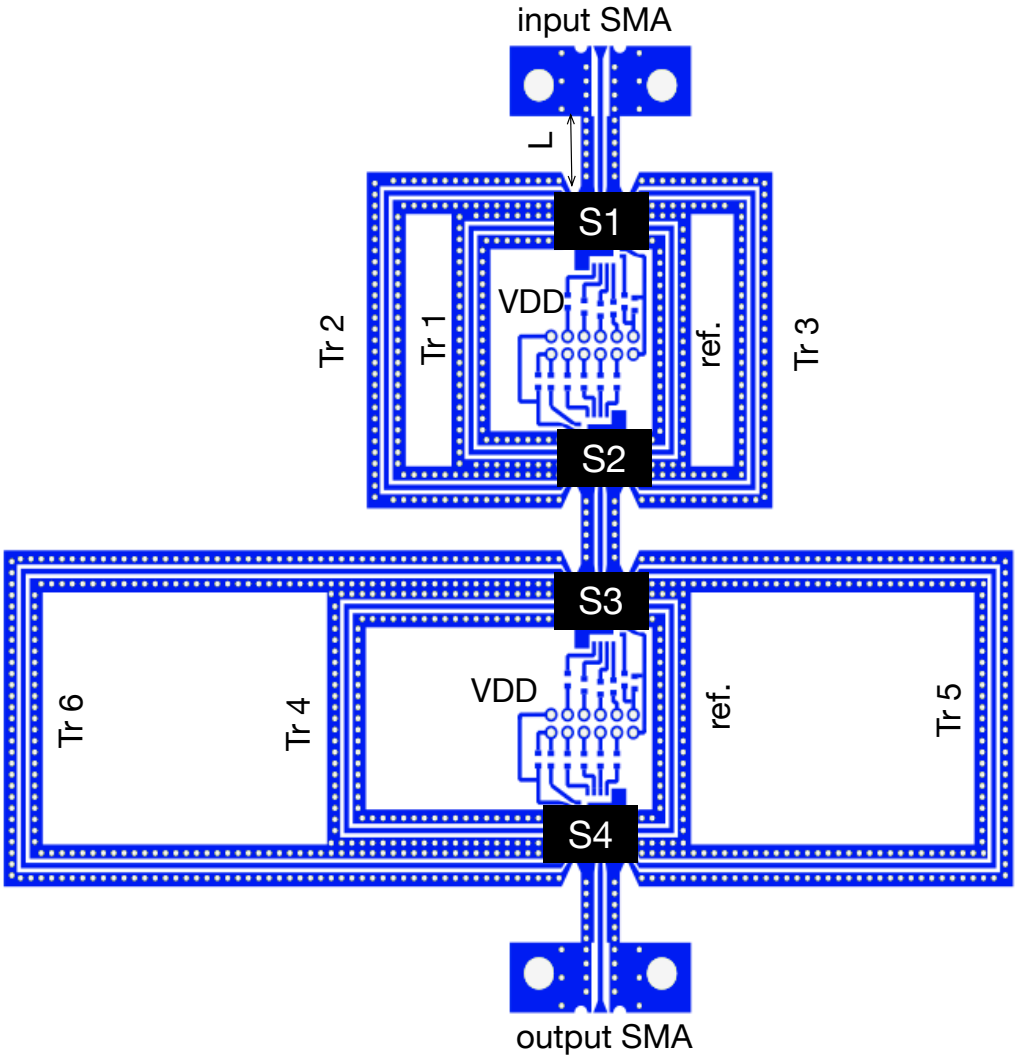

L	ref.	Tr1	Tr2	Tr3	Tr4	Tr5	Tr6
5.0	34.7	38.3	56.7	48.62	62.7	81.9	106.7

Figure 6.24: The circuit layout of the ADG MEMS phase shifters with large phase step ($\delta = 5\Delta$). The circuit size is 90 x 85 mm^2.

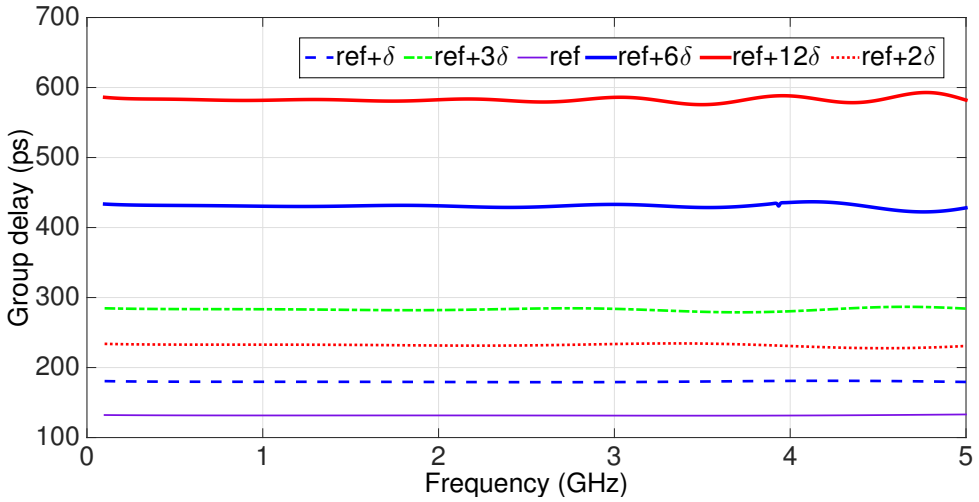

Figure 6.25: The simulated group delay for the large step phase shifter.

from 0^o up to 262.5^o at 900 MHz. Similarly, simulations are carried by applying excitation to the footprints of the devices. Fig. 6.25 and Fig. 6.26 show the simulated group delay and amplitude response for the second phase shifter, respectively. Fig. 6.27 shows the phase states for the tracks simulated from 500 MHz up to 1 GHz.

6.6 ADG MEMS Phase Shifters Measurements

Fig. 6.28 shows the fabricated printed circuit boards for both the small step and large step phase shifters. Pin headers and jumpers are used to control the voltage across the DC inputs.

Fig. 6.29 shows the measured six phase states for the small step from 500 MHz up to 1 GHz: 0^o (a1-b2); 3.5^o (a2-b2); 7^o (a1-c1); 10.5^o (a2-c1); 14^o (a1-c1); and 17.5^o (a2-c2). Fig. 6.30 shows the measured 16 phase states of the large step phase shifter starting from 0^o up to 262.5^o at the same frequency.

Fig. 6.31 and 6.32 show the measured insertion and return loss for all phase states of the small step and large step phase shifter, which indicates a maximum insertion loss

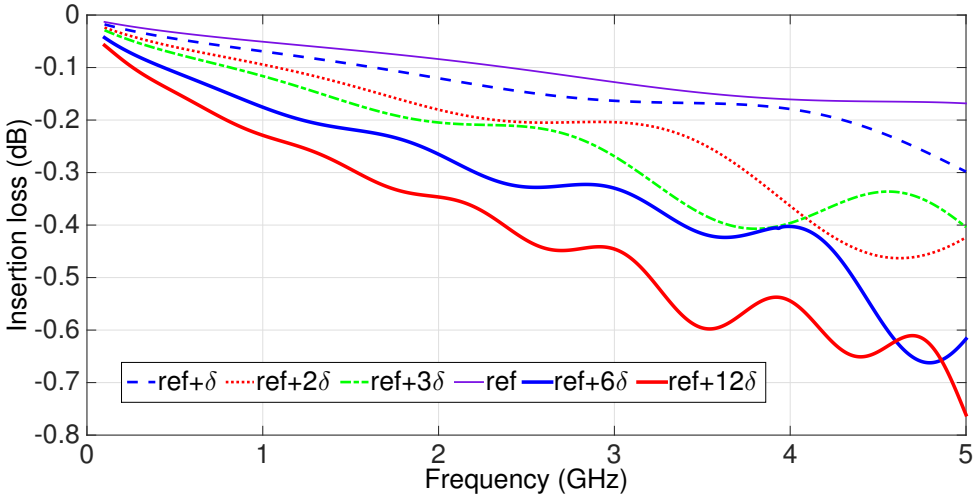

(a) Insertion loss

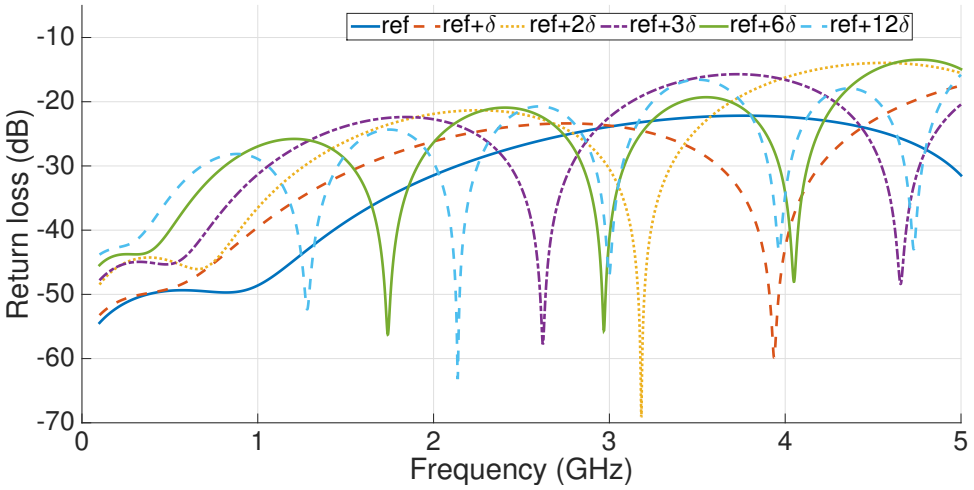

(b) Return loss

Figure 6.26: The simulated amplitude response of the RF tracks of the large step phase shifter.

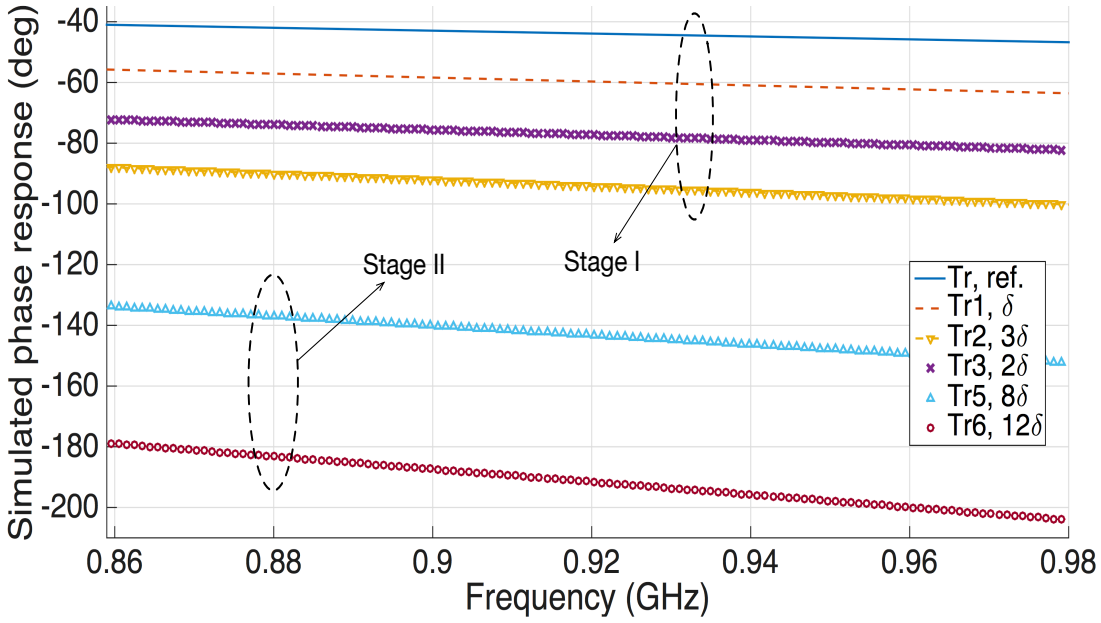

Figure 6.27: The simulated phase response of the RF tracks of the large step phase shifter marked in Fig. 6.24.

Table 6.4: The truth table of the two phase shifter circuits.

	S1	S2	S3	S4
R2	11	00	11	00
δ	11	00	00	11
2δ	11	00	01	10
3δ	11	00	10	01
4δ	00	11	11	00
5δ	00	11	00	11
6δ	00	11	01	10
7δ	00	11	10	01

	S1	S2	S3	S4
8δ	10	01	11	00
9δ	10	01	00	11
10δ	10	01	01	10
11δ	10	01	10	01
12δ	01	10	11	00
13δ	01	10	00	11
14δ	01	10	01	10
15δ	01	10	10	01

	S1	S2	S3	S4	S5	S6
R1	01	00	00	11	-	-
Δ	11	10	00	11	-	-
2Δ	01	00	01	10	11	00
3Δ	11	10	01	10	11	00
4Δ	01	00	01	10	01	10
5Δ	11	10	01	10	01	10

RF1	00
RF2	01
RF3	10
RF4	11

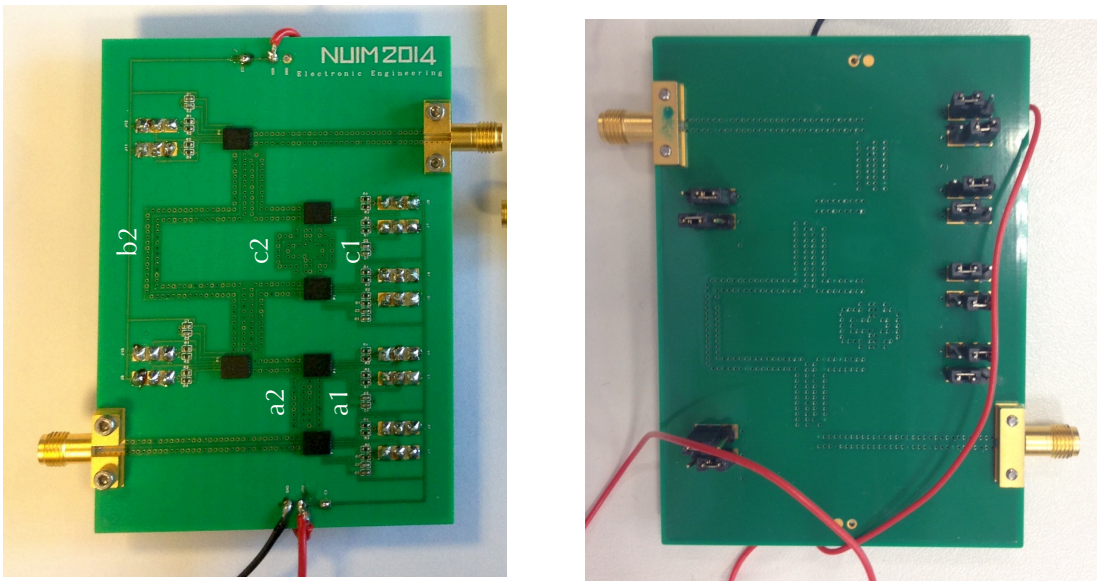

(a) Front view (b) Back view

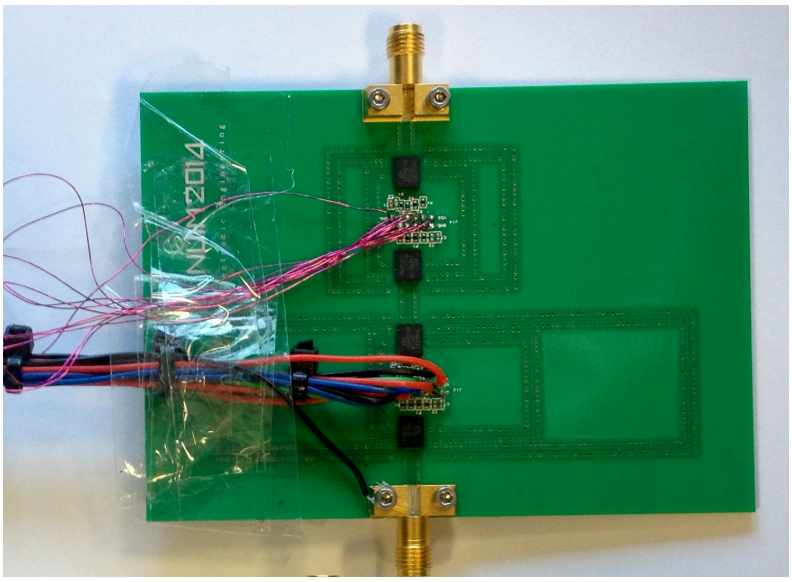

(c)

Figure 6.28: The fabricated ADG MEMS phase shifter boards. The dimensions of each board is $65x90\ mm^2$. (a) and (b) shows the front and the back view of the small step phase shifter, respectively. (c) shows the front view of the large step phase shifter.

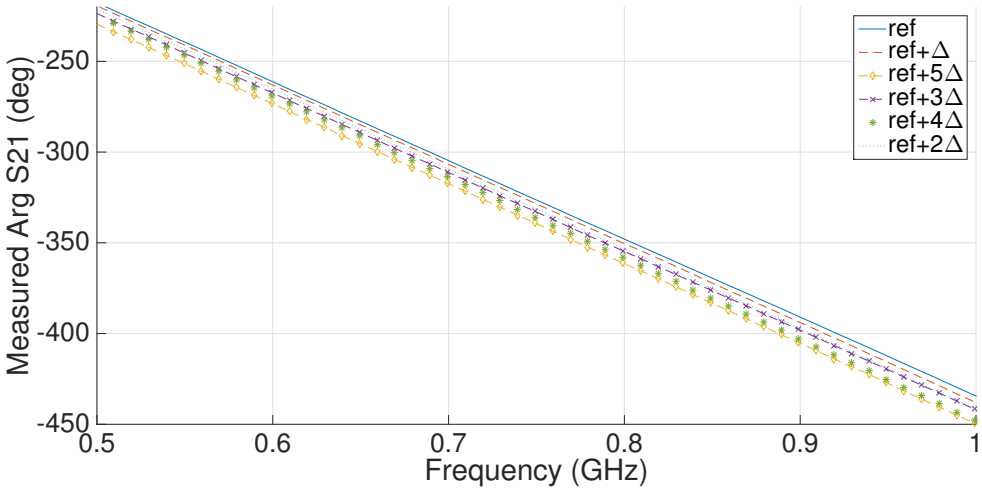

Figure 6.29: The measured six phase states for the first phase shifter circuit ($65x90\ mm^2$).

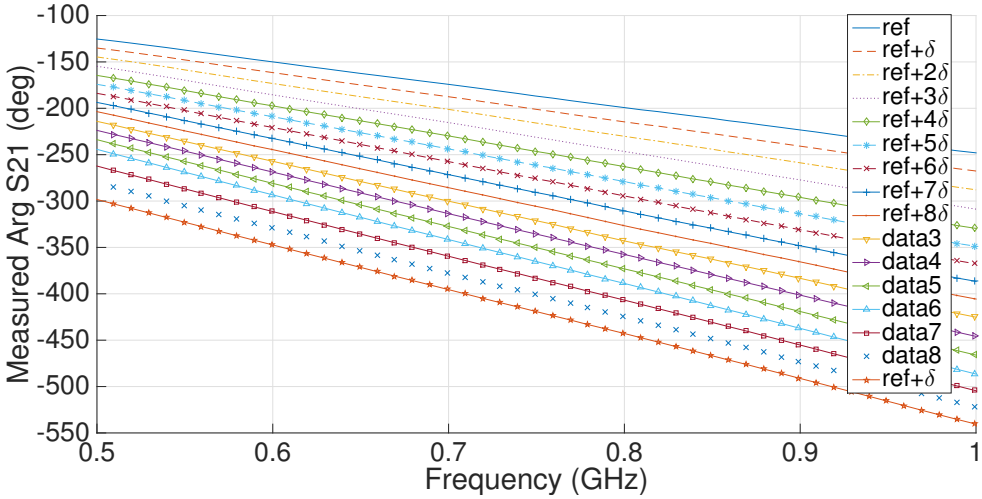

Figure 6.30: The measured phase states for the second phase shifter circuit ($65x90\ mm^2$), $\delta = 5\Delta$.

Table 6.5: A comparison between the simulation and measured results of the two phase shifters at 700 MHz, $\delta = 5\Delta$.

	Simulation results	Measured results
Δ	3.24 degree	3.5 degree
Max. IL	0.02 dB at 0^o, 0.45 dB at 15δ	0.8 dB at 0^o, 1.1 dB at 15δ
Max. RL	36 dB at 0^o, 20 dB at 15δ	28 dB at 0^o, 14 dB at 15δ

of 1.3 dB for the highest phase state.

Table.6.5 shows a comparison between the simulation and measured results. Knowing that the device losses (0.2 dB per switch) were not included in the simulation setup explains the differences in amplitude losses between simulation and measured results.

6.6.1 RMS Phase and Amplitude Deviation

Having equal amplitude response at all phase states is essential, therefore a comparison is made in Fig. 6.33 showing the changes in both the insertion and VSWR at every phase state. The amplitude and phase RMS deviation of all the phase states are calculated for the two phase shifters as shown in Fig. 6.34, which points to a maximum deviation of $\pm 0.9^o$ and ± 0.16 dB for the small step phase shifter as well as $\pm 1.56^o$ and ± 0.155 dB for the latter.

6.6.2 Linearity Test

A linearity test is conducted with two single tone signals generated at 940 MHz and 960 MHz. Fig. 6.35 shows the test setup consisting of two RF signal generators, two 20 dB couplers, Wilkinson power combiner and a set of RF attenuators. The outputs of the two signal generators are injected to each of the two couplers, whose through ports are terminated by a series of attenuators with more than 20 dB attenuation, in order to improve the isolation between the two RF sources. Knowing the fact that, the ADG MEMS switches are passive devices implies having a very high linearity characteristic

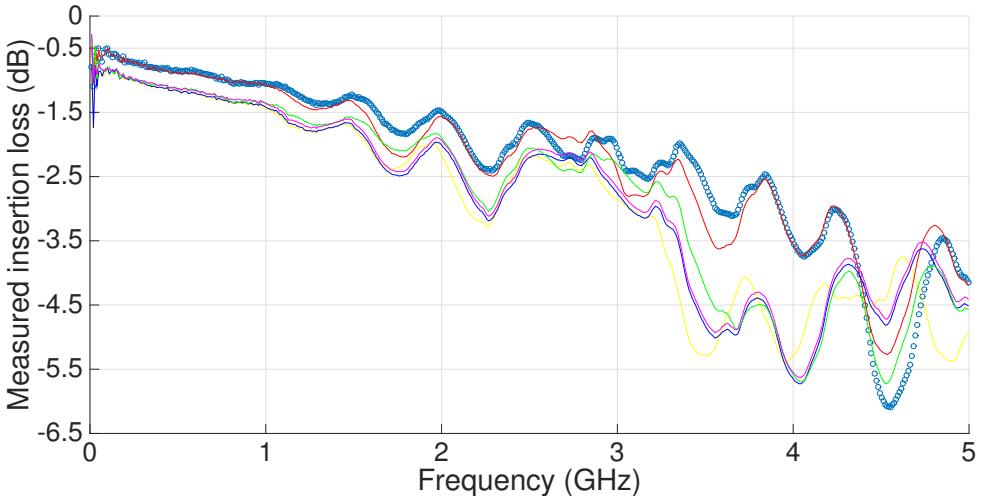

(a) Small step phase shifter

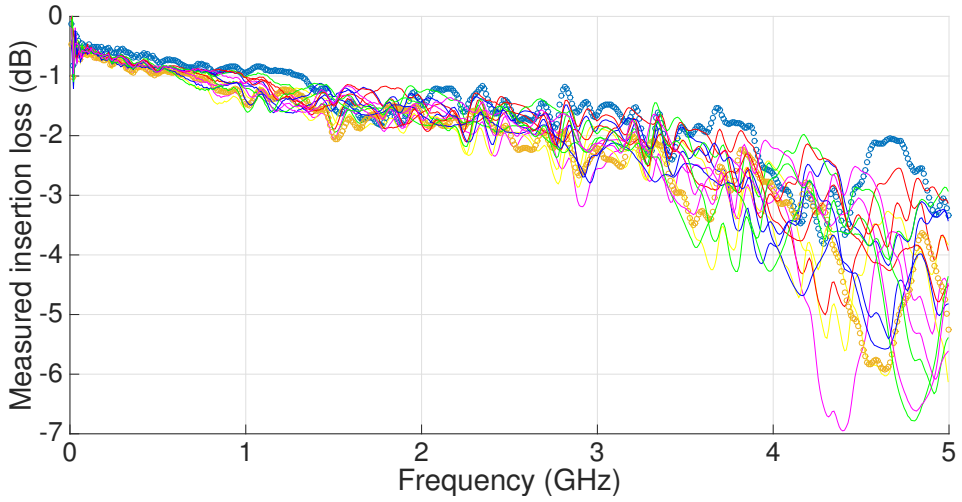

(b)Large step phase shifter

Figure 6.31: The measured insertion for all phase states of the two phase shifter circuits.

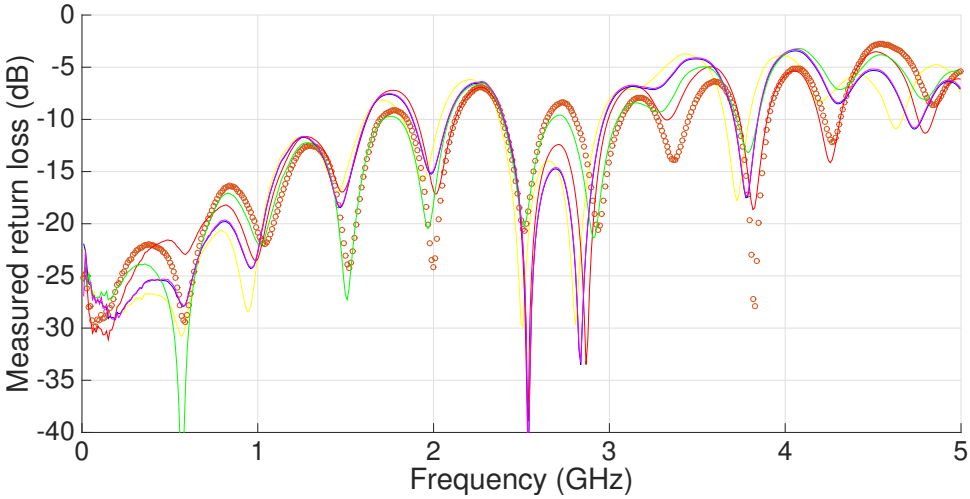

(a) Small step phase shifter

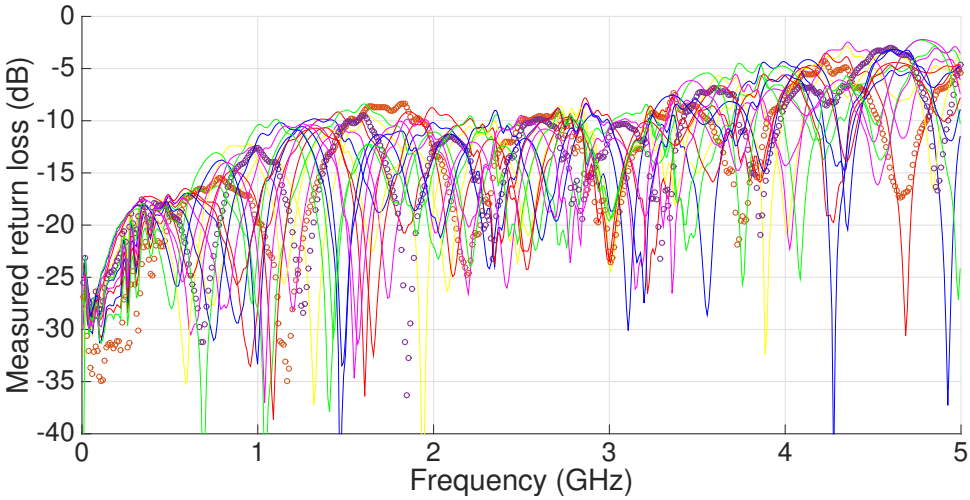

(b)Large step phase shifter

Figure 6.32: The measured return loss for all phase states of the two phase shifter circuits.

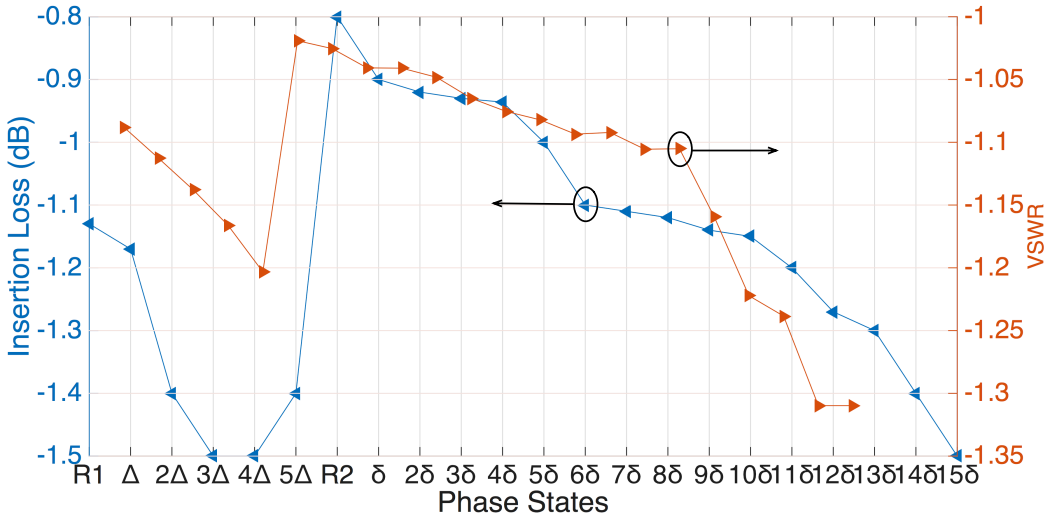

Figure 6.33: The measured insertion loss and VSWR for all phase states at 900 MHz.

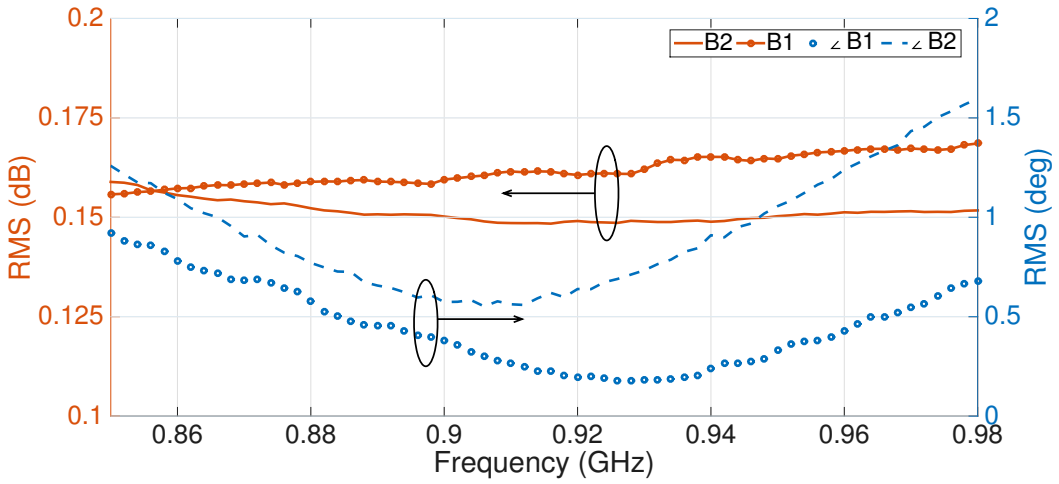

Figure 6.34: The measured RMS error in amplitude and phase for all the phase states of each of the first (B1) and second (B2) phase shifters.

	Small-step phase shifter	Large-step phase shifter
Phase step at 1 GHz	$\Delta = 3.5^o$	$\delta = 5\Delta$
No. of phase states	6	16
No. of MEMS devices	6	4
Min/ Max Insertion loss	1.1 dB to 1.5 dB	0.8 dB to 1.5 dB
Min/ Max VSWR	1.02: 1 to 1.2: 1	1.05:1 to 1.31:1
Max RMS phase in 100 MHz	$\pm 0.9^o$	$\pm 1.56^o$
Max RMS amplitude in 100 MHz	± 0.16 dB	± 0.155 dB

Table 6.6: A summary for the measured results of the two ADG MEMS phase shifter circuits.

for the phase shifter boards. This results in a high input third order intercept point (IP3), which can appear at very high input power levels (e.g. above 60 dBm). For this reason, the measurements are conducted following the method presented in [71], where the third order intermodulation distortion (IMD3) products are recorded for three different input power points. The three input power points are selected such that, the highest point is the maximum peak power that can be generated. In this case, 10 dBm, 15 dBm and 20 dBm are selected, and a straight line is plotted for the IMD3 versus the input power. Another straight line is plotted showing the relation between the input and the output power across the phase shifter, showing the power gain of the circuit (e.g. insertion loss). Extending the two straight lines identifies the location of the IIP3 point, which is the point of intersection between the two, as shown in Fig. 6.36. According to these measurements, the IIP3 point is located above 62 dBm.

6.6.3 Summary and Evaluation of the ADG MEMS Phase Shifters

6.6.3.1 A Performance Comparison with the JSPHS-1000+ Phase Shifter

A summary of the measured results for the two ADG MEMS phase shifters is listed in Table. 6.6. Table. 6.7. shows a comparison between the measured results of the new ADG MEMS phase shifter to the Mini-circuits voltage controlled phase shifter selected for the feedforward interference cancellation system in Chapter III. The results of this com-

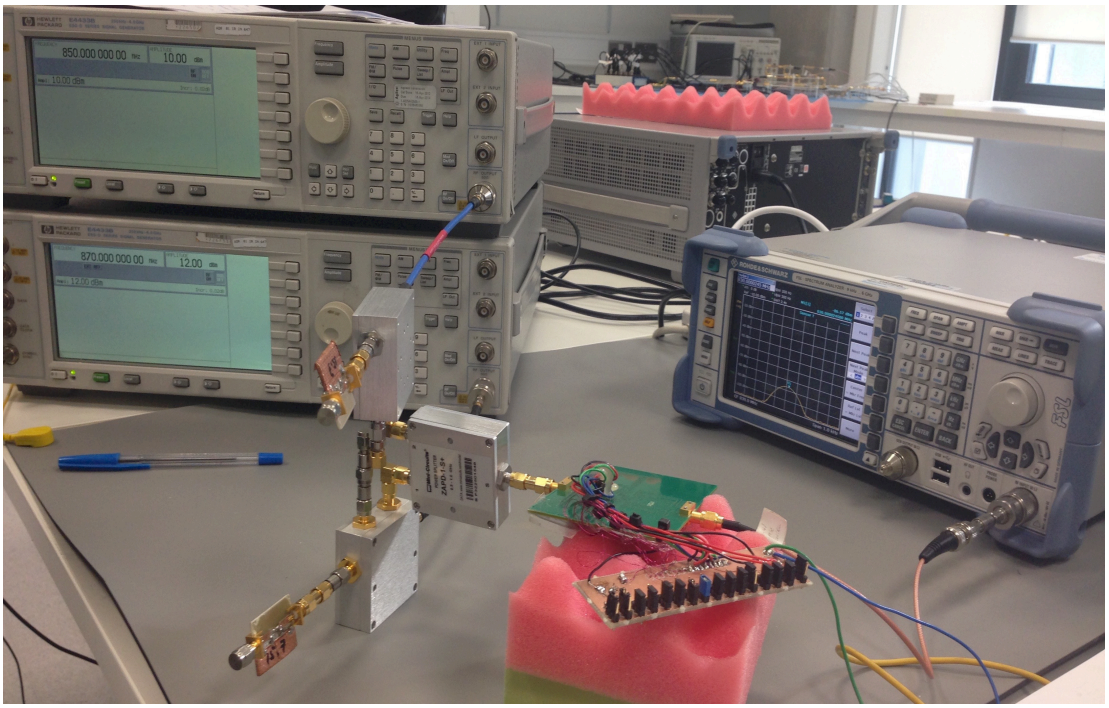

Figure 6.35: IIP3 measurements setup for the ADG MEMS phase shifter using two single tone signals at 940 MHz and 960 MHz, generated from two sources and combined using power combiners and couplers.

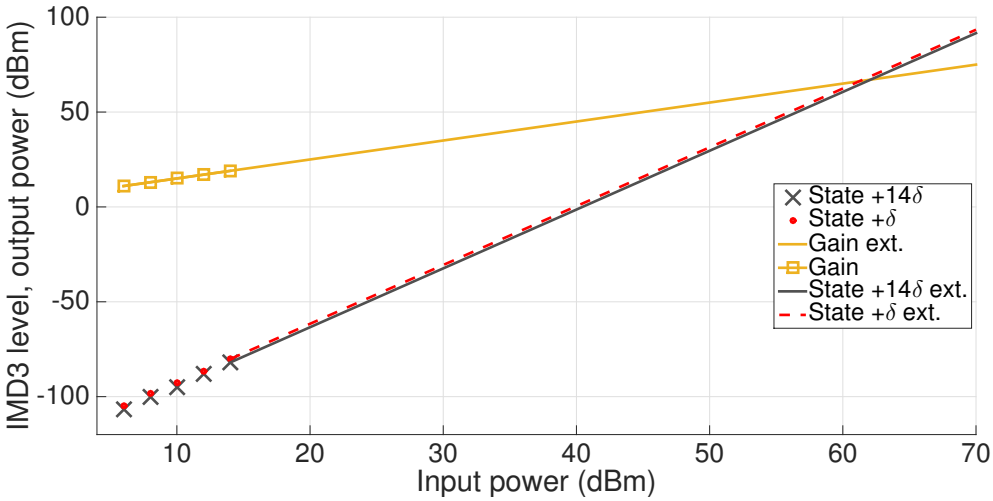

Figure 6.36: Measured IIP3 for two different phase states: state 1 ($+\delta$); and state 14 ($+14\delta$).

Table 6.7: A comparison between the performance of the new ADG MEMS phase shifters and the Mini-circuits voltage controlled phase shifter.

	ADG MEMS	JSPHS-1000+
Component type	Passive	Active
RMS amplitude deviation	± 0.16 dB	± 0.5 dB
Max VSWR	1.35: 1	2.6: 1
Min/ Max insertion loss	0.8 dB to 1.1 dB	1.2 dB to 2.2 dB
Max RF input power	36 dBm	20 dBm

parison show the effect of improving the phase linearity on the RMS amplitude deviation between the phase states of the phase shifters. ADG MEMS phase shifter have reduced the amplitude errors between the phase states by more than 66 %. In addition, both the insertion and return losses are reduced to nearly half of the losses introduced by the JSPHS-1000+, which can reduce the in-band losses in the feedforward interference cancellation system by 0.4 to 1.1 dB.

6.6.3.2 A Performance Comparison with OMRON MEMS-based Phase Shifter

Table. 6.8 shows a comparison between the large step ADG MEMS phase shifter presented in this work, and OMRON MEMS phase shifters. The OMRON phase shifter is designed based on switching LC loads via a packaged surface mount SPDT MEMS device (OMRON) [73]. The number of phase states offered by the ADG is much bigger than OMRON, due to the fact it has four switching RF ports. Despite having a larger number of switching ports, ADG MEMS phase shifters occupy much smaller board dimensions, which is less than half the size of OMRON phase shifters. Most importantly, the ADG MEMS phase shifter has dramatically reduced the phase and amplitude errors between the phase states.

Table 6.8: Table of comparison between the two MEMS switch-based phase shifters: OMRON and the ADG MEMS with large phase step.

	OMRON[73]	ADG MEMS
Switching between	LC loads	Delay lines
No. of switches	4	2
No. of phase states	7	16
Board size (λ^2)	$4.38x6.0$	$2x2.76$
Insertion loss (dB)	0.6 at 0^o	0.8 at 0^o
	1.3 at 123.75^o	1.3 at 262.5^o
Return loss (dB)	> 10	> 13
RMS phase error	$\pm 5^o$	$\pm 1.56^o$
RMS amp. error	± 1 dB	± 0.15 dB
IP3 level	> 65 dBm	> 63 dBm

6.7 Conclusion

This chapter introduces a new design for passive RF controlled phase shifters offering many advantages, which promote their use as an alternative to the active voltage controlled phase shifter component used earlier in the setup of the feedforward interference cancellation system in Chapter III (JSPHS-1000+). The phase shifters here are designed using a new RF ADG MEMS switching device. The integration of the devices on a printed circuit board is carefully studied and design guidance is provided in this chapter. The design is performed to reduce the phase errors due to non linearities in the frequency response of the phase states.

6.7.1 Summary

- A study is carried out on the flatness of the group delay of three microwave structures that can be used to construct the RF interface of ADG MEMS. The three structures are CPW with MSL transition, CPW with no transition and GCPW. GCPW proved to introduce a minimum phase deviation of ± 4 ps for 600 ns transmission line delay (0.67%), when compared to CPW lines whose results show ± 63 ps (10%)

with MSL transition and $\pm$7 ps (1.16 %) with no MSL transition for the same group delay.

- A comparison is made between two different topologies: Reflective; and Non-Reflective, for constructing the phase shifter with linear phase characteristics. The comparison is based on a mathematical analysis performed on the phase sensitivity of two topologies, which recommends the use of the latter for being more robust to impedance mismatches. Furthermore, the analysis is verified via full wave simulations of two 400 ps GCPW lines with loaded and short circuit terminations. The simulation results show larger time delay deviations for the shorted line with more than $\pm$29.5 ps for 8.5% impedance mismatch, against only $\pm$3.0 ps for the loaded line.

- A microwave structure is selected for constructing the RF interface of the device as well as the tracks required to build the phase states. The selection is done based on the results shown in the above comparison, which promotes the use of grounded coplanar waveguide structures. Another selection is performed for the Non-Reflective prototype, since it is characterized by higher phase linearity.

- The design methodology of a small-step and a large-step phase shifter are presented.

- The ADG MEMS phase shifter circuits are designed, fabricated and measured.

6.7.2 Limitations

Phase shifters based on switched true delay lines offer more flatness and stability in the group delay response. On the other hand, the true delay lines will always need a large board size, and any attempt to replace these true transmission lines can alter the flatness of the group delay, which is a critical parameter for phase shifters used in wide-band

signal cancellation.

6.7.3 Contributions

In this chapter, a new RF MEMS switched phase shifter is designed and implemented with high phase linearity. Measurements of the phase shifter have shown reduced amplitude and phase deviation between the phase states over a 100 MHz bandwidth, when compared to the phase shifter module used in constructing the signal cancellation test bench in the previous chapters. These reduced deviations in amplitude and phase can assist in improving the phase matching between the two signal paths in the feedforward interference cancellation system over a wide band, thus improving the overall cancellation performance.

Chapter 7

Conclusion

This thesis presents a new promising solution for RF inter-channel interference created by spectrum congestion of multiple operators. An exemplar of spectrum congestion appears in the 700 MHz spectrum (Upper-700 MHz band) between public safety operators and commercial LTE mobile operators. This specific spectrum is selected as a use case for this thesis, and the solution developed is designed and tested for handling the interference risks in this band. However, the idea and the methodology presented in this thesis can still be used to develop similar solutions for inter-channel interference in other frequency bands.

The commercial mobile LTE operating in the 700 MHz spectrum are allocated 9 MHz for each of the upper and downlink, while the broadband public safety operators employ 5-9 MHz signals, which are also following the LTE standards. Broadband public safety also interoperate with the traditional digital land mobile radios, which are sharing the same frequency spectrum. The allocated guard band between these three different operators are less than 2 MHz, and the difference in the power levels between each two neighboring channels are relatively large. As a result, several interference issues have been created.

The thesis begins with studying the minimum requirements set for handling out of band interference signals in different LTE base station transceivers, as defined in the

3GPP specifications. The study is extended to the microwave front-end duplexers employed in large-cell and small-cell base stations, which have shown some limitations in meeting the LTE standard requirements. In fact, some researchers have managed to improve the out of band rejection of the duplexers employed in large-cell base stations, which are based on air-cavity resonators, however none has succeeded in enhancing ceramic based duplexers used in small-cell base stations. Thus, small-cell base station transceivers are more prone to interference risks in the specified spectrum, and looking into solutions for improving interference rejection of these transceivers has become the main interest of this work.

After reviewing existing interference management techniques for interference signals generated by different sources including unwanted emissions in the transmitter, or by the leaking of transmitter power into the receiver chain, or by neighboring channels, it is found that there are power limitations for techniques involving feedforward interference cancellation with baseband filtering, as well as instability issues for those using feedback cancellation loops instead. In addition, they have shown a dramatic increase in the noise figure and non-linearities of the system. On the other hand, the feedforward cancellation applied on the unwanted emissions in the transmitter, which does not involve baseband filtering, have inspired the authors to apply a similar approach on out of band interferers using RF hardware only. In this case, all the power limitations and noise issues are eliminated, while leaving the challenge of developing a sharp rejection filter and wide-band signal matching. A second review is conducted on microwave filters, which failed in providing sharp rejection while meeting the size constraints in small-cell base stations. This has become the first obstruction in developing an RF interference cancellation system.

This thesis has introduced new design methodologies for successfully obtaining low profile planar band-stop resonators (one port band-stop filter) with sharp rejection characteristics (high roll-off rate). Providing a sharp rejection characteristic, this resonator has made it possible to implement an RF system that can handle interference risks in

congested frequency spectrums without the need of any digital hardware, which is a big achievement in this thesis. Eliminating the digital hardware has the advantage of overcoming the distortion due to noise and non-linearities. In general, this thesis presents the design procedures, implementation, and testing of the interference cancellation system using the new band-stop resonators.

7.1 Thesis Summary

7.1.1 Chapter III

In this chapter, the architecture of the proposed RF interference cancellation system, consisting of two main stages: filtering; and signal matching, is presented together with the performance requirements, which are imposed on each of the RF components employed. The chapter has also discussed the practical implementation of the system by first selecting some of the off-the-shelf RF hardware components, then proposing new design solutions for handling very close interferers, so that the system becomes capable of handling some of the challenging interference scenarios in the 700 MHz band. Knowing that, in this specific band, interferers can appear at only a few MHz away from the receiver edge (e.g. < 20 MHz) adds the first key challenge to the design of the band-stop resonator used in the filtering stage. The system architecture has adopted the use of band-stop resonators rather than filters, because it occupies half the space needed for a two port filter.

More challenges appear in the second stage where perfect signal matching is indispensable for interferers with dynamic bandwidths and power levels. Hence, this chapter has presented a study of the effect of phase and amplitude errors on signal cancellation. The study has shown that a minimum of 29 dB signal cancellation can be obtained, when the tolerance level for the amplitude error is below ± 0.75 dB, given a zero phase error, or when the tolerance level for the phase is less than 2^o, given a zero amplitude error. As

presented in the literature review, the minimum efficiency requirements for recovering an LTE received signal necessitate introducing a minimum of 29 dB additional attenuation to the stop-band of the front end duplexers at the presence of large interference signals (> -20 dBm).

High performance off-the-shelf components are selected in this chapter to setup a big part of the new feedforward interference cancellation system. These components have included a low noise power amplifier, an active voltage controlled phase shifter and a bi-directional coupler. All these components are characterized and measured in this chapter. Measurements of the phase shifter have indicated poor linear phase response, and Chapter IV has presented an alternative passive design for RF MEMS-based phase shifters with improved phase linearity.

7.1.2 Chapter IV

This chapter has presented the first design methodology in this thesis for low profile band-stop resonators with sharp rejection. The design presented can be similar to transversal or moving average filters used for analog and digital frequencies. The idea of these resonators is based on dividing the RF signal among multiple taps with different group delays, which are later recombined forming maxima and nulls. This method is adopted to provide high roll-off rate between the pass and stop band. An analysis is conducted on the circuit structure of the resonator showing the effect of each of the circuit parameters on the overall frequency response by applying circuit simulations. The analysis is verified mathematically after deriving the transfer function of the resonator. A new methodology is developed for optimizing the power split ratio between the taps of the resonator for improving the stop-band rejection. The results of the analysis together with the new optimization method are applied and used to construct a four tap band-stop resonator. The circuit is implemented using microstrip technology on a high permittivity substrate.

Measurements of the four tap resonator have achieved a minimum roll-off rate of 1.3

dB per MHz, a 3 dB bandwidth of 11 MHz and more than 25 dB rejection over 40 MHz bandwidth. These results have made this component suitable for separating two 10 MHz signals that are 20, 15 and even 10 MHz apart, and this separation can exceed 26 dB, 19.5 dB, and 13 dB, respectively.

Furthermore, this chapter has demonstrated a test bench for the new interference cancellation system using the components selected in Chapter III together with the new four-tap band-stop resonator designed in this chapter. Two 10 MHz LTE modulated input signals are generated in the test setup to represent the wanted received signal (-50 dBm) and the interferer (-20 dBm). Three test cases are identified and measured. In the first test case, the power spectrum measurements of the output signals have shown 45 dB cancellation at the center frequency of the interferer, given that it is located at 20 MHz away from the receiver band. In addition, 25 dB cancellation are achieved over the whole band of the interferer, which indicate an increase in the SIR by 29.5 dB. In the second and third test cases, the separation between the two signals is reduced to 15 and 10 MHz, respectively. The test results have shown a rejection of 45 dB and 20 dB, with an increase in the SIR by 26.5 and 13 dB, for the 15 and 10 MHz frequency separation, respectively.

7.1.3 Chapter V

This chapter has presented another design methodology for band-stop resonators inspired by the method used in the previous chapter. It is based on a new observation on the behavior of artificial left-handed transmission lines. The new observation is explained, verified mathematically and by applying circuit simulations. The new method is used in this chapter to construct new band-stop resonators with the same rejection performance as that described in Chapter IV, after reducing the circuit size by more than 66%.

In this chapter, two band-stop resonators are designed, fabricated and measured using two-cell and three-cell lumped capacitors and short circuited stubs. The resonators are realized using composite right-left hand transmission lines, thus referred to as CRLH

band-stop resonators. They are fabricated in a low profile planar circuit board printed on a standard FR4 material, which is more economical in cost when compared to the Rogers material used in Chapter IV. Measurements of the two-cell resonator have shown three transmission zeros with more than 24.8 dB rejection and 1.14 dB per MHz roll-off rate. Measurements of the three-cell resonator have shown 30 dB rejection with more than 1.41 dB per MHz roll-off rate.

The feedforward cancellation system is again tested using the same setup as in Chapter IV, except for using the new CRLH band-stop resonators. Four test cases are defined with the interferer located at different locations away from the receiver band, and at different power levels. Successful cancellation is obtained for 10 MHz modulated interference signals located at 20, 15 and 10 MHz away from the 10 MHz receiver with a value of 34, 45, and 35 dB, respectively. The test results have also shown the same cancellation performance after increasing the power level of the interference signal by 30 dB. Finally, the SIR levels have shown an increase of more than 20 dB in the test results of each of the four test cases.

7.1.4 Chapter VI

Chapter VI introduced the design and implementation of new RF MEMS switch-based phase shifters, which are designed using a new RF MEMS device. The phase shifter circuits are designed with high phase linearity promoting their use as an alternative to the active voltage controlled phase shifter component (JSPHS-1000+), which was first selected in Chapter III and used in the setup of the interference cancellation test bench in Chapter IV and V.

The new MEMS device is characterized in this chapter, then the device integration on a printed circuit board is carefully studied and the phase shifter design guidance are provided. The study has involved evaluating the phase linearity of several microwave structures, which is performed by applying full wave EM simulations on every prototype.

A similar evaluation is performed on the phase linearity of two different circuit topologies using reflective and non-reflective delay lines.

The use of grounded coplanar waveguide structures and non-reflective circuit topology are selected, since both has proved to have reduced phase errors due to non linearities in the frequency response of the selected phase states. Two new RF MEMS-based phase shifter circuits are realized, fabricated and measured with small and large phase steps. Measurements of the new RF MEMS-based phase shifters are compared to the JSPHS-1000+ component. The comparison has shown that the RMS amplitude deviation has been successfully reduced by more than 66%. In addition, both the insertion and return losses are reduced to nearly half of the losses introduced by the JSPHS-1000+. This can directly reduce the in-band losses in the feedforward interference cancellation system by 0.4 to 1.1 dB.

7.2 Future Work

This thesis has achieved successful cancellation for high power wideband modulated interference signals appearing at small frequency offsets from the receiver. The cancellation performance is tested with a minimum separation of 10 MHz between the interference signal and the receiver. According to the study presented in Chapter III, in regard to the interference scenarios in the 700 MHz spectrum between public safety land mobile radios and commercial mobile LTE receivers, the separation between the two signals can reach down to 2 MHz. Moreover, the power level of the interferer can be 40 dB above the level of the received signal, which can be considered as the worst case interference scenario in this band. As a result, the first target of our future work is to modify the design of the band-stop resonators, so that it can handle less than 10 MHz separation between the pass and the stop bands.

Our future work will also focus on how to miniaturize the hardware components used

in the interference cancellation system. An example, Wilkinson power dividers occupies a large space in the circuit layout of the new resonators, as it is realized using quarter wave transmission lines. These lines are used for matching the impedance at the input of the divider to the output ports, which are all following the standard 50 Ω impedance system. For future work, an investigation needs to be carried out on the possibility of eliminating the Wilkinson power dividers from the layout of CRLH-based band-stop resonator. This investigation will be based on adjusting the characteristic impedance of the artificial left-handed transmission lines to 100 Ω. In this case, a T-power divider can be used as an alternative for Wilkinson, and this can lead to a further reduction in the size of the board by more than 50%.

Nomenclature

ACLR	Adjacent Channel Leakage Ratio
ACS	Adjacent Channel Selectivity
ADG	Analog Devices Co.
ADS	Agilent Design Systems
BS	Base Station
CPW	Coplanar Waveguides
CRLH TL	Composite Right-Left Handed Transmission Lines
DL	Down Link
FCC	Federal Communications Commission
FDD	Frequency Division Duplex
GCPW	Grounded Coplanar Waveguides
HSPA	High Speed Data Packet
IMD	Intermodulation Distortion
LDCC	Lumped Distributed Capacitively Coupled Filters

LHTL	Left Handed Transmission Lines
LMR	Land Mobile Radios
LNA	Low Noise Amplifier
LTE	Long Term Evolution
MEMS	Micro-Electro-Mechanical Switches
MSL	Microstrip Line
OOB	Out of Band Emissions
PCB	Printed Circuit Board
PS	Public Safety
SIR	Signal To Interference Ratio
TETRA	Trans-European Trunked Radio
UE	User Equipment
UL	Upper Link
VNA	Vector Network Analyzer

Bibliography

[1] 3GPP's program to provide integrated public safety communications through LTE, IEEE Workshop on Public Safety Communications, 27th September 2013, Berlin, Germany (by Matthew Baker).

[2] Service Rules for the 698-746, 747-762 and 777-792 MHz Bands, et al., PS Docket No. 06-229, Second Report and Order, 22 FCC Rcd 15289, 15415-348 (2007).

[3] Donny Jackson, "Obama makes it official, signs D Block legislation", Urgent Communications, Feb. 2013.

[4] 3rd Generation Partnership Project (3GPP), Technical Specification (TS) no. 36.104 produced by European Telecommunications Standards Institute (ETSI), version 9.4.0, Release 9.

[5] 3rd Generation Partnership Project (3GPP), Technical Specification (TS) no. 36.104 produced by European Telecommunications Standards Institute (ETSI), Release 14.

[6] H. Holma and A. Toskala, "LTE for UMTS – OFDMA and SC-FDMA Based Radio Access", A John Wiley & Sons, Ltd., Publication, 2009.

[7] Anton A. Huurdeman, "The Worldwide History of Telecommunications", John Wiley & Sons, 31 juli 2003

[8] S. Sesia, F. Issam and F. M. Baker, ”LTE – The UMTS Long Term Evolution”, A John Wiley & Sons, Ltd., Publication, 2nd edition, 2011.

[9] 3rd Generation Partnership Project (3GPP), Technical Specification (TS) no. 36.104 produced by European Telecommunications Standards Institute (ETSI), Release 11.

[10] 3rd Generation Partnership Project (3GPP), Technical Specification (TS) no. 36.104 produced by European Telecommunications Standards Institute (ETSI), Release 6.

[11] David Pozar, Microwave Engineering, 2nd edition, Wiley, New York, NY, 1998.

[12] Robert E. Collin, “Excitation of Waveguides and Cavities”, Wiley, 1991.

[13] Annapurna Das and Sisir K Das, Microwave Engineering, McGraw-Hill, New Delhi, 2007.

[14] K. Fujisawa ”General treatment of Klystron resonant cavities”, IRE transactions on microwave theory and techniques, Oct. 1995.

[15] S. Jang and K. Park ”Dual block ceramic resonator filter having common electrode defining coupling/tuning capacitors”US patent, Mar. 1997.

[16] Siamak Fouladi, Member, IEEE, Fengxi Huang, Student Member, IEEE, Winter Dong Yan, Member, IEEE, and Raafat R. Mansour, Fellow, IEEE, “High- Narrowband Tunable Combline Bandpass Filters Using MEMS Capacitor Banks and Piezomotors” IEEE MTT, vol. 16, no. 1, Jan 2013.

[17] Fengxi Huang, Student Member, IEEE, Siamak Fouladi, Member, IEEE, and Raafat R. Mansour, Fellow, IEEE,”High- Tunable Dielectric Resonator Filters Using MEMS Technology” IEEE MTT, vol. 59, no. 12, Dec. 2011.

[18] M. Hoft and S. Burger, ”Corner rounding for increased quality factor of cavity resonators” Asia-Pacific Microwave Conference Proceedings, 2005.

[19] I. Kim, J. Cha, S.Hong and B. Kim ”Predistortion Power Amplifier for Base-Station using a Feedforward Loop Linearizer” European Microwave Conference, 2006.

[20] Y. C. Jeong, D. Ahn, C. D. Kim and I. S. Chang, ”A Feedforward Amplifier using an Equal Group Delay Cancellation Technique”, Microwave Journal Article, June 2013 .

[21] S. Kang, I. Lee and K. Yoo, “Analysis and Design of Feedforward Power Amplifier”, IEEE MIT-S Digest, 1997.

[22] H. Park, H. Yoo, S. Kahng and H. Kim, “Broadband tunable third-order IMD cancellation using left-handed transmission lines based phase shifter”, IEEE Microwave and Wireless components letters, July 2015.

[23] Y. C. Jeong, D. Ahn, C. D. Kim and I. S. Chang, “Feedforward amplifier using equal group-delay signal canceller”, IEEE MTT-S Int. Dig., Jun. 2006.

[24] A. Echeverria, L. Fan, S. Kanamaluru, and K. Chang, “Frequency tunable feedforward amplifier for PCS applications,” in Proc. Emerging Technology Symposium in Wireless Communication Systems, April 1999.

[25] Y. Hau, V. Postoyalko, and J. Richardson, “A microwave feedforward amplifier with improved phase compensation and wide band distortion cancellation”, IEEE MTT-S Int. Dig., 1997.

[26] K. Eero, K. Pasi, H. Antti, H. Veli-Matti, P. Jani, T. Timo, L. Sandro, K. Tapio and S. Hans,”Small Size Receiver Band Self Interference Cancellation Amplifier for 4G Transceivers”, November 2012

[27] J. Jung, C. Park and K. Yeom, “A Novel Carrier Leakage Suppression Front End for UHF RFID Reader”, IEEE Transactions on Microwave Theory and Techniques, Vol. 60, No. 5, May 2012.

[28] R. Gharpurey and S. Ayazian, “Feedforward interference cancellation in narrowband receivers,” in Proc. IEEE DCAS’06Workshop, 2006, pp. 67–70.

[29] S. Ayazian and R. Gharpurey “Feedforward interference cancellation in radio receiver front ends” IEEE Transactions on Circuits and Systems, vol. 54, no. 10, Oct. 2007.

[30] T. Werth, C. Schmits, R. Wunderlich and S. Heinen “An active feedback interference cancellation technique for blocker filtering in RF receivers front-ends” IEEE Journal of Solid State Circuits, vol. 45, no. 5. May 2010.

[31] L. E. Franks and I. W. Sandberg, “An Alternative Approach to the Realization of Network Transfer Functions: The N-Path Filters,” Bell Sys. Tech. J., vol. 39, pp. 1321-1350, Sept. 1960.

[32] Amir Ghaffari, Eric Klumperink, Bram Nauta, “8-Path Tunable RF Notch Filters for Blocker Suppression”, IEEE International Solid-State Circuits Conference, Feb. 2012

[33] A. Ghaffari, E. Klumperink, M. Soer, and B. Nauta, “Tunable High-Q N-Path Band-Pass Filters: Modeling and Verification,” IEEE J. Solid-State Circuits, vol. 46, no. 5, pp. 998–1010, May 2011.

[34] M. Sanchez- Renedo and R. Gomez-Garcia, “Tunable Combline Filter With Continuous Control of Center Frequency and Bandwidth” IEEE Transactions on Microwave Theory and Techniques, Vol. 53, No. 1, January 2005.

[35] J. D. Ruiz, J. Hinojosa, and A. Alvarez-Melcon, “Microstrip notch filters based on open interconnected split ring resonators (OISRRs),” Appl. Phys. A, vol. 112, pp. 263-267, August 2013.

[36] J. Hinojosa, F. L. Martínez-Viviente, J. Ruiz and A. Alvarez-Melcon “Modified Split-Ring Resonator for Microstrip Dual-Band Notch Filter” Proceedings of the 45th European Microwave Conference.

[37] Xuemei Zheng and Tao Jiang “Realization of dual notch bands in UWB bandpass filter using two T-shaped resonators”, Applied Computational Electromagnetics Society Symposium, Italy 2017.

[38] J. R. De Luis, A. Moris, and Q. Gu “A tunable asymmetric notch filter using RFMEMS”, IEEE MTT-S InternationalMicrowave Symposium Digest (MTT), 2010.

[39] B. Carey-Smith, P.A. Warr, M. A. Beach and T. Nesimoglu “Tunable Lumped-distrbuted Capacitvely Coupled Transmission Line”, Electronics Letters, Vol. 40, No. 7, 2004.

[40] B. Carey-Smith, Paul A. Warr, Mark A. Beach and Tayfun Nesimoglu, “Wide Tuning-Range Planar Filters Using Lumped-Distributed Coupled Resonators” IEEE TRANSACTIONS ON MICROWAVE THEORY AND TECHNIQUES, VOL. 53, NO. 2, FEBRUARY 2005.

[41] J. S. Hong and M. J. Lancaster, "Microstrip Filters for RF/Microwave Applications," John Wiley, New York, 2001.

[42] M. Hayati, M. Gholami, H. S. Vaziri and T. Zaree, "Design of microstrip lowpass filter with wide stop-band and sharp roll-off using hex-angular shaped resonator," Electron. Letters. vol. 51, no. I, pp. 69-71, Jan. 2015.

[43] H. Cui, J. Wang and G. Zhang, “Design of microstrip low pass filter with compact size and ultra-wide stop-band,” Electron. Letters., vol. 48, no. 14, pp. 856 - 857, July 2012.

[44] M. H. Yang and J. Xu, “Design of compact broad-stop-band lowpass filters using modi ed stepped impedance hairpin resonators,” Electron. Letters., vol. 44, no. 20, pp. 1198 - 1200, Sept. 2008.

[45] V. K. Velidi and S. Sanyal, “Sharp roll-off lowpass filter with wide stop-band using stub-loaded coupled-line hairpin unit,” IEEE Microwave. Wireless Components. Letters., vol. 21, no. 6, pp. 301-303, June 2011.

[46] Raphika P. M., Abdulla P., Jasmine P. M., "Compact microstrip elliptic function lowpass filter with sharp roll-o and wide stop-band by cascading multiple patch resonators," IEEE International Microwave & RF Conference, Bangalore, India, 2014, pp. 316-319.

[47] Raphika P. M., Abdulla P., Jasmine P. M., "Compact microstrip lowpass filter with sharp roll-o and wide stop-band by cascading multiple resonators" Asia Paci c Microwave Conference, Sendai, Japan, 2014, pp-1229-1231.

[48] P. M. Raphika, P. Abdulla, P. M. Jasmine, "Compact lowpass filter with a sharp roll-off using patch resonators," Microwave. and Opt. Tech. Letters., Vol. 56, no. 11, pp. 2534-2536, Nov.2014.

[49] Raphika P.M., Abdulla P., Jasmine P. M. “Planar Lowpass Filter with sharp Roll-off using Patch Resonators on High Impedance Microstrip Line” Radio and Antenna Days of the Indian Ocean (RADIO), 2015.

[50] M. Wyville and J. Wight, “Frequency Agile RF Filter for Interference Attenuation,” IEEE Radio Wireless Symposium 2012.

[51] M. Kim, J. B. Hacker, R. E. Mihailovich, and J. F. DeNatale, “A DC-to-40GHz four-bit RF MEMS true-time delay network”, IEEE Microwave and Wireless Components Letters, vol. 11, No. 2, February, 2001.

[52] M. Kim, J. B. Hacker, R. E. Mihailovich, and J. F. DeNatale, \A DC-to-40GHz four-bit RF MEMS true-time delay network", IEEE Microwave and Wireless Components Letters, vol. 11, No. 2, February, 2001.

[53] M. Roy, “Distortion cancellation performance of miniature delay filters for feed-forward linear power amplifiers”, IEEE Ultrasonics Symposium, October 7-10, 2001.

[54] Y. Du, J. Bao Z. He and J.Jiang, “A X band Switched Line 5 bit Phase Shifter with RF MEMS Multi-throw Switches”, 8th IEEE International Conference on Nano/Micro Engineering and Molecular Systems (NEMS), April 7-10, 2013.

[55] Karl, John H. (2012), An Introduction to Digital Signal Processing, Elsevier, p. 110, ISBN 9780323139595.

[56] K. R. Betty and Gary Horlick, “Transversal analog filter uses integrators transistors”, Analytical Chemistry, vol. 48, no. 14, Dec. 1976.

[57] John D. Kraus and Ronald J. Marhefka, “Antennas”, 3rd Edition, McGraw-Hill Science.

[58] A. W. F. Edwards, “Pascal’s arithmetical triangle: the story of a mathematical idea”, JHU Press, 2002. Pages 30–31.

[59] R. J. Mailloux, “Phased Array Antenna Handbook”, Section 3.1.4, Second Edition.

[60] C. A. Allen, “Metamaterial based composite right/left handed transmission line” metamaterial-based transmission line components and antennas, University of California, Los Angeles, ProQuest, 2007.

[61] G. V. Eleftheriades, K. G. Balmain, “Negative-Refraction Metamaterials: Fundamental Principles and Applications”, IEEE Press Wiley Inter-science, 2005.

[62] J. Sanchez-Martnez, E. Marquez-Segura, P. Otero and C. Camacho, “Artificial transmission line with left/right-handed behavior based on wire bonded interdigital capacitors”, Progress In Electromagnetic Research B, Vol. 11, 245–264, 2009

[63] Douglas R. Jachowski and Clifford M. Krowne, ”Frequency Dependence of Left-Handed and Right-Handed Periodic Transmission Structures”, 2004 IEEE MTT-S Digest.

[64] J. Lampen, S. Majumder, C. ji and J. Maciel, “Low-loss, MEMS based, broadband phase shifters", IEEE International Symposium on Phased Array Systems and Technology, October 12-15, 2010.

[65] R. Goggin and P. Macdaid, “Commercialization of a reliable RF MEMS switch with integrated driver circuitry in a miniature QFN package for RF instrumentation applications,” IEEE Int. Microwave Symp., May 2015.

[66] D. Chen, Q. Wang and Z. Shen, “A broadband microstrip to CPW transition”, Asia Pacific Microwave Conference, Dec. 4-7, 2005.

[67] S. Alexandrou, R. Sobolewski and T. Hsiang, “Bend Induced Even and Odd Modes in picosecond Electrical Transient Propagated on a Coplanar Waveguide”, Applied Physics Letters, Vol. 60, No.15, April 1992.

[68] R. N. Simons, “coplanar waveguide circuits, components and systems”, NJ, USA, Copyright 2001 John Wiley & Sons.

[69] K. Hettak, T. Laneve, and M. G. Stubbs, “Size Reduction Techniques for CPW and ACPS Structures”, IEEE Transactions on Microwave Theory and Techniques, vol. 49, No. 11, November, 2001.

[70] D. M. Pozar, “Microwave Engineering”, 3rd Edition, NJ, USA, Copyright 2005 John Wiley & Sons.

[71] Agilent application note, “Improved Methods for Measuring Distortion in Broadband Devices Agilent Technologies”, Agilent technologies Inc. 2008 Printed in USA, December 10, 2008 5989-9880EN.

[72] C. Cheng and G. Rebeiz, “A very low loss 1.9–2.1 GHz RF MEMS phase shifter,” IEEE MTT-S Int. Microwave Symp., Jun. 2012.

[73] C. Cheng and G. Rebeiz, “An electronically-scanned 1.8–2.1 GHz basestation antenna using packaged high-reliability RF MEMS phase shifters,” IEEE MTT Transactions, Feb. 2013.

[74] M. Roy, “Distortion Cancellation Performance of Miniature Delay Filters for Feedforward Linear Power Amplifiers”, IEEE Ultrasonics Symposium, October 7-10, 2001.

[75] M. Kim, J. B. Hacker, R. E. Mikailovich and J. F. DeNatale, “MEMS True-Time Delay Circuit for Broadband Antennas”, Antenna and Propagation Society, 2001.

[76] Y. Liang, C. W. Domier and N. C. Luhmann, “MEMS Based True Time Delay Technology for Phased Antenna Array Systems”, Asia Pacific Microwave Conference 2007.

[77] J. Lampen, S. Majumder, C. ji and J. Maciel, “Low Loss, MEMS Based, Broadband Phase Shifters", IEEE International Symposium on Phased Array Systems and Technology, October 12-15, 2010.

[78] Y. Du, J. Bao Z. He and J.Jiang, “A X band Switched Line 5 bit Phase Shifter with RF MEMS Multi throw Switches”, NEMS 2013, April 7-10, 2013.

[79] J. B. Hacker, R. E. Mihailovich, M. Kim and J. F. DeNatale, “A Ka-Band 3 bit RF MEMS True-Time Delay Network”, IEEE Transactions on Microwave Theory and Techniques, vol. 51, no. 1, January 2003.

[80] D. Chen, Q. Wang and Z. Shen, ”A Broadband Microstrip to CPW Transition”, Asia Pacific Microwave Conference, December 4-7, 2005.

[81] S. Alexandrou, R. Sobolewski and T. Hsiang, “Bend Induced Even and Odd Modes in picosecond Electrical Transient Propagated on a Coplanar Waveguide”, Applied Physics Letters, Vol. 60, No.15, April 1992.

[82] R. N. Simons, “Coplanar Waveguide Circuits, Components and Systems”, NJ, USA, Copyright 2001 John Wiley & Sons.

[83] S. Ibrahim, G. Szczepkowski and R. Farrell, “Wide Band Switched Delay Line using MEMS Switches", Royal Irish Academy Conference, April 2014.